Numerical Investigation of the Structure Effects on Water Transportation in PEMFC Gas Diffusion Layers using X-ray Tomography based Lattice Boltzmann Method

Fontip Jinuntuya

A Doctoral Thesis

Submitted in partial fulfillment of the requirements for the award of
Degree of Doctor of Philosophy of Loughborough University

January 2015

Abstract

The excessive presence of liquid water in a gas diffusion layer (GDL) hinders the access of reactant gases to the active sites of the catalyst layer leading to decreased performance of a polymer electrolyte membrane fuel cell (PEMFC). Therefore, GDLs are usually treated with a hydrophobic agent to render their fibres more hydrophobic in order to facilitate gas transport and water removal. Numerous studies have been conducted to investigate water transport in PEMFCs in recent years; however, the behaviour of liquid water in a GDL at a pore-level is poorly understood. Macroscopic models fail to incorporate the influence of the structural morphology of GDLs on liquid water transport behaviour. Experimental methods are not conducive towards a good understanding at a microscopic level because of the diminutive size of the GDLs' porous structure. Alternatively, the Lattice Boltzmann (LB) method has gathered interest as it is found to be particularly useful in fluid flow simulations in porous media due to its capability to incorporate the complex boundaries of actual GDL structures. To date, most studies on fluid transport in GDLs integrated artificial structures generated by stochastic simulation techniques to the LB models. The stochastic-based model, however, does not represent closely the microscopic features of the actual GDL as manufactured. In addition, comparison of liquid water transport behaviour in different GDL structures using the LB method is rare since only a single GDL material has been utilised in most of those studies.

This thesis aims to develop our understanding of liquid water transport behaviour in GDLs with morphologically different structures under varying wettability conditions based on the LB method and the X-ray computed tomography (XCT) technique. GDLs with paper and felt structures were reconstructed into 3D digital volumetric models via the XCT process. The digital models were then incorporated into a LB solver to model water saturation distribution through the GDL domains. The GDL wettability was also altered so that the effect on liquid water behaviour in the GDL could be examined.

This project is divided into three main sections. In the sensitivity analysis, the effect of image resolution on gas permeability through the X-ray reconstructed GDL was

carried out using a single-phase LB model. It was found that the resolution variation could significantly affect the resulting gas permeability in both principal and off-principal directions, as well as computational time. An optimum resolution, however, exists at 2.72 μm/pixel, which consumed 400 times less computational time with less than 8% difference in the resulting permeability compared to the base resolution. This study also served as a guideline for selecting a resolution for generating the XCT images of the GDLs which were utilised in the following studies.

In the structure analysis, the structures of the paper and felt GDLs were generated using the XCT and the key properties of each GDL, including thickness, porosity, permeability and tortuosity, were characterised. The thickness and the through-plane porosity distributions of each GDL were examined based on the tomography images. The resulting local through-plane porosity distributions were then used to calculate through-plane permeability and tortuosity distributions using an analytical model available in the literature. This study revealed the heterogeneity of the GDLs and how the heterogeneous nature of the GDL structures affects others properties of the GDLs. In this study, the absolute through-plane permeability and tortuosity of the X-ray-reconstructed GDL samples were also characterised using the single-phase LB model. The results from the two models were then compared and validated against data in the literature.

In the water transport analysis, the two-phase LB model was employed to examine the effects of GDL structures on the behaviour of liquid water in the GDLs, including invasion patterns, saturation distribution and breakthrough behaviour under varying GDL wettability conditions. It was found that wettability was responsible for invasion patterns and water saturation levels whilst the GDL structure was mostly responsible for breakthrough occurrence and saturation distribution. It was observed that water travelled with stable displacement saturating all pores in hydrophilic GDLs, while it travelled with capillary fingering causing decreased saturation in hydrophobic GDLs, about 50% in the highly hydrophobic cases. The GDL structure was found to play a key role in breakthrough behaviour in the hydrophilic GDL as it was seen that the through-plane fibres in the felt structure and the through-plane binders in the paper structure encouraged water removal from the GDL in the thickness direction. Conversely, the GDL structure was found to have negligible influence on breakthrough in the hydrophobic

GDL. Each GDL structure, however, contributed to a distinct difference in water distribution in the GDL with hydrophobic wettability.

The work presented in this thesis contributes to the understanding of liquid water transport behaviour in the GDLs under the combined effects of the GDL structures and wettability conditions, which is essential for the development of effective PEMFC water management and the design of future GDL materials.

Acknowledgements

I would like to express my deepest and sincere gratitude to my supervisor, Prof. Rui Chen for offering the opportunity to be part of his group. I am very grateful for his excellent supervision, constant encouragement and support throughout the course of this study.

I appreciate our collaborator, Dr. Xiaoxian Zhang, University of Liverpool for providing the LB codes and support on LB simulation.

I would like to thank members of fuel cell and combustion group for their help and support. I further want to thank the staff and members of Department of Aeronautical Engineering for their help, support and providing a pleasant environment over the time of this study.

I further extend my gratitude to my sponsors the Royal Thai Government for supporting throughout the course of this study.

Finally, I would like to thank my family. I am so grateful to my dear parents and brother for always loving, cheering and supporting me.

Table of Contents

List of Figures

Chapter 1

Chapter 2

Chapter 3

Chapter 4

Chapter 5

Chapter 6

Chapter 7

List of Tables

Chapter 6

Chapter 7

Nomenclature

$f_i(x,t)$	particle distribution function
x	location
t	time
i	direction
$f_i^{eq}(x,t)$	equilibrium distribution function
c_s	speed of sound
u	velocity
k	absolute permeability
q	average gas velocity
P	pressure
L	size of the domain
q_x	average velocity in x direction
q_y	average velocity in y direction
q_z	average velocity in z direction
L_x	size of the domain in x direction
L_y	size of the domain in y direction
L_z	size of the domain in z direction
r_f	fibre radius
u_x	velocity component in x direction
u_y	velocity component in y direction
u_z	velocity component in z direction
u_{ave}	average velocity
M	transformation matrix
S	collision operator matrix
$\hat{S}$	diagonal collision matrix
F_k	total force

F_{f-f}^{k}	fluid-fluid interaction
F_{f-s}^{k}	fluid-solid interaction
u'	bulk fluid velocity
u_k	velocity of fluid k
$G_{k\bar{k}}(x,x')$	Green's function
$g_{k\bar{k}}$	interaction strength between fluid component k and $\bar{k}$
$G_{ks}(x,x')$	fluid-solid interaction parameter
g_{ks}	interaction strength between fluid k and the solid wall
Bo	Bond number
Ca	capillary number
Re	Reynolds number
We	Weber number
D	average pore diameter
g	gravitational acceleration
U_w	velocity of liquid water
P_N	pressure outside the bubble
P_W	pressure inside the bubble
R	radius of bubble
w_i	weighting factor

Greek

ξ_i	velocity in direction i
τ	dimensionless relaxation parameter
ρ	fluid density
μ	dynamic viscosity
ν	kinematic viscosity
ε	porosity
ε_p	percolation threshold porosity

α	fitted value
θ	contact angle
μ_a	viscosity of air
μ_w	viscosity of liquid water
ρ_a	density of air
ρ_w	density of liquid water
σ	interfacial tension
Ω_i	collision operator

Abbreviations

PEMFC	polymer electrolyte membrane fuel cell
GDL	gas diffusion layer
GDE	gas diffusion electrode
CL	catalyst layer
GC	gas channel
MEA	membrane electrode assembly
PTFE	polytetrafluoroethylene
MPL	microporous layer
LB	Lattice Boltzmann
PN	pore network
XCT	X-ray computed tomography
SEM	scanning electron microscopy
NMR	nuclear magnetic resonance
SRT	single relaxation time
MRT	multiple relaxation time
SC	Shan-Chen model
TS	Tomadakis and Sotirchos model

Chapter 1
Introduction

1.1 PEMFC and its Working Principles

A fuel cell is an electrochemical energy conversion device that directly converts chemical energy stored in gaseous reactants, hydrogen and oxygen, into electrical energy. Fuel cells have been considered as an alternative power source to the conventional fossil fuel based system due to their high energy efficiency, zero emissions and low noise. Among the various kinds of fuel cells, polymer electrolyte membrane fuel cells (PEMFC) are the most attractive types of fuel cells owing to their capability to power a broad range of applications, their simplicity in assembling, and ability to work in any orientation [1]. A single PEMFC typically consists of seven components including a polymer electrolyte membrane (PEM), anode and cathode catalyst layers (CL), gas diffusion layers (GDL), and bipolar plates (BPP) with flow field channels, as illustrated in Fig. 1.1.

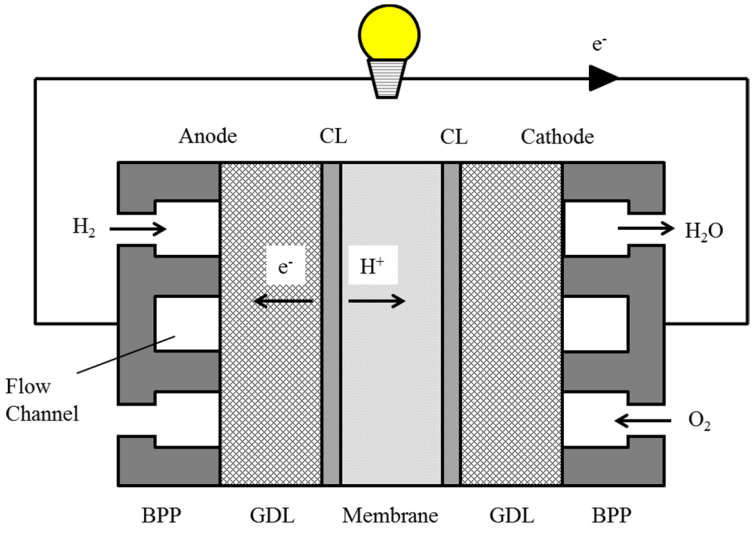

Figure 1.1 Schematic of a PEMFC.

The membrane, catalyst and gas diffusion layers are often mechanically compressed together at high temperatures and pressures to form a single piece, commonly called membrane electrode assembly (MEA) [2, 3], while the bipolar plates with flow field channels, usually called gas channels (GC), are positioned on either side of the MEA for delivering gaseous reactants towards the electrochemical reaction sites.

The gaseous reactants, hydrogen and oxygen, are supplied continuously to the anode and cathode gas channels of the bipolar plates respectively. These gases then diffuse through the porous GDL towards their corresponding CL where electrochemical reactions occur. At the anode CL, where the hydrogen oxidation reaction (HOR) takes place, hydrogen splits into protons and electrons. The protons travel through the electrolyte membrane and reach the cathode CL, while the electrons produced in the anode CL are not allowed to travel through the membrane due to its low electronic conductivity. As a result, the electrons are forced to transfer to an external circuit, thus generating electricity. At the cathode, the protons and electrons react with the oxygen supplied from the cathode gas channels, forming water by the oxygen reduction reaction (ORR) [2, 4]. The chemical reaction can be described as follows:

$$\text{Anode: } H_2 \rightarrow 2H^+ + 2e^- \tag{1.1}$$

$$\text{Cathode: } \frac{1}{2}O_2 + 2e^- + 2H^+ \rightarrow H_2O \tag{1.2}$$

1.2 Water Transport and Flooding Phenomena in PEMFC

In a PEMFC, water is produced internally at the cathode CL as a result of the oxygen reduction reaction (ORR), and is also supplied to the PEMFC by humidified reactant gases in order to hydrate the membrane [5]. There are also two means of water transport through the membrane: electro-osmotic drag and back diffusion. The electro-osmotic drag drives water to move from anode to cathode along with the protons, whilst during back diffusion water is forced to move towards the anode due to the concentration gradient of water across the membrane. The water flux caused by the electro-osmotic drag is proportional to the protonic flux and the back diffusion flux is related to the concentration gradient of water [5, 6]. Water is essential to maintain membrane hydration in order to

ensure high ionic conductivity and avoid potential membrane degradation [5, 7-9]. An adequate amount of water at the cathode, however, has to be transported away from the CL by either vapour diffusion or capillary liquid water transport [5]. If this water removal is not sufficient enough, excessive water may condense at preferential locations and fill the pores of the electrodes, thereby reducing the ability of reactant gas to reach the CL. In addition, the liquid water may further cover the catalyst sites in the CL and render them electrochemically inactive [10, 11]. This phenomenon is known as 'flooding' and is an important limiting factor of PEMFC performance [5]. Although flooding is generally associated with the higher current densities due to the higher water production, it is also usually observed even at low current densities, particularly under low gas flow rates and lower operating temperatures [12]. In addition to the performance reduction due to the reactant transport limitation, excess liquid water can also cause non-homogeneous current density [5], ineffective heat removal [13] and serious damage of constituent components at sub-zero environments [14]. As already mentioned, it is obvious that the delicate balance of water in the PEMFC is vital and the presence of excess liquid water in the PEMFC components has a critical impact on PEMFC performance and durability; hence, the understanding of liquid water in PEMFC components, particularly in the GDL, is of paramount importance in achieving high performance, durability and successful operation of the PEMFC.

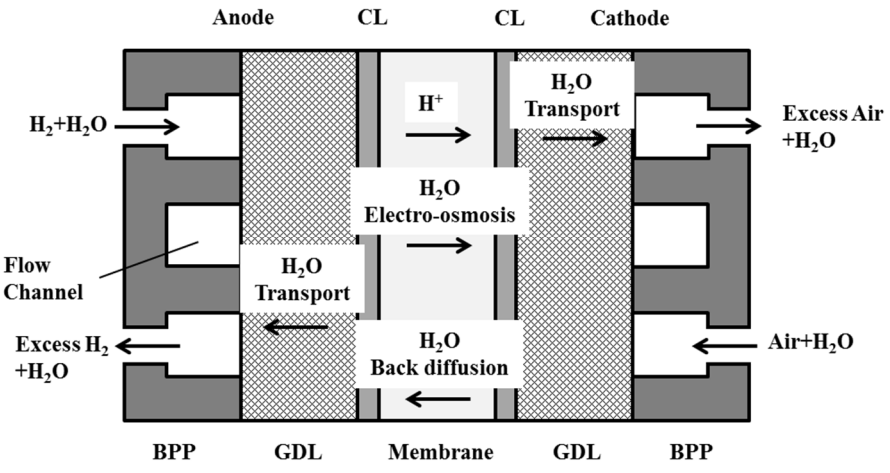

Figure 1.2 Schematic of water transport in a PEMFC. Adapted after [5].

1.3 Gas Diffusion Layers

Gas diffusion layers (GDL) play a crucial role for a PEMFC by serving several functions. A GDL provides pathways for reactant gases to be transported from a gas supply channel to a CL and for product water to be removed from the CL to the gas channel. It also provides pathways for electrons to transport from the CL to the bipolar plate, as well as pathways for heat removal from MEA to bipolar plates. In addition, it provides physical support for the MEA [15]. The GDL is therefore designed to meet the following functions: [15, 16]

- It has to be porous both in the in-plane and through-plane directions in order for reactant gases to be able to flow through and effectively distribute to the active sites of the CLs, as well as for product water to travel from the CL to the gas channels at a rate that retains membrane hydration, while not allowing water accumulation [17].
- It has to be electronically conductive to allow the electrons to complete the electric circuit.
- It has to be thermally conductive to facilitate the heat generated in the electrochemical reactions in the CL to be conducted to the bipolar plates where the coolant channels are located.
- It has to be sufficiently rigid to support the MEA.
- It has to provide a good balance between water expulsion and water retention to ensure the PEMFC works without flooding or membrane dehydration.

The materials typically used as a GDL are carbon paper, carbon felt and carbon cloth with a thickness in the range of 100-300 μm [3]. The micrographs of each type of GDL are shown in Fig. 1.3. Carbon paper and carbon felt consist of randomly dispersed carbon fibres, whilst carbon cloth consists of woven bundles of carbon fibres. The individual carbon fibres are around 7-12 μm in diameter and the bundle diameter can be in the region of 400 μm [15, 18]. The largest pore diameters in the carbon paper and carbon cloth are about 40 μm and 250 μm respectively [19]. The porosity is usually between 70% and 80% [16].

In terms of PEMFC performance, carbon cloth GDL is reported to perform better than carbon paper GDL at high humidity conditions, as it has lower tortuosity and a rougher surface facilitating droplet detachment [20]. Carbon paper GDL, however, exhibits better performance under dry conditions as it has higher tortuosity which prevents the loss of product water to dry gas streams, thus keeping the membrane hydrated and reducing ohmic loss [20].

The GDL is usually treated with a hydrophobic agent, such as poly-tetrafluoroethylene (PTFE) with loading varying from 5% to 30% wt., to alter its wetting characteristics in order to facilitate liquid water removal and thus gas transport [5, 15, 20, 21]. The PTFE treatment creates hydrophobic and hydrophilic pockets of pores in the GDL [5, 15, 22, 23] which allow separate paths for gas transport and liquid water transport [5]. A micro-porous layer (MPL), which consists of carbon powder and PTFE particles, is usually coated on the GDL near the CL to improve PEMFC performance [24].

The degree of hydrophobicity is dependent upon the amount of PTFE content added to the GDL [25]. It was reported that enhancing the hydrophobicity of the GDL improved both gas and liquid water transport in the PEMFC under high humidity operating conditions, but excessive PTFE content added could reduce the hydrophilic pathways, thus diminishing the liquid water removal from the CL and the GDL making the electrode more prone to flooding [26]. Accordingly, an optimised PTFE content in the GDL has been suggested in order to improve the gas-liquid transport in the GDL and thus the overall performance of PEMFC [26].

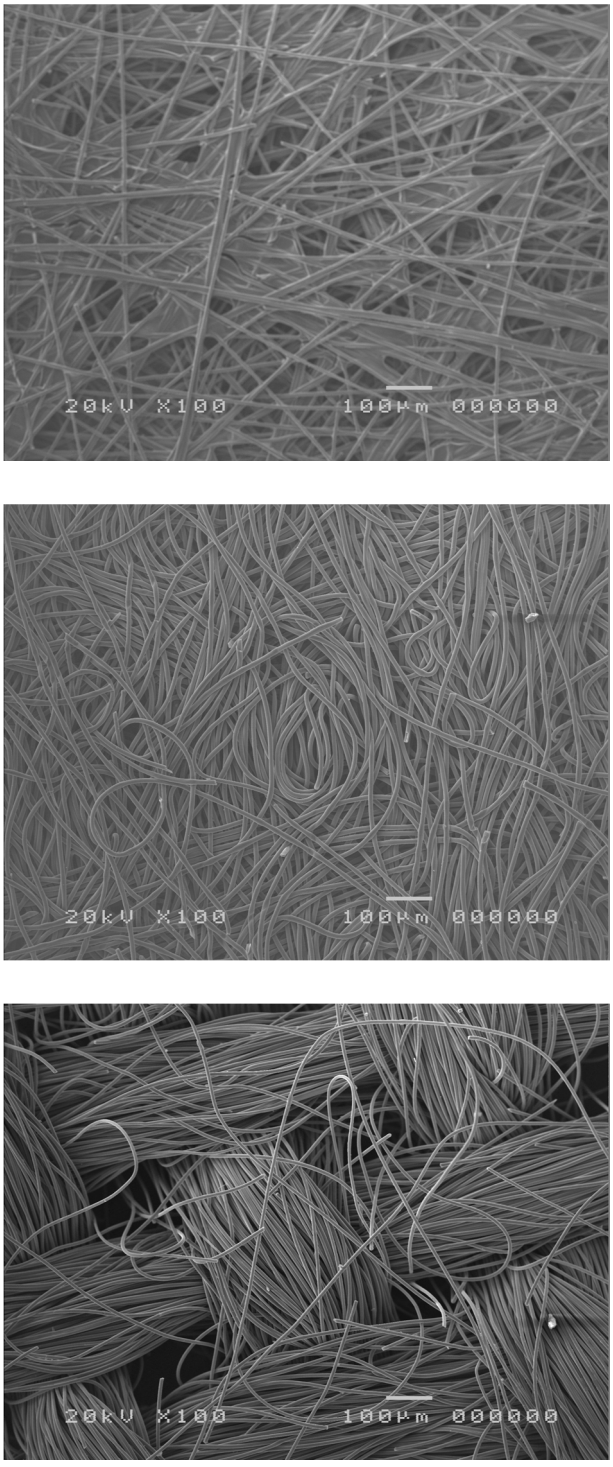

Figure 1.3 Micrographs of (a) carbon paper, (b) carbon felt and (c) carbon cloth GDL samples.

1.4 Properties of Gas Diffusion Layers

In this section, the most important properties of a GDL that strongly influence water management and performance of a PEMFC including wettability, capillary breakthrough pressure, porosity, pore size distribution, permeability and liquid transport properties are reviewed.

1.4.1 Wettability and Capillary Breakthrough Pressure

The GDL is usually treated with a hydrophobic agent in order to enhance liquid water and gas transport in the GDL, which in turn results in high PEMFC performance. Different kinds of hydrophobic agents such as PTFE (polytetrafluoroethylene), FEP (fluorinated ethylene propylene) and PVDF (polyvinylidene fluoride) have been utilised in order to improve the hydrophobicity of the GDL [9, 27]. The hydrophobic agents can be coated onto the GDL in many ways including dipping, brushing and spraying [27]. The most common way is dipping the GDL into a solution containing a pre-determined amount of hydrophobic polymers [21, 27]. The loadings of PTFE and FEP in the GDL are usually between 5% and 30% by weight [21].

A number of works have studied the effect of hydrophobic treatment on cell performance and on liquid water transport in the GDL. Some indicate that increasing hydrophobic content in the GDL can reduce the saturation level in the GDL [25, 28-31]. Bevers et al. [28] studied the effect of PTFE contents on water saturation in carbon paper GDL by comparing the sample weights before and immediately after their immersion in demineralised water for ten minutes. The results indicate a decrease in water saturation levels with an increase in PTFE content. A numerical study by Prat and co-workers [25] using a pore network (PN) model also indicates a decrease in water saturation levels in a hydrophobic GDL. Using a two-phase LB model, Hao and Cheng [29] and Rama and co-workers [30, 31] demonstrated a saturation reduction with an increasing hydrophobicity. Too much hydrophobic loading, however, can lead to poor gas and water transport due to the blockage of pores by excessive hydrophobic agents [32-34]. Park et al. [32] examined liquid water behaviour in the GDLs with 0% to 45% PTFE under several PEMFC working conditions. They found that the higher PTFE hindered the removal of water from the CL to the gas channel and would cause water flooding in the CL. Lim and Wang [33]

studied the effects of the hydrophobic FEP content on PEMFC performance by treating a commercial GDL with 10% and 30% FEP. The results indicate that the 10% FEP loading provides sufficient hydrophobicity for effective water removal resulting in higher power performance. They concluded that the significant difference in performance was mainly due to the fact that excessive FEP loading results in the significant blockage of pores, which may limit reactant transport and liquid water removal and thus fuel cell performance. Prasanna et al. [34] investigated a number of carbon paper GDLs with different PTFE loadings and observed a significant decrease in cell performance for the cathode GDL with 30% or higher PTFE loading. Their results also suggest that the GDL with 20% PTFE provided the optimum condition for liquid water and gas transport. Lin and Nguyen [26] suggested that liquid water transport and gas transport can be improved when a PEMFC operates under high levels of humidity by adding PTFE to the GDL to render the GDL more hydrophobic. They found, however, that adding too much PTFE decreases the hydrophilic pores and thus prohibits liquid water to transport away from the CL. Velayutham et al. [35] studied the effects of PTFE content in the GDL ranging from 7% to 30% and found that the optimum PTFE content for controlling water flooding was 23% at their PEMFC test conditions (55°C and ambient pressure). Using a transparent fuel cell, Tuber et al. [36] studied the impact of GDL wettability on water transport and cell performance by comparing untreated and 20% PTFE-treated GDLs. The results indicated that the treated GDL could lead to flooding while operating at room temperature.

GDLs with highly hydrophobic contents also require higher intrusion pressure to drive the flow of liquid water to penetrate the GDL. Tuber et al. [36] suggested that a sufficiently large build-up pressure is required to initiate flow from the CL and GDL interface to the GDL and GC interface to form droplets on the GDL surface. The capillary breakthrough pressure is usually in the range of 5kPa – 15kPa [18, 24, 37-39]. Benzinger et al. [18] studied liquid water flow through carbon paper and carbon cloth GDLs with different PTFE contents using a pressurised membrane filtration cell in which the pressures were controlled by the water level above the tested sample found that minimum pressures of 5kPa to 10kPa were required for liquid water to pass through the GDLs with 0% to 60% PTFE loadings. Tamayol and Bahrami [40] conducted a similar study on water permeation through the GDLs using a custom-built pressurised membrane filtration

cell. They compared similar carbon paper GDLs with different thickness and PTFE loadings. Their results suggested that the breakthrough pressure increases with PTFE loading and thickness. The breakthrough pressure rises from 3.5kPa to 5.3kPa with an increase in PTFE loadings from 0% to 20%.

Fresh GDLs are usually treated with PTFE to enhance their hydrophobicity in order to improve water and gas transport; however, they lose hydrophobicity over time [7]. The PTFE content of the GDL has been reported to decrease gradually with fuel cell operation especially at the cathode [9, 24, 41]. The loss of PTFE is a main degradation mechanism in a GDL and has been found to change the wettability of the GDL [24]. Several works have been conducted experimentally and numerically to understand the effect of the wettability change. A decrease in the GDL contact angle of a FEP-coated carbon paper GDL with immersion time in water was reported [41]. Mukherjee et al. [42] conducted a study using a LB model to examine the effect of a mixed wettability GDL representing an aged GDL. They found that the mixed wettability GDL becomes prone to enhanced flooding compared to the fresh GDL represented by a fully hydrophobic GDL. A pore network (PN) approach was also carried out to investigate the effect of mixed wettability on water transport behaviours in the GDL by applying a different hydrophilic fraction into the models. Sinha and Wang [43] found that water preferentially flows through hydrophilic pores and suggested that the optimum hydrophilic pore fraction could provide the least gas transport resistance. Kuttanikkad et al. [44] and Wu et al. [45] also studied the impact of different hydrophilic pore fractions on water saturation and found that the hydrophilic pore fraction become significant only when the fraction was beyond the threshold fraction.

1.4.2 Pore Structure: Porosity and Pore Size Distribution

Porosity and pore size distribution (PSD) of the GDL are among the most important parameters influencing gas and liquid transport in the GDL. Porosity determines permeability and affects the liquid water saturation profile across the GDL [5, 24]. It allows gas permeation through the GDL to access the CL and product water to transport out from the CL to the gas channel. High porosity enhances mass transport across the GDL contributing to high limiting currents. High porosity, however, reduces the electronic conductivity and mechanical strength of the GDL [24]. Increasing the

hydrophobic agent (PTFE) loading to the GDL reduces GDL porosity and changes pore size distribution of the GDL in which the mean pore diameter is lower than the original [17].

Porosity and PSD can be determined by several methods, such as intrusion and capillary flow porosimetry [46]. The intrusion method evaluates the total pore volume by measuring the amount of an intruding fluid that has penetrated into the pores of a porous medium as a function of applied pressure [47]. The capillary flow method employs similar principles as the intrusion method. Instead however, of using a non-wetting fluid and driving it into the pores as the intrusion method does, the capillary flow method initially saturates the pores with a wetting fluid and uses a gas to drive the wetting fluid out [46].

The effects of GDL porosity have been investigated mainly through modelling. Most models use a constant porosity value for simplicity whilst only a few consider the GDL with non-uniform porosity [5]. Nam and Kaviany [48] reported that higher porosity decreases water saturation in the GDL while increasing limiting currents. Kong et al. [49] studied the impact of pore size distribution and porosity of GDLs on cell performance and indicated that pore size distribution is a more important structural parameter influencing cell performance than porosity. They concluded that mass transport loss can be lessened by enlarging the macro-pores volume in the GDL, which in turn results in improved cell performance. Williams et al. [50] characterised pore size distribution and permeability for several GDL samples and suggested that larger pores and high gas permeability could improve oxygen transport through the GDL. Using a one-dimensional model, Zhan et al. [51] analysed water saturation distribution for the GDL with different porosity patterns including uniform porosity, sudden change in porosity and gradient change in porosity, based on the assumption of a fixed water flux through the GDL. Their results suggest that the GDL with a gradient porosity is more favourable to liquid water ejection from the CL to the GC. Chen et al. [52] used a multi-phase model to analyse liquid water saturation profiles and oxygen concentration across the GDL. Their results confirm the benefit of a gradient in porosity in enhancing water removal and oxygen transport through the cathode GDL. Zhan et al. [53] studied liquid water distribution in relation to GDL porosity distribution patterns using a one-dimensional model. For the GDL with uniform

porosity, it was found that the gas diffusion increased with an increase in porosity and contact angle and a decrease of GDL thickness. For the GDL with a gradient porosity, it was found that a larger porosity gradient contributed to better gas diffusion. Han et al.[54] compared a carbon-filled GDL with conventional carbon paper-based single-layer and dual-layer GDLs. They concluded that the carbon-filled GDL contributed to better performance than the conventional GDLs, although it has a lower porosity of about 67% and a smaller average pore diameter of 4.7 μm. Hiramitsu et al. [55] suggested that flooding originates at the interface between CL and GDL and can be eliminated by controlling the pore size of the GDL at the interface. Using X-ray tomography images, Fishman et al. [56] characterised porosity distribution for several commercially available GDLs and reported that the porosity in the thickness direction is non-uniform. The distinct difference in porosity distributions for different types of GDLs was also presented. From the same group, Hinebaugh et al. [57] utilised a PN model based on the porosity distributions obtained in [56] to simulate the saturation distributions of liquid water in the GDLs. The results show a corresponding trend between the saturation distribution at breakthrough and the porosity distribution for each sample.

GDL compression is another factor affecting GDL morphology and porosity [24]. Chang et al. [58] investigated the effect of clamping pressure on the porosity of the GDL over the pressure range of 0 bar to 35 bar. Their results indicated that the porosity of the GDL is inversely proportional to the external clamping pressure with a relatively sharp decrease in porosity for pressures below 5 bar. Bazylak et al. [59] reported that the compression alters the GDL microstructure and water transport behaviours due to the breakup of fibres and loss of hydrophobicity of the GDL due to fibre damage. Using a combination of LB method and X-ray tomography, Rama et al. [60] examined the effect of compression on the structural properties of a carbon cloth GDL. The GDL samples were compressed in the range of 0MPa – 100MPa and encapsulated using polydimethylsiloxane (PDMS) then reconstructed to digital 3D models by using X-ray computed tomography. The structural models indicate that structural change, as a result of increasing compression pressure, proceeds through a three-step process including general compaction of individual fibres, elongation of individual tow cross-sections and deformation of individual tow cross-sections. The results indicate a substantial decrease in the mean pore diameter from 33 μm to 12 μm over the range of the compression.

1.4.3 Permeability

Permeability of the GDL is one of the main properties influencing gas and water transport in PEMFCs [50]. It is a measure of resistance due to convective flow, which can be estimated by applying a pressure drop and measuring flow across the sample [15]. The permeability coefficient representing permeability of a sample is usually calculated using Darcy's law [15, 47].

Most GDLs are made either by pressing chopped carbon fibres together to form a carbon paper or by weaving bundles of carbon fibres to form a carbon cloth. As a result, the GDL structure is very different in all directions [61]. With its highly anisotropic nature, the GDL also exhibits highly anisotropic permeability characteristics [24]. Gostick et al. [62] measured gas permeability in all three perpendicular directions for several commercial GDL samples and found that most samples exhibited higher in-plane permeability than through-plane permeability.

Several experimental and numerical studies have been conducted to study the through-plane and in-plane permeability characteristics under various conditions. Most experimental permeability measurements used an apparatus developed in-house. Mathias et al. [15] measured through-plane and in-plane permeability of an uncompressed commercial carbon paper GDL without MPL. Prassanna et al. [34] studied through-plane permeability of GDL samples with varying PTFE loadings from 10% to 40% PTFE and without MPL. The results show that permeability decreases with increasing PTFE loadings. Ismail et al. [63] measured the through-plane permeability for treated and untreated GDL samples. The results indicated that there exists an optimum amount of PTFE at which the through-plane permeability of the GDL is at a maximum (5% in this study). Williams et al. [50] measured nitrogen flow through several GDL samples (both single-layer and dual-layer) in the through-plane direction. The results indicated that the addition of MPL to the substrate substantially decreases through-plane permeability. They concluded that large pores and high gas permeability improve convection and thus oxygen transport through the GDL. Feser et al. [64] measured air permeability of woven carbon fibre, non-woven carbon fibre and carbon paper GDL samples using a radial flow test apparatus developed in-house. They found that the woven and the non-woven samples have significantly higher in-plane permeability than the paper GDL. Ahmed et

al. [65] investigated cell performance under various isotropic and anisotropic permeability conditions using a three-dimensional, non-isothermal model. They reported that cell performance was significantly affected by both isotropic and anisotropic permeability, particularly when permeability in one or both directions was low. They attributed the low cell performance to the reduced water removal from the GDL due to low permeability. Tamayol and Bahrami [66] developed an analytical model for predicting the in-plane permeability of the GDL as a function of porosity and fibre diameter. The model of porous medium was constructed as a mixture of fibres parallel and normal to flow directions and the permeability of the porous medium was modelled as a blend of the permeability of its components. Their results illustrated that the in-plane permeability of a GDL is proportional to its porosity and the fibre diameter squared. The LB method was also utilised by different research groups [19, 60, 67-69] to examine gas permeability in both carbon paper [19, 67, 68] and cloth GDLs [60, 69]. In a study using the LB model, Rama et al. [19] also validated the simulated air permeability result with the experimentally measured result and reported a difference of only 3%, suggesting that the LB model is a powerful method for estimating permeability.

Several studies have also been conducted to examine the effects of compression on gas permeability of the GDL. Ihonen et al. [70] measured in-plane permeability for several GDL samples at different levels of compression and found that the permeability decreased with increasing compression applied on the GDL. Similarly, Chang et al. [58] measured in-plane permeability as a function of the clamping pressure and found that permeability exponentially decreases as pressure increases. Instead of measuring permeability as a function of compression, Nitta et al. [71] measured in-plane permeability as a function of compressed thickness. They found that in-plane permeability decreased non-linearly as the compressed thickness of the GDL was decreased. The results also showed that permeability is reduced by one order of magnitude when the GDL was compressed to about 65% of its initial thickness. They attributed the non-linear permeability reduction to changes in pore size and its distribution due to compression. Using a three-dimensional, non-isothermal model, Ahmed et al. [72] observed the effect of clamping pressure applied through the bipolar plate on isotropic and anisotropic permeability and found that it caused a decrease in both isotropic and anisotropic permeability by several orders of magnitude. In another

numerical approach, Rama et al. [60] used the LB model to examine the effect of compression on anisotropic permeability of an X-ray reconstructed carbon cloth GDL under compression ranging from 0MPa to 100MPa. The simulated results illustrated that the degree of anisotropy of the carbon cloth GDL increases ab initio and peaks in the range of 0.3MPa – 10MPa, indicating that the optimum in-plane permeability relative to through-plane permeability exists within this range of compression pressures. Beyond this range, in-plane, through-plane permeability and the degree of anisotropic permeability all show a decrease.

Air and water relative permeability in the GDL have also been studied. He et al. [73] developed a fraction model based on the micrograph image of a commercial carbon paper GDL to predict permeability and liquid water relative permeability of the GDL. The results suggested that permeability increases with the decrease of tortuosity. The results also indicated that the water relative permeability in the hydrophobic case is much higher than in the hydrophilic case suggesting that a hydrophobic carbon paper GDL is favourable to the removal of liquid water. Hussaini and Wang [74] measured absolute permeability and air-water relative permeability for both carbon paper and carbon cloth GDLs. They found that carbon paper GDLs display higher permeability in the in-plane direction than in the through-plane direction by about 18%, whilst the carbon cloth GDL exhibits higher permeability in the through-plane direction by about 75% than its in-plane value.

1.4.4 Liquid Transport Properties

Characterisation of liquid water transport in the GDL can be performed in various ways, either by experimental investigation through both in-situ and ex-situ visualisation or by numerical modelling [21]. Visualisation techniques include nuclear magnetic resonance (NMR) imaging, neutron imaging, X-ray imaging, scanning electron microscopy and direct optical photography. Numerical modelling includes macroscopic and pore-scale models, such as the pore network (PN) and Lattice Boltzmann (LB) models. Several works have been conducted to understand the liquid water transport behaviours in the GDL. Some of those works are summarised below.

Nam and Kaviany [48] visualised water droplets on the GDL surface using an environmental scanning electron microscope (ESEM) and observed the agglomeration of small water droplets to form larger droplets in the GDL. Based on the agglomeration of small droplets observed, they proposed a branching-type geometry to describe water distribution in the GDL in which water vapour condenses on the GDL fibres as micro-droplets, which then accumulate to form macro-droplets and consequently a flow of liquid water that extends from the CL to the gas channel.

Pasaogullari and Wang [10] developed a one-dimensional analytical model for liquid water transport in both hydrophobic and hydrophilic GDLs. They suggested that the transport of liquid water in the GDL is governed by capillary force, which is due to the saturation gradient across the GDL. They proposed the formation of a tree-like liquid percolation in the GDL, similar to the mechanism proposed by Nam and Kaviany [48].

Litster et al. [75] developed a fluorescence microscopy technique to study liquid water transport mechanisms in the GDL. Based on the observations on the evolution of liquid water in several paths, they proposed that water transport in the GDL is dominated by fingering and channelling, and features numerous dead ends where water transport withdraws as an adjacent breakthrough channel forms. This contradicts with the mechanism proposed by Nam and Kaviany [48] and Pasaogullari and Wang [10].

Using fluorescence microscopy, Bazylak et al. [59] studied the liquid water transport in the GDL under compression and found that the compressed regions on the GDL sample provided preferential pathways for liquid water transport and breakthrough. They concluded that the formation of preferential pathways for liquid water transport was a result of compression in which the hydrophilic pathways for water transport were created due to the loss of hydrophobicity caused by compression. In another study with fluorescence microscopy, Bazylak et al. [76] observed water breaking through the GDL surface at preferential locations; however, the breakthrough locations change with time. They concluded that the change of breakthrough locations suggests a dynamic interconnection of water pathways within the GDL. Using confocal microscopy, Gao et al. [77] studied liquid water breakthrough behaviours and observed preferential breakthrough locations of liquid water on the GDL surface, similar to Bazylak et al. [59].

Lu et al. [78] studied liquid water breakthrough dynamics across the GDLs with and without MPL using an ex-situ setup. In the case of GDL without MPL, they observed multiple breakthrough events and dynamic breakthrough locations of liquid water on the GDL surface. They also observed that the capillary pressure peaks corresponded to breakthrough events and this agrees with the observations by Bazylak et al. [76] and Gao et al. [77]. The dynamic change of breakthrough locations observed in this study, however, opposes the pore network model in which water breaks through at the same location. In the case of GDL with MPL, multiple breakthrough events without shifting of breakthrough location were observed. The result suggests the role of MPL in stabilising water pathways in the GDL.

Using synchrotron X-ray radiography, Manke et al. [79] studied liquid water transport in an operating PEMFC and observed an eruptive transport mechanism [79] in which water droplets are abruptly and intermittently discharged from the GDL surface into the gas channel. This is similar to the phenomenon observed by Litster et al. [75].

Zhang et al. [80] utilised neutron imaging to examine the effect of different cathode GDLs on liquid water accumulation in an operating PEMFC. The results suggest that a carbon cloth GDL holds less water than paper GDLs. Using neutron imaging, Kowal et al. [81] compared liquid water saturation in carbon paper and carbon cloth GDLs and indicated that carbon paper GDLs retained more water under the channel land than carbon cloth GDLs.

Transparent fuel cells have also been employed to visualise the transport of liquid water; however, this method only allows the visualisation of liquid water after it has already been transported out of the GDL [46]. A number of studies have been conducted to observe water droplet formation and interactions on the surface of the GDL with different types of flow field channels, such as serpentine [82, 83] and straight [11, 83, 84].

1.5 Numerical Modelling of Fluid Transport in GDLs

Numerical models for fluid transport in the GDL can be classified into two groups: macroscopic models and pore-scale models. Macroscopic models treat GDL as

homogeneous material, whilst the pore-scale models employ real or simplified GDL microstructures for simulations [4]. As homogeneous material, the microstructure of the GDL is neglected in the macroscopic models. Effective transport properties of the material are utilised to reflect the effects of the neglected microstructure. In contrast, construction of the digital microstructure of GDL as a computational domain is required for pore-scale modelling [4]. Both models are discussed below.

1.5.1 Macroscopic Models

Macroscopic models have been developed and applied in order to predict gas and liquid distribution in PEMFCs. These models are based on the volumetric averaging theory, which assumes the GDL as a homogeneous material. Under the macroscopic nature assumption, these models fail to incorporate the influence of pore geometries of the GDL on fluid transport [85]. Below, the governing equations for both single- and two-phase flows are discussed.

1.5.1.1 Single-Phase Transport [86]

Transport of a single-phase flow with a single component

In a porous material under isothermal conditions, the bulk hydrodynamic behaviour of the single-phase single-component flow is described by the conservation of mass and momentum. The conservation of mass in porous material is given by:

$$\frac{\partial(\varepsilon\rho)}{\partial t} + \nabla \cdot (\rho u) = 0 , \tag{1.3}$$

where u is the superficial velocity which takes the porosity ε into account and is related to the average velocity in the pores by:

$$u = \varepsilon u_i \tag{1.4}$$

In a porous material, the transport of a single fluid is driven by the pressure gradient. The conservation of momentum is described by the generalised Darcy's equation as:

$$u = -\frac{K}{\mu}\nabla P, \tag{1.5}$$

where ∇P is the pressure gradient, K is the permeability, μ is the dynamic viscosity and $\frac{K}{\mu}$ is the viscous resistance. The Carman-Kozeny (CK) model is commonly used to determine the absolute permeability and is given as:

$$K = \frac{d_f^2 \varepsilon}{16 K_{CK} (1-\varepsilon)^2}, \tag{1.6}$$

where d_f is the fibre diameter and K_{CK} is the Carman-Kozeny constant, which is a specific material value emanating from a shape factor and a tortuosity factor [86].

Transport of a single-phase flow with two components

The transport of a single-phase flow with two components, such as hydrogen and water vapour at the anode, is described by Fick's law as:

$$n_A = \rho_A u - D_{AB}^{eff} \nabla \rho_A, \tag{1.7}$$

where n_A is the mass flux of component A, ρ_A is mass concentration, D_{AB}^{eff} is the effective diffusion coefficient of component A in the second component B and $\nabla \rho_A$ is the concentration gradient of component A. The effective diffusion coefficient is given as [4, 86, 87]:

$$D_{AB}^{eff} = \frac{\varepsilon}{\tau} D_{AB}, \tag{1.8}$$

where D_{AB}^{eff} and D_{AB} are the effective and bulk diffusion coefficients, and ε and τ are porosity and tortuosity of a porous medium respectively. Porosity is defined as the ratio of void volume in the total volume. Tortuosity defines the additional resistance to diffusion due to a tortuous flow path [4]. The relationship between tortuosity and porosity is generally given by Bruggeman's model as [4]:

$$\tau = \varepsilon^{-0.5} \tag{1.9}$$

Transport of a single-phase flow with more than two components

For a single-phase flow with more than two components, such as nitrogen, oxygen and water vapour at the cathode, the transport of each component is described by the Stefan-Maxwell equation for multiple component diffusion as:

$$\nabla c_i = \sum_{j=1, j\neq i}^{n} \frac{x_j N_i - x_i N_j}{D_{ij}^{eff}}, \tag{1.10}$$

where the subscribes i and j represent different species. c_i is molar concentration, n is the number of components, $x_{i,j}$ is the mole fraction, and $N_{i,j}$ is molar flux. D_{ij}^{eff} is the effective diffusion coefficient.

1.5.1.2 Two-Phase Systems [86]

In a two-phase system, the void space of a porous medium is occupied by two phases. The bulk porosity ε is a fraction of the void volume over the total bulk volume and is composed of the liquid ε_L and gas ε_G volume fractions. The saturation of liquid S_L is defined as the ratio of the volume occupied by liquid to the total void volume in the porous medium. Hence, saturation is noted in the range of zero to one. The relationship between porosity and saturation is given as follows:

$$\varepsilon_L + \varepsilon_G = \varepsilon \tag{1.11}$$

$$S_L = \frac{\varepsilon_L}{\varepsilon} \tag{1.12}$$

Hydrodynamics and capillarity in two-phase systems

In a two-phase system, the mass conservation equations for gas and liquid are described as [86]:

$$\frac{\partial(1-S_L)\varepsilon\rho_G}{\partial t} + \nabla\cdot(\rho_G u_G) = \dot{S}_G \tag{1.13}$$

$$\frac{\partial S_L \varepsilon \rho_L}{\partial t} + \nabla \cdot (\rho_L u_L) = \dot{S}_L, \tag{1.14}$$

where $(1 - S_L)\varepsilon$ and $S_L \varepsilon$ represent the volume of gas and liquid phases respectively. $\dot{S}_G$ and $\dot{S}_L$ are the volumetric sources of gas and liquid.

In the two-phase system, the momentum equation for each phase is described through Darcy's equation as:

$$u_G = -\frac{K_G}{\mu_G} \nabla P_G \tag{1.15}$$

$$u_L = -\frac{K_L}{\mu_L} \nabla P_L \tag{1.16}$$

Since there are five variables, S_L, u_G, u_L, P_G and P_L, the four equations above are not enough to evaluate these five variables. Hence, the concept of capillary pressure is introduced. Capillary pressure is the result of interfacial tension, which is the free surface energy between two immiscible phases. Capillary pressure is the pressure difference across the interface of the two immiscible phases, and in the case of gas and liquid it is defined as:

$$P_C = P_L - P_G \tag{1.17}$$

Based on the definition of capillary pressure, therefore, the momentum equations for gas and liquid phases can be described as:

$$u_G = -\frac{K_G}{\mu_G} \nabla P_G \tag{1.18}$$

$$u_L = -\frac{K_L}{\mu_L} \nabla P_G - \frac{K_L}{\mu_L} \nabla P_C \tag{1.19}$$

Another important characteristic of the two-phase flow in a porous medium is the fluid-solid interaction. This depends on interfacial tension and surface wettability.

When two immiscible fluids (e.g. a liquid and a gas) are in contact with a solid surface as shown in Fig. 1.4, at equilibrium, the angle θ between the interface of the two fluids and the solid surface can be described by Young's equation as [88]:

$$\sigma_{GL}\cos\theta = \sigma_{SG} - \sigma_{SL}; \qquad \cos\theta = (\sigma_{SG} - \sigma_{SL})/\sigma_{GL}, \tag{1.20}$$

where σ_{SG} is the interfacial tension between solid and gas, σ_{SL} is the interfacial tension between solid and liquid, and σ_{GL} is the interfacial tension between gas and liquid.

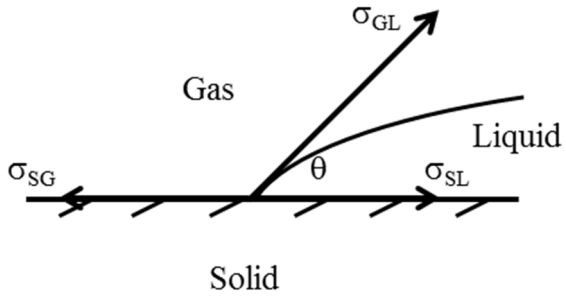

Figure 1.4 Interfacial tensions. Adapted after [88].

The angle θ is usually called the contact angle and $\sigma_{GL}\cos\theta$ is called adhesion tension. The latter determines which fluid is preferentially wetting the solid, spreads over it or adheres to it. This leads to the concept of wettability of a solid by a liquid. When one fluid is said to wet the solid surface, it is called wetting fluid while in the contrary event it is called non-wetting fluid [88].

In the case of an air-water system as in the GDL of the PEMFC, wettability is considered to be hydrophilic for $0°<\theta<90°$ and hydrophobic for $90°<\theta<180°$. The range $80°<\theta<100°$ is usually referred to as moderate, neutral or intermediate wettability. Fig. 1.5 shows different wetting conditions of the GDL surface.

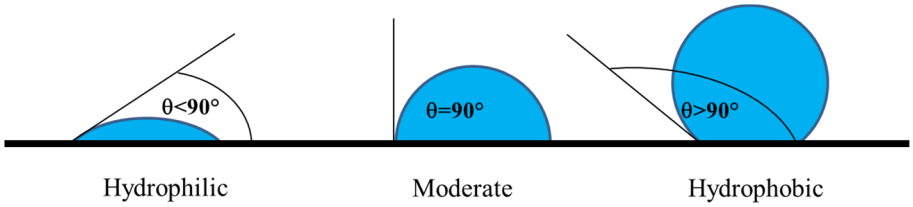

Figure 1.5 Illustration of different wetting conditions of the GDL represented by contact angles of liquid water on a GDL surface.

Capillary pressure P_C can also be described through the Young-Laplace's equation as [88]:

$$P_C = \Delta P = P_2 - P_1 = \sigma\left(\frac{1}{R_1} + \frac{1}{R_2}\right) = \frac{2\sigma}{R^*}, \tag{1.21}$$

where R_1 and R_2 are two principal radii of curvature in perpendicular directions, R^* is the mean radius of curvature and σ is the interfacial tension between liquid and gas. The two radii of curvature R_1 and R_2 are usually assumed to be identical to the radius of the sphere R. Therefore, the Young-Laplace equation becomes [88]:

$$\Delta P = \frac{2\sigma}{R} \tag{1.22}$$

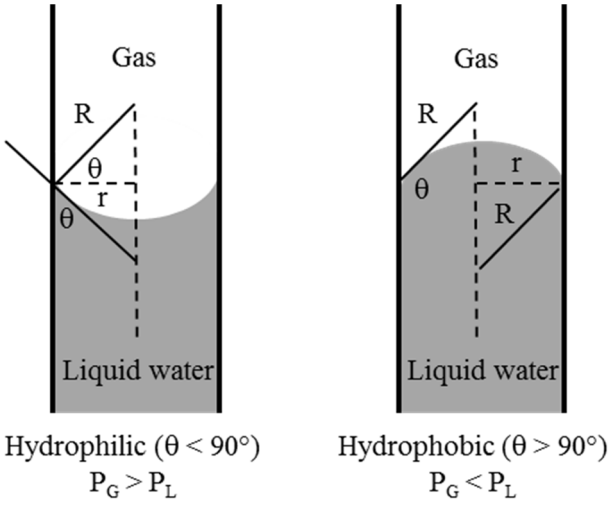

Figure 1.6 Liquid water and gas behaviours in small pores with different surface wettabilities. Adapted after [4].

In the GDL, liquid water transport is greatly affected by the pore walls due to its small pore sizes and, thus, the surface wettability of the GDL plays an important role in liquid water transport [4]. Fig. 1.6 shows the liquid-gas behaviours in small pores with different surface wetting characteristics, hydrophilic and hydrophobic, of the pore walls. As illustrated in Fig. 1.6, R can be replaced by:

$$R = \frac{r}{\cos\theta}, \tag{1.23}$$

where r is the radius of the pore and θ is the contact angle. This gives the capillary pressure P_C as a function of contact angle θ, pore size r and interfacial tension σ as:

$$P_C = \frac{2\sigma\cos\theta}{r} \tag{1.24}$$

As pore size decreases, the pressure necessary to push liquid water through the pore increases. Thus, a large pore requires less effort for liquid water to flow through it than a small pore.

Relative permeability

In a two-phase system, a gas and a liquid occupy the same pores in a porous medium, thus reducing the amount of pore space available for each phase. As a result, permeability must be attuned for the volume fractions occupied by each phase. The permeability of the two phases is described as [86]:

$$K_G = K_{RG} K \tag{1.25}$$

$$K_L = K_{RL} K \,, \tag{1.26}$$

where K is the single-phase permeability. K_{RG} and K_{RL} are the relative permeability for the gas and liquid phases respectively and are usually expressed as [86]:

$$K_{RG} = (1 - S)^3 \tag{1.27}$$

$$K_{RL} = S^3, \tag{1.28}$$

where S is the reduced saturation.

The models discussed above treat the GDL as a macro-homogeneous layer and rely on the averaged parameters such as permeability, tortuosity and effective diffusivity. In addition, the two-phase correlations, namely the capillary pressure-saturation and relative permeability-saturation relationships, are required for the models.

1.5.2 Pore-scale Models

Several pore-scale models have been extensively developed and applied to investigate fluid transport in the GDL. Such models can be classified into rule-based and first-principle-based models [4, 85]. The rule-based models incorporate physical rules to a simplified or real structure. The pore network (PN) models are the most widely used ruled-based models. To the contrary, the first-principle-based models rely on solving a set of governing equations, i.e. the Navier-Stokes (NS) equations. The conventional computational fluid dynamics (CFD), molecular dynamics (MD), lattice gas automata (LGA) and Lattice Boltzmann (LB) methods are in this category. The most prominent models among these first-principle models is the LB approach, since the MD models are

computationally very expensive, the LGA models generate large statistical noise and in the conventional CFD models it is still difficult to simulate fluid flow in the geometrically complex structure of the GDL [4, 85]. Below, the PN and LB models are discussed.

1.5.2.1 Pore Network Models

In the pore network (PN) models, the actual GDL microstructure is typically mapped into a network of wide pores and narrower throats. The shapes of pores and throats are usually simple so that the flow resistance through the pore network can be simply calculated [4]. Pores are commonly simplified to regular spherical or cubic pores connected by square or circular throats. The pore network can be created through a simple truncated Weibull cumulative distribution in which the distribution parameters can be adjusted to obtain the desired pore size distribution (PSD) [85]. A typical PN model simulates a drainage process in which liquid water displaces air that initially saturates the GDL by capillary force. Liquid water will proceed through the throats if the pressure difference across the interface between liquid water and air exceeds the capillary resistance and the pore will be invaded automatically due to its larger size [46]. In the PN model, the pressure drop across the pores and throats can be calculated based on a generalised Poiseulle law or Hagen-Poiseulle law [4, 89]. The PN models have been developed and applied by several researchers to investigate liquid water transport in the GDL at pore level [4, 46, 85].

Sinha and Wang [89] developed the PN model to simulate liquid water movement and flooding in a hydrophobic carbon paper GDL. They found that liquid water travels through the GDL in the form of connected clusters with finger-like water fronts and encounters several dead ends in the narrow regions. The results indicated that liquid water percolates through a path of least resistance. Using the extended PN model, Sinha and Wang [43] modelled liquid water transport in mixed-wettability GDLs and found that liquid water favourably flows through the connected GDL hydrophilic network of a mixed-wetted GDL, suppressing the fingering pattern observed in a fully hydrophobic GDL. They also indicated that the optimum hydrophilic pore fraction could provide the least mass transport losses.

Kuttanikkad et al. [44] conducted a similar study on the effect of mixed wettability in the GDL using the PN model and reported that the distributions of liquid

water in the GDL are slightly affected by the hydrophilic pore fraction as long as the fraction is below the threshold fraction (0.7 in their study). Conversely, the hydrophilic pore fraction becomes significant when the fraction is above the threshold fraction, which results in the greater blockage of pores by liquid water. Instead of assuming that the network throats at the inlet interface are in contact with the water reservoir, Wu et al. [45] combined the PN model with the multiple injections boundary conditions and found that the liquid water saturation profile along the GDL thickness changes only a little with the addition of hydrophilic pores when the hydrophilic fraction is low, whilst as the hydrophilic fraction increases beyond 0.4, a flat shape of saturation profile is observed.

Using the PN model, Gostick et al. [90] and Koido et al. [91] were able to predict the capillary pressure-saturation relationships for different carbon paper GDLs.

Markicevic et al. [92] utilised an invasion percolation PN model to study the effects of network structure on capillary pressure and relative permeability. The study showed that capillary pressure is strongly affected by the heterogeneity of the structure whilst the relative permeability significantly changes with saturation level. From the same group, Bazylak et al. [93] studied different designs of the 2D pore network. The study showed that the radial gradient pattern in the pore network is favourable due to a significant decrease in saturation level. Bazylak and co-workers [57] modelled commercial GDLs in 2D based on the heterogeneous porosity distribution input obtained through the X-ray tomography data and reported the dependence of the saturation profile on the porosity distribution profile. Using a similar method, again, Bazylak and co-workers [94] modelled commercial GDLs in 3D and demonstrated the strong dependence of the saturation profile on the porosity distribution profile. They indicated that the peaks and valleys presented in the porosity profile of the thick paper GDL may create high saturation regions in the GDL and suggested that GDLs should be designed to have smooth porosity distribution with few local minima.

Using the PN model, Nam and co-workers [95] indicated that capillarity is the main driving force behind the transport of liquid water in hydrophobic GDLs. In another work, Nam and co-workers [96] showed that the pore morphological factors of GDL, such as pore connectivity, play an important role in water distribution. The study showed that liquid water preferentially occupies pores with the largest size, displaying capillary

fingering flow in the hydrophobic GDLs. They also suggested that the saturation level can be lowered by reducing GDL thickness. More recently, Nam and co-workers [97] extended the PN model to study water distributions in hydrophobic GDLs where the outlet boundary was partially blocked by ribs of the flow field plate. The study showed higher water saturation in the under-rib region than in the under-channel region of the GDL.

Prat and co-workers [25] utilised the PN model with an invasion percolation algorithm to investigate liquid water invasion patterns in an idealised 2D pore network. The study indicated the reduction of liquid water saturation in a hydrophobic GDL. In another work, Prat and co-workers [98] studied the impact of GDL wettability on liquid water invasion in 2D pore network models and demonstrated the shift from stable displacement patterns to capillary fingering patterns with the change of wettability from hydrophilic to hydrophobic. Recently, Prat and co-workers [99] employed the invasion percolation type PN model to investigate the invasion pattern in a 2D network with multiple inlet injections. They observed a smaller number of breakthrough locations compared to the number of injection locations and concluded that the observed phenomenon is due to the internal front merging and cluster formation.

More recently, Tan et al. [100] employed the PN model with the invasion percolation algorithm to simulate liquid water penetration through carbon paper GDLs at different temperatures. They observed that liquid water has fixed flow paths and always breaks through at preferential locations. They also found that the breakthrough pressure for liquid water decreases linearly with the increase of temperature. The results from the PN model were also compared with the experiment results and showed good agreement.

As the literature suggested, the PN models provide more fundamental understanding of liquid water transport processes and distribution in the GDL under various conditions, which cannot be obtained from macroscopic models; however, the PN models still rely on idealised models of the GDLs that cannot fully replicate the actual GDL.

1.5.2.2 Lattice Boltzmann Method

The LB method is a numerical model based on kinetic theory that has been developed for simulating fluid flow. Unlike the conventional CFD method, the LB method does not directly solve the partial differential equations. Instead, LB tracks the propagation and collision of a number of fictitious particles in a lattice domain under the rule that the collisions conserve mass and momentum. Macroscopic properties, such as fluid density and velocity, are calculated by summing the corresponding moments of all the particles at each node in the lattice domain [19, 46]. The LB models used in this thesis will be described in detail in Chapter 2.

With its kinetic nature, the LB method is capable of dealing with complex geometric boundaries and various forces at microscopic scale and is, therefore, convenient for simulating flow through heterogeneous porous structures like the GDL. The LB method is able to incorporate phase separation and interfacial tension in multiphase flows which are difficult to implement in conventional CFD [85, 101].

A number of studies employed the LB model to study gas flows through GDL structures. Hao and Cheng [67], Nabovati et al. [68] and Van Doormaal and Pharoah [102] determined gas permeability of digitally reconstructed carbon paper GDLs using the single-phase LB model. Rama et al. and Ostadi et al. [19, 60, 69, 103-110] characterised gas permeability, tortuosity and diffusivity in X-ray reconstructed carbon paper and carbon cloth GDLs using the single-phase LB model.

Apart from the single phase LB model, several LB models have been developed to simulate two-phase flows. Gunstensen et al. [111] proposed a LB model based on the two-component lattice gas model. The model used two coloured particles to separate the two phases and used a perturbation to recover approximately Laplace's law at the interface. This model, however, is not strictly based on thermodynamics and it is therefore difficult to add microscopic physics into the model [31, 112, 113]. Shan and Chen [114, 115] developed a LB model based on the interaction potential for multi-phase and multi-component fluid flow systems. This model, commonly referred to as SC model, incorporates a non-local interaction force between particles of different fluids at neighbouring lattices [31, 85, 113] in order to generate phase separation, which occurs

automatically if the interaction strength exceeds the critical value [101]. The SC model does not conserve momentum locally but globally. The main drawback of the SC model is that it cannot handle fluids with large density ratios [31]. Swift et al. [116, 117] proposed a multi-phase, multi-component LB model based on the free energy approach. In this approach, the equilibrium distribution functions are modified by adding an additional constraint [113]. The free energy model satisfies conservation of mass and momentum locally and globally. This model, however, does not satisfy Galilean invariance resulting in a serious drawback due to unphysical effects in simulations [85, 118]. Other LB models for simulating two-phase flows found in the literature include He et al. [119], Zheng et al. [120] and Inamuro et al. [121]. He et al. [119] developed a multi-phase LB model using the kinetic equation for multi-phase flow systems, whilst Zheng et al. [120] and Inamuro et al. [121] proposed a LB model for modelling two-phase fluids with large density differences. Among the various two-phase models mentioned above, the SC model is the most widely used because of its simplicity in dealing with boundary conditions in complex structures and phase separation [85]. Several studies have applied the two-phase LB models to investigate liquid water transport behaviours in the GDLs at a pore level.

Mukherjee et al. [122] utilised the SC-LB model to study two-phase transport and flooding behaviour in the GDL and CL. Their work demonstrated that the LB simulation is able to reveal the complicated liquid water dynamics, including droplet interactions, water front formation and propagation through the hydrophobic GDL. In another study, Mukherjee et al. [123] extended the model to study the influence of compression on two-phase transport and flooding behaviours. The result showed a greater resistance to liquid water transport in the in-plane direction due to the increased tortuosity of the compressed GDL. In another recent study, Mukherjee et al. [42] also examined the impact of durability on flooding behaviour by comparing the randomly distributed mixed wettability GDL with the purely hydrophobic GDL.

Koido et al. [91] utilised the SC-LB model to examine water distribution in a carbon paper GDL and evaluated the relative permeability as a function of water saturation. Niu et al. [124] considered the influence of pressure gradients and hydrophobicity by evaluating relative permeability and saturation relations using the LB

model based on the diffuse interface theory. Park and Li [125] used a 2D SC-LB model to study two-phase behaviour in a slice of a paper GDL, whilst Tabe et al. [126] also used a 2D model to discover liquid water invasion patterns in a simplified GDL using the model proposed by Inamuro et al. [121] based on the free energy approach.

Using the SC-LB model, Zhou and Wu [127] examined the liquid water configuration of a simplified 2D GDL with different surface wettabilities, including fully hydrophilic, fully hydrophobic and 50% hydrophobic, with different wettability arrangements. The study showed that liquid water distribution was completely different even though the fibre fraction was identical, indicating that the fraction of hydrophobic fibres alone cannot describe the transport characteristics of liquid water in the GDL.

Hao and Cheng [29] utilised the LB model based on the free energy approach to investigate the effect of surface wettability by simulating liquid water invasion in a carbon paper GDL with uniform and non-uniform wettability. For the uniform wettability case, their results indicated a decrease in the saturation level of liquid water in the GDL with more hydrophobicity. For the non-uniform wettability case, the results indicated that water preferentially passed through the hydrophilic passages in the GDL, which is in agreement with the results from the PN models in [43].

Using the SC-LB model, Chen et al. [128, 129] investigated the effects of channel land on liquid water behaviour and distribution in the 2D GDL and gas channel and found that a hydrophilic GC leads to less liquid water accumulation in the GDL than a hydrophobic GC.

Moriyama and Inamuro [130] examined the effects of surface wettability of the GDL and channel walls on liquid water distribution in the GDL and GC by applying the two-phase LB model for high density ratio originally proposed by Inamuro et al. [121]. The results indicated that the liquid water preferentially travels through small pores in the hydrophilic GDL and large pores in the hydrophobic GDL. In addition, the study suggested that more water accumulates under rib than under channel and that the water under the rib can be lessened by shifting the wettability of the channel wall from hydrophilic to hydrophobic.

Using the SC-LB model, Molaeimanesh and Akbari [131] investigated the effects of GDL wettability and its wettability gradients on the behaviour of a water droplet during removal from a GDL. For a uniform wettability GDL, they concluded that increasing hydrophobicity of the GDL facilitates the removal of the water droplet and decreases the remaining water in the GDL. For a GDL with gradient wettability, they found that the decreasing hydrophobicity towards the outlet eases water droplet motion in the GDL. In another recent work, Molaeimanesh and Akbari [132] examined droplet removal in four GDLs with different PTFE distributions in which all fibres were coated by PTFE in the first case, while some portions of carbon fibres were left uncoated in the other three cases. The overall PTFE in all cases was equally at 20% wt. The results showed that the lack of PTFE coating even in a small region could severely prohibit droplet removal from the GDL.

The microstructures in the studies above were mostly reconstructed using stochastic simulation techniques. The stochastic method operates by using a set of structural inputs obtained from specifications or measured data to construct a porous medium [85, 122]; in any case, however, it is not able to replicate fully an actual GDL sample. The stochastic technique also struggles to model the binding material that holds the fibres together in carbon paper. The binding material is either seen as a thin film or a rough surface. Many modelling techniques ignore the binder but it is known to alter the pore size and shape. In addition, several assumptions are made which make the stochastic model more unrealistic. For these reasons, more effort has been spent studying the GDL using X-ray computed tomography (XCT). Rama et al. [19] conducted a study on the feasibility of using the combined methods of XCT and LB to simulate fluid flow at the pore level in the GDL. The XCT method was used to generate, process and reconstruct a 3D image of a carbon paper GDL sample. The LB solver was then applied to simulate the gas velocity field in the void space of the GDL. The simulated velocity was then used to obtain the permeability. The simulated result was compared with the experimental result using a Frazier air tester and the error of the simulation study was found to be only 3% greater than that measured. The experimenters concluded that the agreement between the two results indicated that the combination of XCT and LB could capture accurately the microstructure of the GDL and the fluid flow through it. The study also showed that the combined techniques displayed a detailed description of flow paths, which would be

impossible to gain through measured experiments. This, along with other studies [30, 31, 60, 69, 103-110], showed that using XCT to generate 3D microstructures provides great promise towards more realistic structural delineation and pore-scale modelling of fluid transport in the GDLs.

1.6 Aims and Objectives

The GDL has a crucial role in the performance, durability and successful operation of PEMFCs. The GDL provides pathways for reactant gases to be transported from a gas supply channel to a catalyst layer, and product water to be removed from the catalyst layer to the gas channel. It is generally known that effective removal of product water from the catalyst layer through the GDL can prevent mass transport loss due to the blockage of available pore spaces by liquid water. It has been found that the wettability of the GDL is one of the most important properties of the GDL that strongly influence liquid water transport in the GDL. The effects of wettability on liquid water transport in the GDL have been studied widely, both experimentally and numerically. Among different numerical models, the Lattice Boltzmann (LB) method with its capability of dealing with complex geometric boundaries has emerged as a powerful tool for investigating flows in heterogeneous porous structures like the GDL. Comparisons between liquid water transport behaviours in different GDL structures using the LB method, however, are rare since only a single GDL material is utilised in most studies in the literature. The X-ray imaging technique has been recently utilised to generate 3D representative structures of GDL samples for the LB simulation. The high computational demand of the LB method, however, together with the commonly used highest available resolution of the X-ray images has limited its application to the analysis of only a very small volume of GDLs. With high resolutions, the LB flow simulation is also extremely time-consuming.

This thesis aims to develop the understanding of liquid water transport in the GDL materials with morphologically different structures under varying wettability conditions through the application of the LB and the X-ray computed tomography methods.

GDLs with paper and felt structures are reconstructed into 3D digital volumetric models via the X-ray computed tomography process. The digital models are then

incorporated into a two-phase LB solver to model water saturation distribution through the GDL domains.

To achieve the aim set out above, the specific objectives of this thesis are as follows:

1. To determine the optimum image resolution of an X-ray-reconstructed GDL sample through gas permeability simulation using the single-phase LB model in order to provide a guideline for selecting a resolution when generating X-ray images. This will be utilised in subsequent studies.
2. To characterise the material properties (i.e. thickness, porosity, permeability and tortuosity) of the newly X-ray-reconstructed models of different GDL samples based on tomography images of each sample and an analytical model available in the literature, and to validate them against the data in the literature.
3. To characterise the permeability and tortuosity of the GDL samples using the single-phase LB model, compare the average value of each property with the value obtained from the analytical model and validate the values of those properties against data in the literature.
4. To investigate the effects of GDL structures on liquid water transport behaviours, including invasion patterns, saturation distribution and breakthrough behaviour, under varying wettability conditions using the two-phase Shan-Chen (SC) LB model.

Chapter 2
Lattice Boltzmann Method

2.1 Introduction

The Lattice Boltzmann (LB) method is a numerical model that has been developed and increasingly utilised in the past two decades for simulating fluid flows. The LB model, which is based on kinetic theory, describes a fluid as a collection of particles moving and interacting through collisions [133]. The basic idea behind the LB method is to construct simplified kinetic models that incorporate the physics of microscopic processes so that the average macroscopic properties obey the macroscopic equations [133, 134]. It is largely different to the conventional continuum-based CFD methods, as it does not solve the partial differential equations (PDEs) directly. Instead, the LB model is designed to track the propagation and collision of a number of fictitious particles in a lattice domain under collision rules in which mass and momentum are conserved [19]. Macroscopic properties, such as fluid density and velocity, are obtained by summing up the corresponding moments of all particles at each lattice node [19]. Its major advantage over the conventional CFD methods is that it is capable of dealing with complex geometries, which is extremely difficult for the conventional CFD methods [101].

The LB method is originally derived from the Lattice Gas Automata (LGA) [114, 115, 135-140]. In the LGA model, space, time and particle velocities are all discrete [133]. Fluid particles move only along a lattice matrix and collide with each other on each lattice site according to some designed collision rules in which mass and momentum are conserved [115, 135]. Using Boolean variables, the LGA model defines the occupation of particles in a lattice matrix with either zero or one. It also includes an exclusion rule, which prevents two particles residing at the same lattice node. LGA configures the evolution of each particle at each time step through streaming and collision steps. The streaming step moves each particle to its nearest node in the direction of its velocity and the collision step controls the interaction of particles arriving at a node through scattering rules [133, 134]. While it also offers a simple and efficient method to model fluid flows, a major drawback is its large statistical noise [115]. This issue is solved by an alternative

approach, the LB method, which was developed from LGA. In order to suppress the statistical noise, McNamara and Zanetti [141] introduced the modelling of LGA with a LB equation [135]. In the LB model, instead of the discrete particles, the mean population is used to model fluid flows [135]. A particle in the LGA model, which is represented by a Boolean number, is replaced by the particle distribution function represented by any real number between zero and one [137]. In addition to the elimination of statistical noise, the unphysical artefacts in the original LGA model, the velocity-dependent pressure term and the lack of Galilean invariance, can be removed when a single-relaxation time collision term with a proper equilibrium distribution function is used in the LB equation [135, 142, 143]. Through a Chapmann-Enskog analysis, it can recover fully the governing continuity and Navier Stokes equations at the macroscopic scale [101, 142-144].

With its kinetic nature, the LB method provides many advantages, including clear physical pictures, ease of boundary conditions implementation and full parallelism [133], and has been suggested to be particularly useful in applications involving interfacial dynamics and complicated boundaries, such as multiphase flows in porous media [85, 145]. Recently, the LB method has been increasingly utilised to investigate fluid transport processes in porous structures of PEMFC GDLs [19, 30, 31, 60, 69, 103-110]. In this thesis, the LB model is used to simulate gas and liquid phase flow through the GDLs of a PEMFC.

2.2 Lattice Structure

In order to recover the Navier-Stokes equation at the macroscopic scale, the symmetry of the lattice structure is essential [133, 138]. The terminology DmQn is used to note which lattice structure is used in the LB model, where m denotes the dimension of the lattice structure and n indicates the number of discrete velocities. For example, the D3Q19 model is a three-dimensional cubic lattice structure in which fluid particles can move in nineteen velocity directions. In the lattice domain, the space is discretised into a number of squares in 2D domain and cubes in 3D domain. For 2D models, there are several 2D structures including D2Q4, D2Q5, D2Q7 and D2Q9. Among these 2D models, the D2Q9 is commonly used for flow simulations [134]. For 3D models, the three most common types are the D3Q15, D3Q19 and D3Q27 [112]. The D3Q15 and D3Q19 are the most

popular schemes for simulating flows in complex geometries but have less stability and accuracy when compared to the D3Q27 scheme. The D3Q27, however, demands extra computational effort. By far the most common is the D3Q19 scheme. The D2Q9 and D3Q19 models are shown in Fig. 2.1 and Fig. 2.2 respectively.

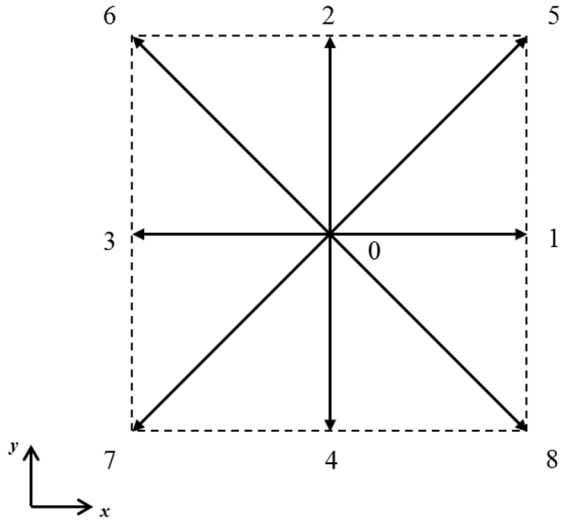

Figure 2.1 The D2Q9 lattice model.

For the D2Q9 model, at each lattice site there are 9 velocities for the particles at the origin to move in 2D, as shown in Fig. 2.1, which are defined as follows:

$$\xi_i = \begin{cases} (0,0)/\delta t, & i = 0, \\ (\pm \delta x, 0)/\delta t,\ (0, \pm \delta x)/\delta t, & i = 1-4, \\ (\pm \delta x, \pm \delta x)/\delta t, & i = 5-8 \end{cases} \tag{2.1}$$

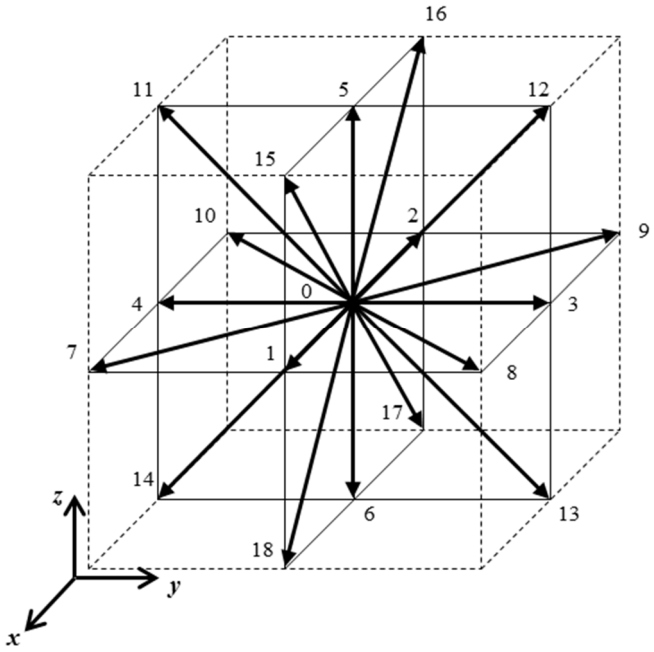

Figure 2.2 The D3Q19 lattice model.

For the D3Q19 model, at each lattice site there are 19 velocities for the particles at the origin to move in 3D, as shown in Fig. 2.2, which are defined as follows:

$$\xi_i = \begin{cases} (0,0,0)/\delta t, & i = 0, \\ (\pm \delta x, 0, 0)/\delta t, (0, \pm \delta x, 0)/\delta t, (0, 0, \pm \delta x)/\delta t, & i = 1-6, \\ (\pm \delta x, \pm \delta x, 0)/\delta t, (\pm \delta x, 0, \pm \delta x)/\delta t, (0, \pm \delta x, \pm \delta x)/\delta t, & i = 7-18 \end{cases} \tag{2.2}$$

2.3 Lattice Boltzmann Equation

The Lattice Boltzmann equation can be obtained from a discrete kinetic equation for the particle distribution function [133]. The LB equation is described as follows:

$$f_i(x + \xi_i \delta t, t + \delta t) = f_i(x, t) + \Omega_i(f(x, t)), \qquad i = 0, 1, 2, ..., M \tag{2.3}$$

where $f_i(x,t)$ is the particle distribution function, which defines the mass of a particle at location x and time t moving with the velocity ξ_i along the direction i. $\Omega_i(f(x,t))$ is the collision operator representing the change rate of $f_i(x,t)$ due to collision, which is usually simplified by the single-relaxation-time Bhatnagar-Gross-Krook (BGK) approximation [146, 147]. δt is the time increment. The fluid density and momentum are defined as:

$$\rho = \sum_i f_i \qquad \rho u = \sum_i f_i \xi_i \tag{2.4}$$

The collision operator $\Omega_i(f(x,t))$ is required to satisfy the conservation of total mass and total momentum at each lattice site [133].

$$\sum_i \Omega_i(f(x,t)) = 0 \qquad \sum_i \Omega_i(f(x,t))\xi_i = 0 \tag{2.5}$$

The LB method is implemented through two sequential steps, a collision step and a streaming step. In a collision step, the term on the right-hand side of Eq. (2.3) is calculated as:

$$f_i^*(x,t) = f_i(x,t) + \Omega_i(f(x,t)). \tag{2.6}$$

In the streaming step, the outcomes of collisions $f_i^*(x,t)$ are moved from location x to the nearest location $x + \delta t \xi_i$ along their direction of motion at time $t + \delta t$ to become $f_i(x + \delta t \xi_i, t + \delta t) = f_i^*(x,t)$.

After both the collision and streaming steps have been completed, the fluid densities and velocities for each lattice site can be updated through $\rho(x,t+\delta t) = \sum_i f(x,t+\delta t)$ and $\rho u = \sum_i f_i(x,t+\delta t)\xi_i$ respectively [19]. Another collision interaction also appears during the streaming step, which is the interaction between the particles and solid walls at the fluid-solid boundaries. In this case, the bound-back method is utilised. This method assumes that any particle that collides with the solid boundary bounces back to its original position. This method is discussed in the following section.

2.4 Single Relaxation Time Lattice Boltzmann Model

The simplest Lattice Boltzmann model is the Lattice Bhatnagar-Gross-Krook (BGK) model, which linearly approximates the collision operator Ω_i based on a single relaxation time towards the local equilibrium [133, 146, 148]. The BGK model [146] has become the most popular LB model due to its simplicity [142, 143, 148] and its computational efficiency [133], and has been suggested by several authors [133, 149]. In the BGK model, the local equilibrium distribution is chosen in order to recover the Navier-Stokes equations [133, 142, 143]. The BGK approximation or BGK collision operator [134] is given by:

$$\Omega_i(x,t) = -\frac{1}{\tau}\left[f_i(x,t) - f_i^{eq}(x,t)\right] \tag{2.7}$$

Therefore, the single relaxation time (SRT) Lattice Boltzmann model based on the BGK approximation is described as follows:

$$f_i(x+\xi_i\delta t, t+\delta t) = f_i(x,t) + \frac{1}{\tau}\left[f_i^{eq}(x,t) - f_i(x,t)\right] \tag{2.8}$$

where $f_i(x,t)$ is the particle distribution function which defines the mass of a particle at location x and time t moving with the velocity ξ_i along the direction i, $f_i^{eq}(x,t)$ is the equilibrium distribution function and τ is the dimensionless relaxation parameter that controls the rate at which $f_i(x,t)$ approaches $f_i^{eq}(x,t)$. δt is the time increment. For the D3Q19 LB scheme, the velocity ξ_i is defined as follows:

$$\xi_i = \begin{cases} (0,0,0)/\delta t, & i = 0, \\ (\pm\delta x,0,0)/\delta t, (0,\pm\delta x,0)/\delta t, (0,0,\pm\delta x)/\delta t, & i = 1-6, \\ (\pm\delta x,\pm\delta x,0)/\delta t, (\pm\delta x,0,\pm\delta x)/\delta t, (0,\pm\delta x,\pm\delta x)/\delta t, & i = 7-18 \end{cases} \tag{2.9}$$

where δx is the element length. The equilibrium distribution function $f_i^{eq}(x,t)$ is the value of $f_i(x,t)$ under a state of equilibrium, which can be expressed as a discretisation of the Maxwell-Boltzmann equilibrium distribution [101, 143]. The $f_i^{eq}(x,t)$ for the D3Q19 model is given by:

$$f_i^{eq}(x,t) = w_i \rho \left[1 + \frac{\xi_i \cdot u}{c_s^2} + \frac{1}{2}\left(\frac{\xi_i \cdot u}{c_s^2} \right)^2 - \frac{u \cdot u}{2c_s^2} \right] \tag{2.10}$$

where w_i is a weighting factor depending on the magnitude of the velocity ξ_i ($w_i = 1/3$ for $|\xi_i| = 0$, $w_i = 1/18$ for $|\xi_i| = \delta x / \delta t$ and $w_i = 1/36$ for $|\xi_i| = \sqrt{2}\delta x / \delta t$), c_s is the speed of sound and is given by $c_s = \frac{1}{\sqrt{3}} \delta x / \delta t$, ρ and u are fluid density and velocity respectively and can be calculated by:

$$\rho = \sum_i f_i \tag{2.11}$$

$$\rho u = \sum_i f_i \xi_i \tag{2.12}$$

The fluid viscosity is related to relaxation time τ by $\nu = \delta x^2 (\tau - 1/2)/3\delta t$ and pressure expressed as $P = c_s^2 \rho = \frac{\delta x^2 \rho}{3\delta t^2}$.

2.5 Multiple Relaxation Time Lattice Boltzmann Model

The BGK LB model has some deficiencies, such as numerical instability and viscosity dependence of boundary locations particularly for simulating flow in porous media [103, 150]. In order to overcome the deficiencies in the BGK model, a multiple-relaxation-time (MRT) LB model has been developed. In the MRT model, the single relaxation time parameter in the BGK model is replaced by a collision matrix, which allows different relaxation times to be independently tuned in order to improve numerical stability and accuracy [103, 105, 148, 150]. The MRT LB model is described as follows [148, 150]:

$$f_i(x + \xi_i \delta t, t + \delta t) - f_i(x,t) = S\left[f_i^{eq}(x,t) - f_i(x,t) \right] \tag{2.13}$$

where $f_i(x,t)$ is the particle distribution function which defines the mass of a particle at location x and time t moving with the velocity ξ_i along the direction i, $f_i^{eq}(x,t)$ is the equilibrium distribution function, δt is the time increment and S is the collision matrix.

$$f_i\left(x+\xi_i\delta t, t+\delta t\right)-f_i\left(x,t\right)=M^{-1}\hat{S}\left[m^{eq}\left(x,t\right)-m\left(x,t\right)\right] \tag{2.14}$$

where $\hat{S}=M\cdot S\cdot M^{-1}$ is a diagonal collision matrix which determines different rates for different moments, M is a transformation matrix which transforms the particle distribution functions $f_i(x,t)$ into moments $m\left(x,t\right)$, and $m^{eq}\left(x,t\right)$ is the equilibrium value of the moment $m\left(x,t\right)$. For the D3Q19 model, the diagonal collision matrix $\hat{S}$ is given by [30, 31]:

$$\hat{S}=diag\left(s_0,s_1,s_2,s_3,s_4,s_5,s_6,s_7,s_8,s_9,s_{10},s_{11},s_{12},s_{13},s_{14},s_{15},s_{16},s_{17},s_{18}\right) \tag{2.15}$$

where

$$\begin{aligned}
&s_{0,k}=s_{3,k}=s_{5,k}=s_{7,k}=0,\\
&s_{1,k}=s_{2,k}=s_{9,k-15,k}=1/\tau,\\
&s_{4,k}=s_{6,k}=s_{8,k}=s_{16,k-18,k}=8\left(2-1/\tau\right)/\left(8-1/\tau\right),
\end{aligned} \tag{2.16}$$

in which τ is a relaxation parameter which is related to the viscosity of fluid. The transformation from velocity to moment space is as follows [150]:

$$m=M\cdot f,\qquad f=M^{-1}\cdot m \tag{2.17}$$

For the D3Q19 model, the matrix M is given in [148] and the 19 moments are given as [148, 150]:

$$m=\left(\rho,e,\varepsilon,j_x,q_x,j_y,q_y,j_z,q_z,3p_{xx},3\pi_{xx},p_{ww},\pi_{ww},p_{xy},p_{yz},p_{xz},m_x,m_y,m_z\right)^T \tag{2.18}$$

The corresponding 19 moments are mass density $\left(m_0=\rho\right)$, the part of kinetic energy independent of density $\left(m_1=e\right)$, the part of kinetic energy square $\left(m_2=\varepsilon=e^2\right)$, momentum $\left(m_{3,5,7}=j_{x,y,z}\right)$, the energy flux independent of the mass flux $\left(m_{4,6,8}=q_{x,y,z}\right)$, the symmetric traceless viscous stress tensor $\left(m_9=3p_{xx},m_{11}=p_{ww},m_{13,14,15}=p_{xy,yz,xz}\right)$, the quartic order moments $\left(m_{10}=3\pi_{xx},m_{12}=\pi_{ww}\right)$ and the cubic order moments

$\left(m_{16,17,18} = m_{x,y,z}\right)$. Among these quantities, only density $\rho = \sum_i f_i$ and momentum $j = \left(j_x, j_y, j_z\right) = \sum_i f_i \xi_i$ are conserved quantities, whilst the rest are non-conserved quantities for athermal fluids [148, 150]. The equilibria $m^{eq}\left(\rho, j\right)$ for the non-conserved moments are given as: [148, 150]

$$e^{eq} = -11\rho + \frac{19}{\rho_0} j \cdot j = -11\rho + \frac{19}{\rho_0}\left(j_x^2 + j_y^2 + j_z^2\right),$$

$$\varepsilon^{eq} = 3\rho - \frac{11}{2\rho_0} j \cdot j,$$

$$q_x^{eq} = -\frac{2}{3} j_x,\ q_y^{eq} = -\frac{2}{3} j_y,\ q_z^{eq} = -\frac{2}{3} j_z,$$

$$p_{xx}^{eq} = \frac{1}{3\rho_0}\left[2j_x^2 - \left(j_y^2 + j_z^2\right)\right],\ p_{ww}^{eq} = \frac{1}{\rho_0}\left[j_y^2 - j_z^2\right],$$

$$p_{xy}^{eq} = \frac{1}{\rho_0} j_x j_y,\ p_{yz}^{eq} = \frac{1}{\rho_0} j_y j_z,\ p_{xz}^{eq} = \frac{1}{\rho_0} j_x j_z,$$

$$\pi_{xx}^{eq} = -\frac{1}{2} p_{xx}^{eq},\ \pi_{ww}^{eq} = -\frac{1}{2} p_{ww}^{eq},$$

$$m_x^{eq} = m_y^{eq} = m_z^{eq} = 0.$$

The kinematic viscosity of the fluid is given by $\nu = \delta x^2\left(\tau - 1/2\right)/3\delta t$.

2.6 Boundary Treatment

Like any other numerical method, proper boundary conditions are necessary for simulating fluid flow using the LB model. In the LB model, the boundary conditions must be implemented by specifying the unknown incoming particle distribution functions $f_i\left(x,t\right)$ which enter the domain across boundaries [101]. Below, the boundary conditions employed in this thesis are discussed.

In the LB model, the fluid-solid boundary comes into effect when fluid particles hit solid boundaries during the streaming step [104]. The interface between fluid and solid is usually assumed to be a non-slip boundary in which the fluid velocity is assumed to be zero at a given interface [103, 105, 151]. The interface is also assumed to be aligned with the lattice site [151]. The bounce-back scheme for no-slip boundary conditions is commonly used to solve the fluid-solid interface by assuming that any particle that hits a solid wall during the streaming step is simply bounced back to its original location in the opposite direction with the same speed [103, 105], as shown in Fig 2.3. This simplicity of the bounce-back method is ideal for simulating fluid flows in complicated geometries, such as porous media [133].

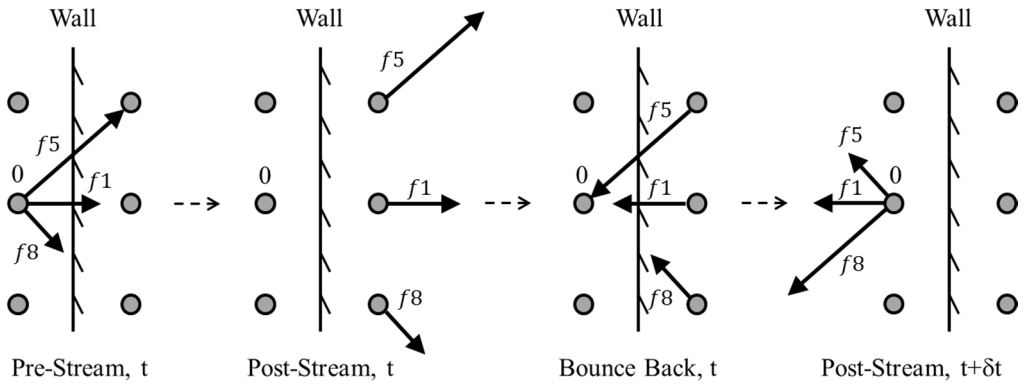

Figure 2.3 Illustration of the mid-plane bounce-back process on a non-slip boundary. Adapted after [152].

The particles $f_1(0,t)$, $f_5(0,t)$ and $f_8(0,t)$ at site 0 are streaming towards the solid wall, which is located halfway between the fluid and solid sites. These particles hit the wall at time $t+\frac{\delta t}{2}$ and then bounce back to their original position at time $t+\delta t$ with the same speed, as illustrated in Fig. 2.3.

Another common boundary condition employed for fluid flow systems is the periodic boundary condition. Periodic boundary conditions form the simplest type of

boundary conditions. The basic idea is that any particle leaving the domain from one face with certain properties returns to the opposite face of the domain with the same properties, as illustrated in Fig. 2.4.

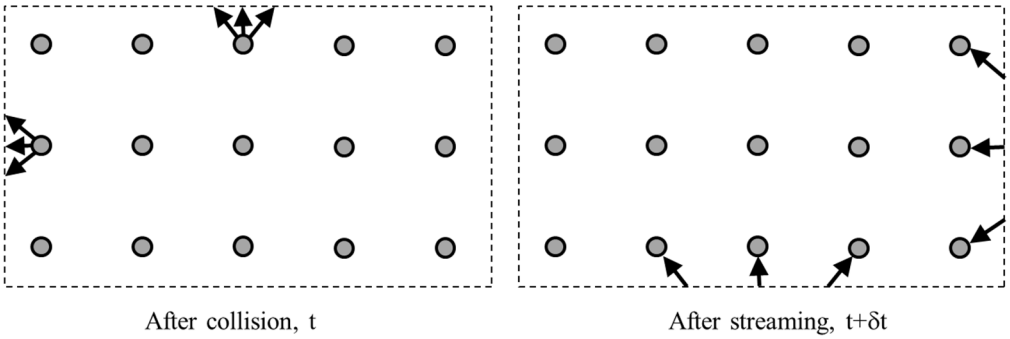

Figure 2.4 Illustration of the periodic boundary condition. Particles leaving the domain on the left and top boundaries, re-enter the domain on the right and bottom boundaries respectively. Adapted after [101].

Pressure boundary is another boundary condition commonly used in fluid flow simulations. In the LB model, fluid pressure is related to fluid density as $P = c_s^2 \rho$. Hence, a given pressure is comparable to a given density at the boundary, which can be solved by the method proposed by Zou and He [153], based on the bounce-back of the non-equilibrium distribution part of the particle distribution functions in the normal direction [103, 105, 153]. Supposing that the pressure is applied in z direction, the distribution functions f_5, f_{11}, f_{12}, f_{15}, f_{16} are from outside of the domain, which is unknown, as shown in Fig 2.2. The unknown incoming distribution functions at the inlet boundary can be expressed as [103-105, 152, 153]:

$$f_5 + f_{11} + f_{12} + f_{15} + f_{16} = \rho_{in} - \begin{pmatrix} f_0 + f_1 + f_2 + f_3 + f_4 + f_6 + f_7 + f_8 \\ + f_9 + f_{10} + f_{13} + f_{14} + f_{17} + f_{18} \end{pmatrix} \qquad (2.19)$$

where ρ_{in} is the density of fluid at the inlet boundary. If the velocity component in z direction is u_z, the momentum in z direction is given as:

$$f_5 + f_{11} + f_{12} + f_{15} + f_{16} = \rho_{in} u_z + \left(f_6 + f_{13} + f_{14} + f_{17} + f_{18}\right) \tag{2.20}$$

The two equations give:

$$\begin{aligned} \rho_{in} = {} & \frac{1}{1-u_z}\left(f_0 + f_1 + f_2 + f_3 + f_4 + f_7 + f_8 + f_9 + f_{10}\right) \\ & + 2\left(f_6 + f_{13} + f_{14} + f_{17} + f_{18}\right) \end{aligned} \tag{2.21}$$

The assumption of bounce-back for the non-equilibrium part of the particle distribution proposed by Zou and He [153] is:

$$f_i = f_i^{eq} + \left(f_{i'} - f_{i'}^{eq}\right) \tag{2.22}$$

where $f_{i'}$ is the particle distribution function in the i' direction. The unknown incoming distribution functions f_5, f_{11}, f_{12}, f_{15}, f_{16} can be expressed as [103-105, 153]:

$$f_i^* = \frac{f_i - \left(j_x / \xi_{ix} + j_y / \xi_{iy}\right)}{2}, \quad i = 5, 11, 12, 15, 16 \tag{2.23}$$

where $j_x = \sum_{i=0}^{18} f_i \xi_{ix}$ and $j_y = \sum_{i=0}^{18} f_i \xi_{iy}$. This allows the pressure boundary condition to be imposed at the boundary of the domain.

2.7 Conclusions

In this chapter, the single relaxation time (SRT) LB model based on the BGK approximation, the multiple relaxation time (MRT) LB model, the lattice structures and the boundary treatment were described. The SRT model will be used in Chapter 4 for characterising gas permeability in X-ray reconstructed images of a carbon paper GDL at various resolutions, and for characterising gas permeability and tortuosity of different GDL materials in Chapter 6. Subsequently, the MRT model will be used in Chapter 7 to simulate liquid water transport behaviours in the GDL structures. The D3Q19 lattice model will also be coupled with both the SRT and MRT models. The bounce-back

scheme for the non-slip boundary, the periodic boundary and the pressure boundary will be implemented in order to specify the unknown incoming particle distribution functions for the LB simulations throughout the aforementioned chapters.

Chapter 3
X-ray Computed Tomography Imaging Technique

3.1 Introduction

X-ray computed tomography is a non-invasive and non-destructive imaging technique, which allows the 3D visualisation of an internal structure of an object from a set of X-ray shadow images, commonly called projections [154]. The projections are produced based on the level of X-ray attenuation, which corresponds to the density of the object [106, 154]. The early applications of X-ray tomography were mainly used in medical imaging; for example, to image bone structure or diagnose disease [155]. With its capability of imaging 3D structures in a non-invasive way, it is now widely used in other areas, such as geological and material sciences [154-157] and is fast becoming a conventional characterisation technique [158]. In academic research, the X-ray tomography imaging technique has recently been employed successfully to reconstruct 3D binary images of PEMFC GDLs [19, 30, 31, 60, 69, 103-110, 159] in order to characterise material properties and investigate fluid flows in reconstructed GDL structures. With X-ray tomography, the sample preparation is usually minimal and, as it is non-destructive, the same sample can be scanned repeatedly under different conditions [156].

3.2 Principles of X-ray Computed Tomography

A typical X-ray computed tomography system consists of an X-ray source, a sample holder and an X-ray detector, as illustrated in Fig. 3.1. In the early X-ray systems, the X-ray source rotated simultaneously with the detector in order to obtain 2D projections. Most modern desktop X-ray scanners, however, are now based on the rotation of the scanned sample [154]. The projections of the sample are obtained by rotating it in front of the trajectory of an X-ray beam. Part of the X-rays is absorbed by the sample, whereas the transmitted X-rays are collected by the detector. The detector system is often a scintillator screen, which converts the transmitted X-rays into visible light, coupled with a CCD or CMOS detector that captures light which corresponds to a projection of the scanned sample [154, 158]. The greyscale projections obtained by the detector are then used to make 2D cross-section image slices, which correspond to what would be seen if the

sample was cut through the scanning plane [19]. The 2D cross-sectional slices are then assembled to make a 3D image of the sample.

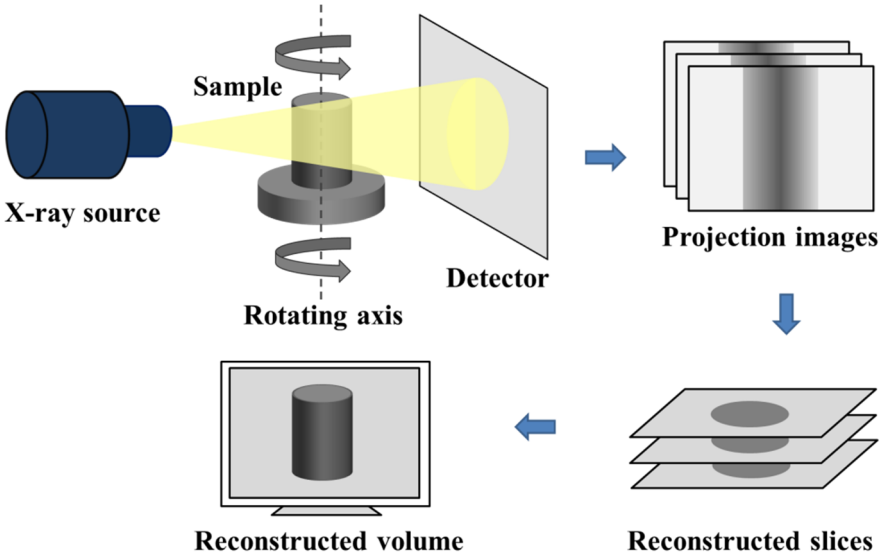

Figure 3.1 Illustration of a typical X-ray computed tomography process, including image acquisition and image reconstruction. Adapted after [156].

The X-ray computed tomography process typically involves image acquisition, image reconstruction and image thresholding, all of which are described in the following sections.

3.2.1 Image Acquisition

The principles of a desktop X-ray CT scanner are illustrated in Fig. 3.1. A sample is positioned in front of the X-ray source and rotated step-by-step along its vertical axis. At each rotating step, a greyscale projection is produced using an X-ray detector array. A series of greyscale projections, therefore, are obtained from different rotation angles from 0° to 360° for one scan. The General Electric Phoenix nanotom® system used in this study is equipped with an X-ray source of 160kV (max) and 250μA (max) with an X-ray spot size of approximately 1μm. The three most important properties of the X-ray source

are voltage, current and spot size [160]. High voltage allows the imaging of a thicker or denser sample; however, high voltage can cause X-ray over-transmission and the projection images can become over-bright [160]. High current involves a more intensive X-ray beam resulting in a shorter exposure time and better image contrast therefore, high current is usually preferred. As far as spot size is concerned, a smaller spot size results in lesser penumbral blurring, which can produce a sharper projection [156, 160]. The values of voltage and current are set for optimal visualisation and contrast.

For the X-ray detector, the two most important parameters are pixel size and the number of pixels, as with a small pixel size and larger numbers of pixels more details can be captured [160]. The General Electric Phoenix nanotom® system employed in this study, used a 5-megapixel flat panel CMOS (complementary metal-oxide semiconductor) detector with a GOS (gadolinium oxysulfide) scintillator deposited on a fibre optic plate. In an X-ray detector, the X-rays are converted to visible light by a GOS scintillator, which is then recorded by a flat panel CMOS detector to produce the projection images. The quality of the X-ray image is greatly dependent on the quality of the X-ray source and the detector, as well as the precision and stability of the manipulation device [161].

3.2.2 Image Reconstruction

A common method for image reconstruction is to reconstruct a set of 2D greyscale projections obtained from the X-ray detector into 2D cross-sectional image slices and then to stack them into a 3D volume, as illustrated in Fig. 3.1. In this method, the reconstruction is usually based on the back-projection method in which at each rotation step the lines of possible positions of a point are added to the reconstructed area. With several rotation steps, the position of the absorption point in the reconstructed area can be localised. With the increasing number of projections borne out of the increasing rotation steps, localisation becomes more precise [162-164]. With the back-projection method, 2D greyscale cross-sectional image slices of the scanned sample, which correspond to what would be seen if the sample was cut through the scanning plane, are generated. A series of 2D cross-sections are then assembled to form a 3D reconstructed volume of the scanned sample.

Another method is where the projections are directly reconstructed into a 3D volume using a filtered back-projection algorithm. The nanotom® CT software, namely the Phoenix datos|x CT software, uses a proprietary implementation based on Feldkamps cone beam reconstruction algorithms to reconstruct the 3D volume of the scanned sample [165, 166]. This software allows the image acquisition and reconstruction to be fully automated.

In order to characterise material properties and simulate fluid flows through the material, an accurate representative binary 3D model is required. Therefore, it is necessary to threshold the greyscale image slices or the greyscale volume obtained from the X-ray tomography to produce binary images for characterisation and simulation.

3.2.3 Image Thresholding

In order to distinguish solids from pores, the threshold process is required. The threshold value is often determined by visual inspection or by the Otsu algorithm [167]. The Otsu algorithm, a clustering-based thresholding method, determines the optimum threshold value at which the sum of foreground and background spreads is at a minimum [168]. The Otsu method, however, cannot always be reliable while it is also computationally expensive when dealing with a large set of images [168].

Conversely, Ostadi et al. [159] proposed a heuristic technique in which the threshold level was determined by comparing the average diameter and fibre connectivity of the surface of the X-ray reconstructed 3D image with those of a reference scanning electron microscopy (SEM) image [159]. They found that this method is relatively fast and more reliable than the common visual threshold tuning without any prior knowledge of the micro structure [159]. This threshold technique was then employed in several studies [19, 30, 31, 60, 69, 103-110, 159].

In this thesis, the threshold technique proposed by Ostadi et al. [159] was utilised to create 3D binary images of the GDL samples, which were then used for structure and transport analysis, as well as fluid flow simulations. The 2D and 3D thresholded reconstructed binary images of a GDL sample are illustrated in Fig. 3.2.

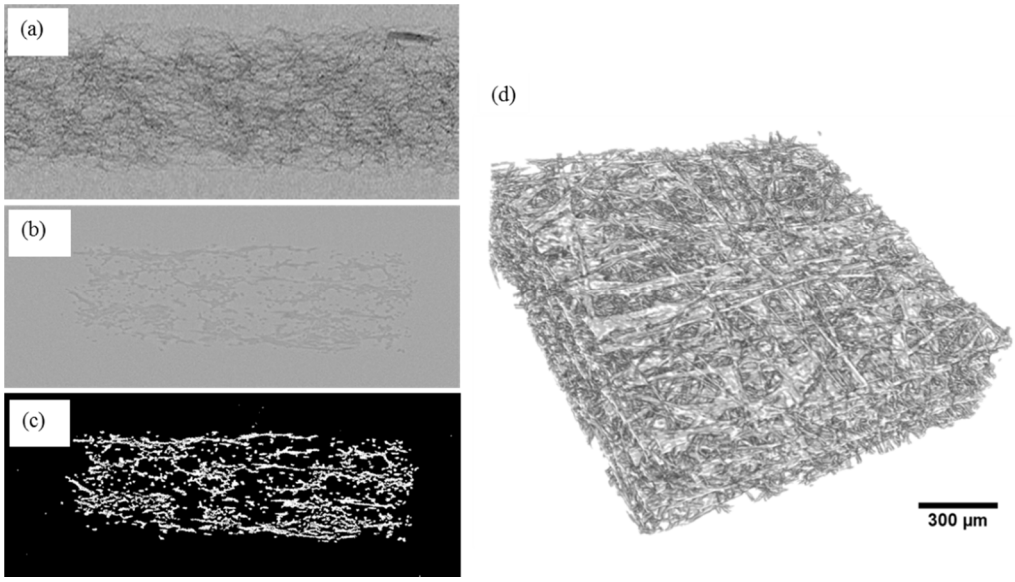

Figure 3.2 2D and 3D images of a carbon paper GDL sample: (a) a shadow X-ray tomography image (b) a 2D reconstructed greyscale cross-sectional image slice (c) a binary cross-sectional image slice after threshold (d) the 3D binary reconstructed image.

3.3 Conclusions

In this chapter, the basic principles of X-ray computed tomography, including image acquisition, image reconstruction and image thresholding were described. In Chapter 4, X-ray reconstructed images of a carbon paper GDL at various image resolutions are incorporated into a single-phase Lattice Boltzmann (LB) solver in order to examine the effect of image resolutions on gas permeability. In Chapter 5, the X-ray tomography technique is employed to generate the 3D digital structures of carbon paper and carbon felt GDL samples. The reconstructed images are then used to characterise the structure and transport properties, including thickness, porosity, tortuosity and permeability, for each GDL sample. In Chapter 7, the X-ray reconstructed images are integrated into the two-phase LB solver in order to simulate liquid water transport behaviours in the GDL structures under different conditions.

Chapter 4
Sensitivity Analysis on Image Resolution

4.1 Introduction

The gas diffusion layer (GDL) plays an important role in the overall performance and durability of a PEMFC by serving several functions, including providing pathways for reactant gases to access the reaction sites; removing product water; transporting heat and electrons; while also serving as a mechanical support for the membrane [15]. The GDL is a heterogeneous porous carbon-based material typically made of carbon paper, carbon felt and carbon cloth with thickness in the range of 100-300 μm [3]. The individual carbon strands are around 7-12 μm in diameter and the bundle diameters in the woven materials can be in the region of 400 μm [15, 18].

To date, experimental measurements of fluid flows and associated parameters in the diminutive structure of the GDL remain difficult. Therefore, numerical models have been extensively developed and applied to examine fluid transport through the GDL. The Lattice Boltzmann (LB) method has been increasingly utilised to investigate fluid transport behaviours in GDL and general porous material due to its capability to incorporate complex boundaries of actual GDL structures into the model. A number of studies have been conducted using the LB method to examine complex flows through carbon paper and carbon cloth GDL structures at pore-scale [67, 68, 102]. Hao and Cheng [67] studied the anisotropic permeability of a carbon paper GDL using the LB model. Similar work was also conducted by Van Doormaal and Pharoah [102] to determine the permeability of an idealized GDL. Van Doormaal and Pharoah [102] concluded that the permeability in both through-plane and in-plane directions depends strongly on the porosity of the sample. They also reported that the through-plane permeability was not affected much by fibre angle in contrast to the in-plane permeability, which was greatly affected by fibre angle. These works incorporated either 2D or 3D artificial structures generated by stochastic simulation techniques to the LB models. The stochastic approach is relatively more rapid and less expensive than generating the GDL model through experimental imaging techniques, such as X-ray tomography. The stochastic-based

model, however, does not represent closely microscopic features of the actual GDL as manufactured. Several assumptions are required for the stochastic method. For example, fibres are considered to be cylindrical with a uniform diameter and are infinitely long [4]. In addition, the binding materials are often ignored in stochastic models, which can result in the model being more unrealistic.

In order to reflect the actual GDL structure accurately, the X-ray computed tomography reconstruction technique has been used to generate 3D representative structures of GDL samples. X-ray tomography is a non-invasive and non-destructive imaging technique which allows the 3D visualisation of an internal structure of a scanned sample [154]. The combination of the two advanced techniques of the X-ray tomography and the LB method has also been successfully applied to study fluid movement through PEMFC GDLs in recent studies by Rama et al. and Ostadi et al. [19, 30, 31, 60, 69, 103-110] in both single-phase and two-phase flows to predict air permeability, anisotropic permeability, tortuosity and water behaviours. The high computational demand of the LB method, however, together with the commonly used highest available resolution of the X-ray images has limited its application to analyse only a very small volume of the GDL. With high resolutions, the LB flow simulation is also extremely time-consuming. Recently, Hao and Cheng [29] examined the pixel size effect on a stochastic reconstructed GDL with resolutions of 1.5 μm, 2.5 μm and 3.8 μm respectively, by performing drainage simulations. The results showed almost the same capillary pressure curves for the 1.5 μm and 2.5 μm and thus the 2.5 μm was employed in that study. In Hao and Cheng [29], however, the GDL was reconstructed based on the stochastic model, which could not fully replicate the actual GDL structure.

This work aimed to examine the effect of image resolution on gas permeability through the X-ray reconstructed GDL by using the LB method. The binary 3D models of the GDL at 6 different resolutions were acquired by using the X-ray imaging technique. Each image was then integrated into a single-phase LB numerical solver to characterise its gas permeability. The resulting permeability, its sensitivity to the resolution variation and the computational time were analysed in order to identify the optimum resolution for the representative model of the GDL.

4.2 Single-Phase Lattice Boltzmann Modelling

In this study, the three-dimensional single relaxation time LB model was used to simulate gas flow through the GDL. Principally, the LB method tracks the movements and collisions of a number of fictitious fluid particles in a lattice domain. The movement of each fictitious particle is described by the particle distribution function $f_i(x,t)$ which defines the mass of a particle at location *x* and time *t* moving with the velocity ξ_i along the direction *i*

$$f_i\left(x+\xi_i\delta t, t+\delta t\right) = f_i\left(x,t\right) + \frac{1}{\tau}\left[f_i^{eq}\left(x,t\right) - f_i\left(x,t\right)\right] \tag{4.1}$$

where $f_i^{eq}\left(x,t\right)$ is the equilibrium distribution function and τ is the dimensionless relaxation parameter that controls the rate at which $f_i\left(x,t\right)$ approaches $f_i^{eq}\left(x,t\right)$. The equilibrium distribution function $f_i^{eq}\left(x,t\right)$ is given by:

$$f_i^{eq}\left(x,t\right) = w_i\rho\left[1 + \frac{\xi_i \cdot u}{c_s^2} + \frac{1}{2}\left(\frac{\xi_i \cdot u}{c_s^2}\right)^2 - \frac{u \cdot u}{2c_s^2}\right] \tag{4.2}$$

where w_i is a weighting factor depending on the magnitude of the velocity ξ_i and c_s is the speed of sound. The bulk fluid density ρ and velocity u are obtained by summing the corresponding distribution functions of all incoming particles at each node in the lattice domain as follows:

$$\rho = \sum_i f_i \tag{4.3}$$

$$\rho u = \sum_i f_i \xi_i \tag{4.4}$$

The three-dimensional LB scheme, containing 19 velocities (commonly referred to as D3Q19), was employed in this work, whereby fluid particles in each lattice node are able to move in 19 directions from the origin in the three-dimensional regime as shown in Fig. 2.2.

The LB implementation involves a collision step and a streaming step. In a collision step, the term on the right-hand side of Eq. (4.1) is calculated as $f_i^*(x,t) = f_i(x,t) + \left[f_i^{eq}(\rho,u) - f_i(x,t)\right]/\tau$. The streaming step moves the outcomes of collisions $f_i^*(x,t)$ from location x to the nearest location $x + \delta t \xi_i$ along their direction of motion at time $t + \delta t$ to become $f_i(x + \delta t \xi_i, t + \delta t) = f_i^*(x,t)$. After the streaming step has been completed, the gas density ρ and velocity u for each node in the lattice domain are then updated through $\rho(x,t+\delta t) = \sum_i f(x,t+\delta t)$ and $\rho u = \sum_i f_i(x,t+\delta t)\,\xi_i$ respectively [19].

In the LB model, the bounce-back scheme for no-slip boundaries is used to solve fluid-solid boundary conditions by assuming that any fluid particle that hits a solid boundary during the streaming step is simply bounced back to its original location at the end of each time step. In order to drive gas flow, a pressure difference is applied to two opposite sides of the domain in one direction, while the other four sides are treated as periodic boundaries where the particles exiting the domain from one side re-enter through its opposite side [19].

4.3 Permeability Calculation

Permeability is a key transport property of a porous medium which describes the ability of the material to allow fluids to pass through it. The permeability of a material depends only on its porous structure. The detailed gas velocity distribution in the void space of the GDL domain at the microscopic scale obtained from the LB simulation is used to calculate the absolute permeability at the macroscopic scale. The absolute permeability of the GDL k is defined by Darcy's law as:

$$k = \frac{\rho \nu\, q}{(\Delta P / L)} \tag{4.5}$$

where ρ is the gas density, q is the average gas velocity through the GDL in the direction of the pressure gradient, ΔP is the applied pressure gradient across the GDL domain, L is

the size of the domain and ν is the kinematic viscosity, which is related to the dimensionless relaxation time as:

$$\nu = \delta x^2 (\tau - 1/2)/3\delta t \tag{4.6}$$

By applying a pressure difference in the through-plane direction (z-direction), gas can also flow in the in-plane direction (y- and x- directions). The three components of the permeability tensor in principal and off-principal flow directions can be calculated as:

$$k_{zz} = \frac{\rho\nu\, q_z}{(\Delta P / L_z)};\ k_{yz} = \frac{\rho\nu\, q_y}{(\Delta P / L_z)};\ k_{xz} = \frac{\rho\nu\, q_x}{(\Delta P / L_z)} \tag{4.7}$$

where q_x, q_y, q_z are the average velocities and L_x, L_y, L_z are the sizes of the domain in x-, y- and z-directions respectively. The average velocities in the three directions are:

$$q_x = \frac{\sum_i u_x(x_i)}{L_x L_y L_z};\ q_y = \frac{\sum_i u_y(x_i)}{L_x L_y L_z};\ q_z = \frac{\sum_i u_z(x_i)}{L_x L_y L_z} \tag{4.8}$$

4.4 Digital 3D Models using X-ray Computed Tomography

In this study, the digital image of a carbon paper GDL sample was originally generated at the resolution of 0.68 μm/pixel through the X-ray computed tomography imaging technique. There were three key steps involved in generating the 3D images, including progressive 2D imaging using X-ray tomography, image processing and digital 3D reconstruction. The complete details of image acquisition and reconstruction of the GDL were reported in Chapter 3 and in [19].

In order to examine the pixel size effect on the absolute permeability, a number of 3D images were further generated based on the original resolution by increasing the pixel size, starting with 2 times up to 6 times larger than the base pixel size. Therefore, the GDL images at the resolutions of 0.68, 1.36, 2.04, 2.72, 3.40 and 4.08 μm/pixel respectively were employed to study the impact on the resulting permeability. Examples of binary image slices generated with these resolutions are shown in Fig. 4.1. Fig. 4.2

compared with the 3D and 2D images of the reconstructed GDL samples at these 6 resolutions.

Due to the limitations of computational power, each GDL image with the original size of about 211 μm × 204 μm × 224 μm was equally split into 4 small regions, as illustrated in Fig. 4.3 and Fig. 4.4. The size of each region in voxels and physical dimensions for each resolution are shown in Table 4.1. The 3D images at the 6 different resolutions of region 1 to region 4 are shown in Fig. 4.5 – Fig. 4.8.

Table 4.1 Digital and physical size for each GDL region at the resolution of 0.68, 1.36, 2.04, 2.72, 3.40 and 4.08 μm/pixel respectively.

Resolutions	**Image size in voxels**			**Image size in μm**		
(μm/pixel)	**x**	**y**	**z**	**x**	**y**	**z**
0.68	155	150	329	105.40	102.00	223.72
1.36	78	75	164	106.08	102.00	223.04
2.04	52	50	109	106.08	102.00	222.36
2.72	39	38	82	106.08	103.36	223.04
3.40	31	30	65	105.40	102.00	221.00
4.08	26	25	54	106.08	102.00	220.32

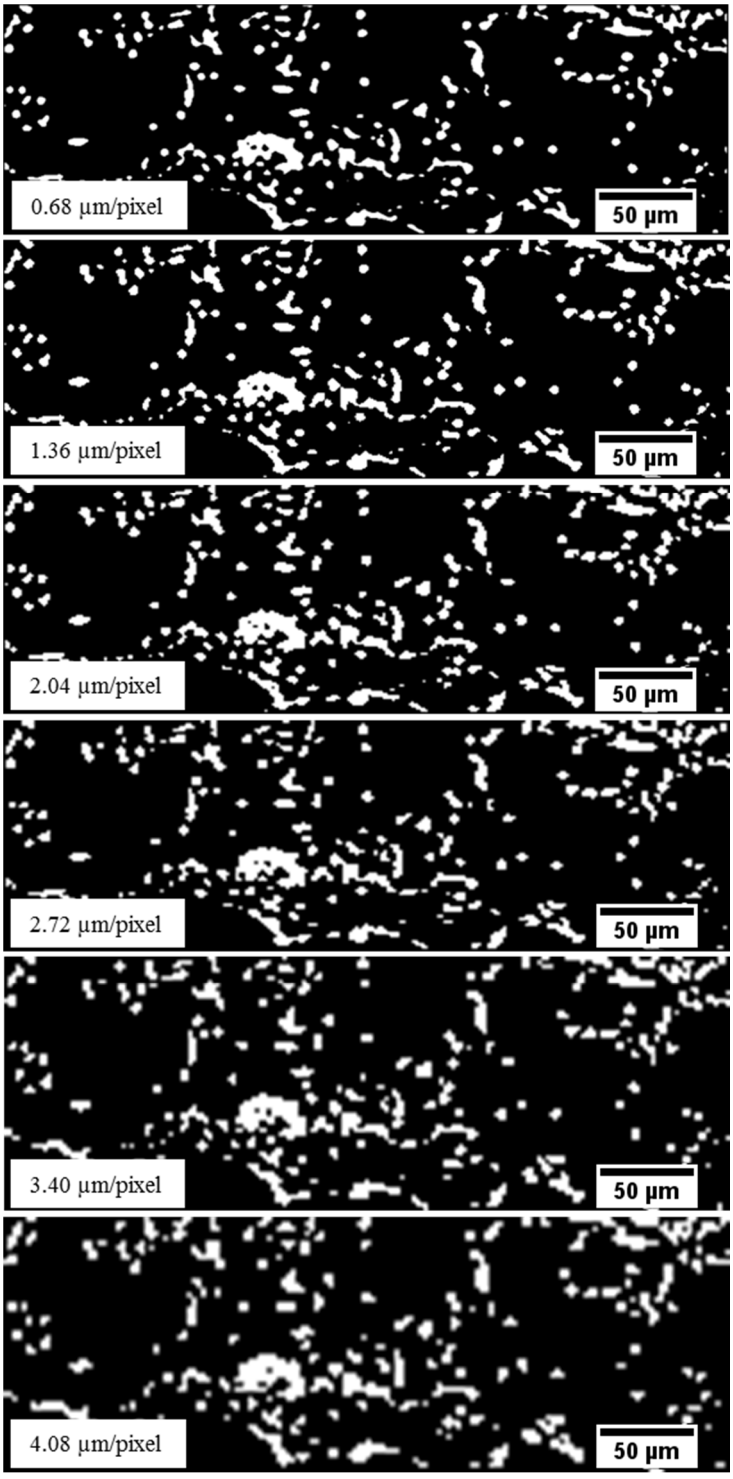

Figure 4.1 Binary slices generated with the resolutions of 0.68, 1.36, 2.04, 2.72, 3.40 and 4.08 µm/pixel respectively.

(a)

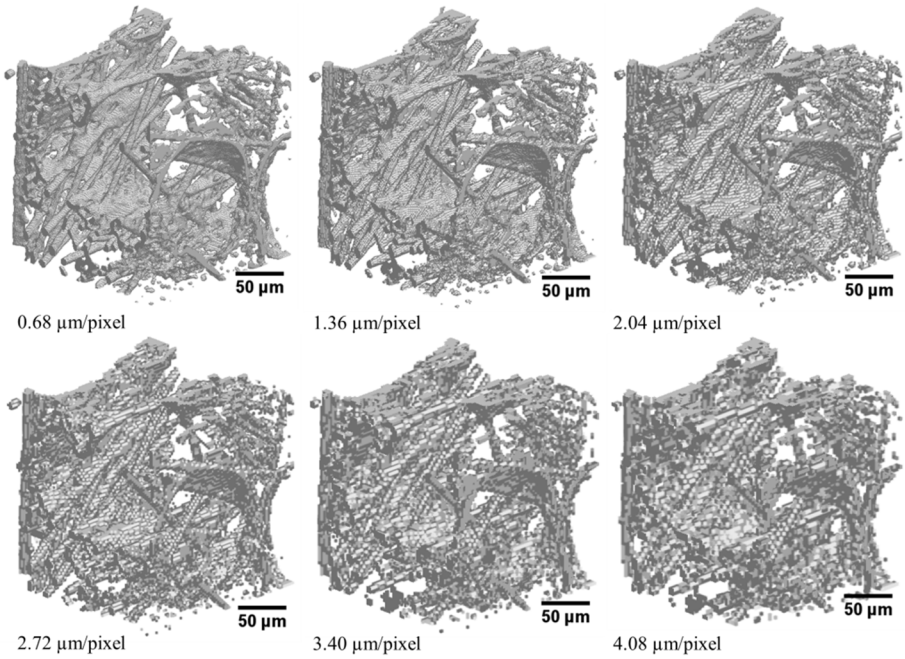

(b)

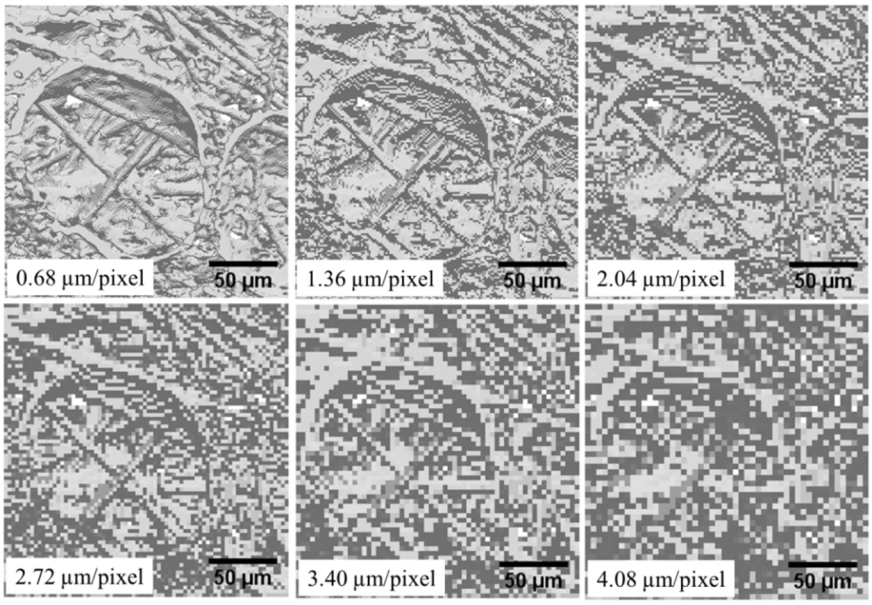

Figure 4.2 (a) 3D and (b) 2D images of the X-ray reconstructed GDL sample at the resolutions of 0.68, 1.36, 2.04, 2.72, 3.40 and 4.08 µm/pixel respectively.

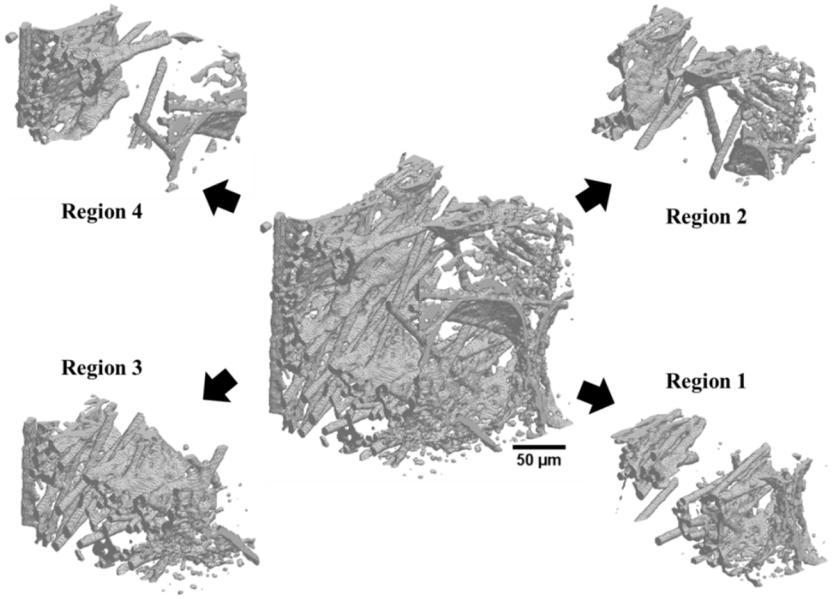

Figure 4.3 Domain division of the GDL sample into 4 small regions at the resolution of 0.68 µm/pixel.

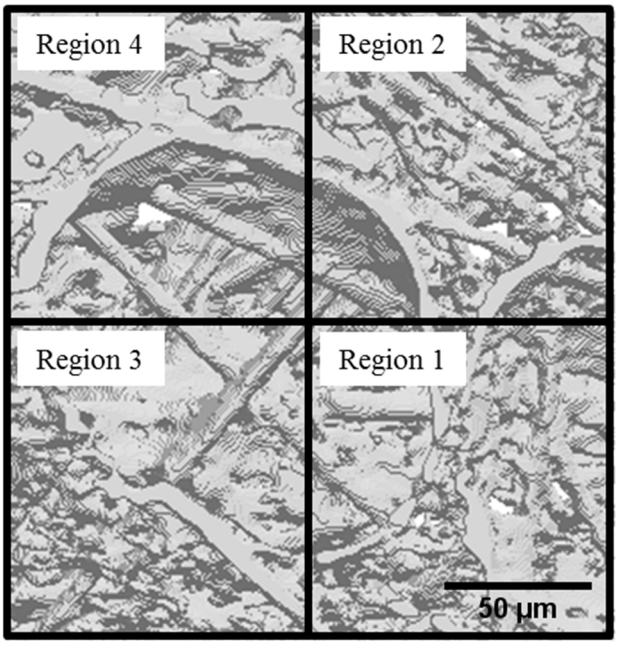

Figure 4.4 Surface view of the 4 split domains of the GDL sample at the resolution of 0.68 µm/pixel.

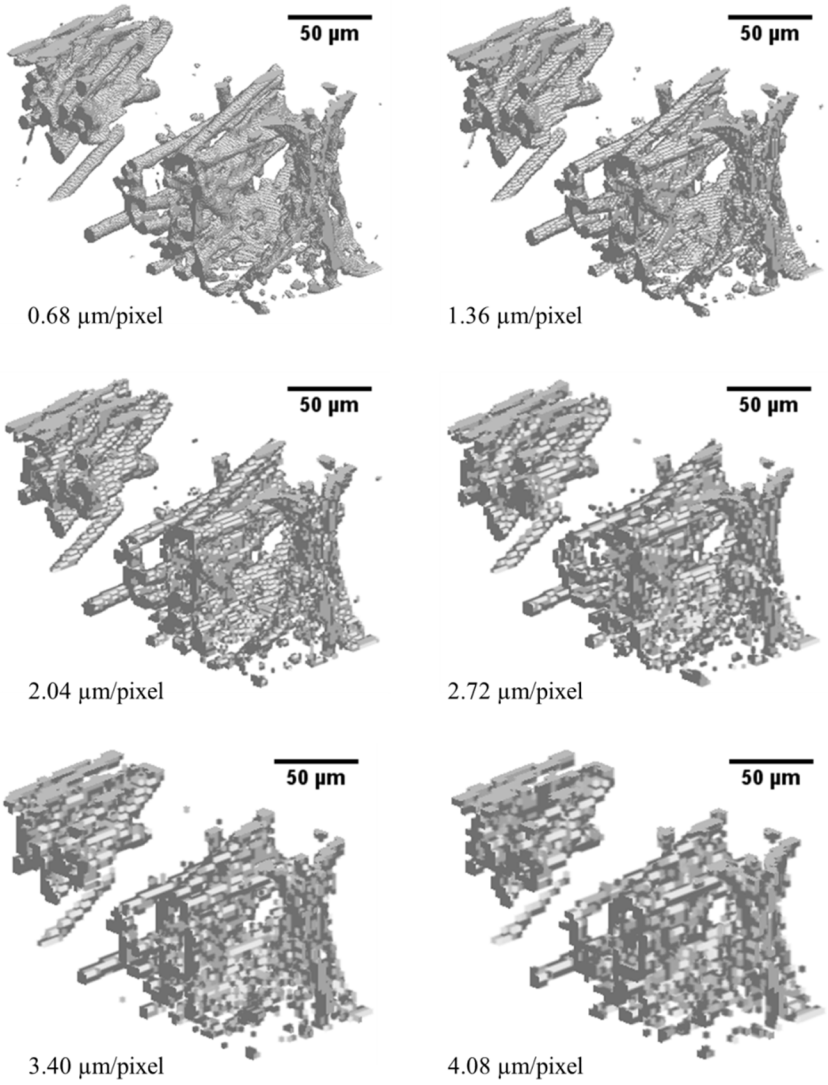

Figure 4.5 3D models of region 1 reconstructed at the resolutions of 0.68, 1.36, 2.04, 2.72, 3.40 and 4.08 µm/pixel respectively.

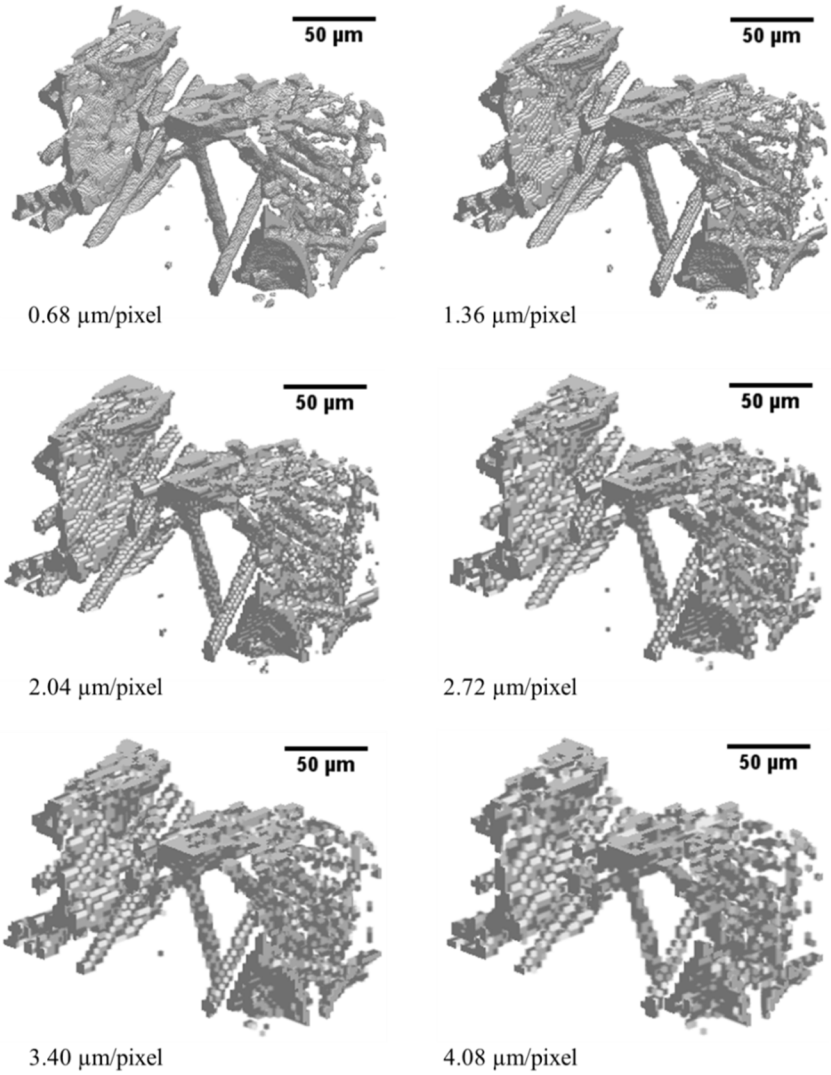

Figure 4.6 3D models of region 2 reconstructed at the resolutions of 0.68, 1.36, 2.04, 2.72, 3.40 and 4.08 µm/pixel respectively.

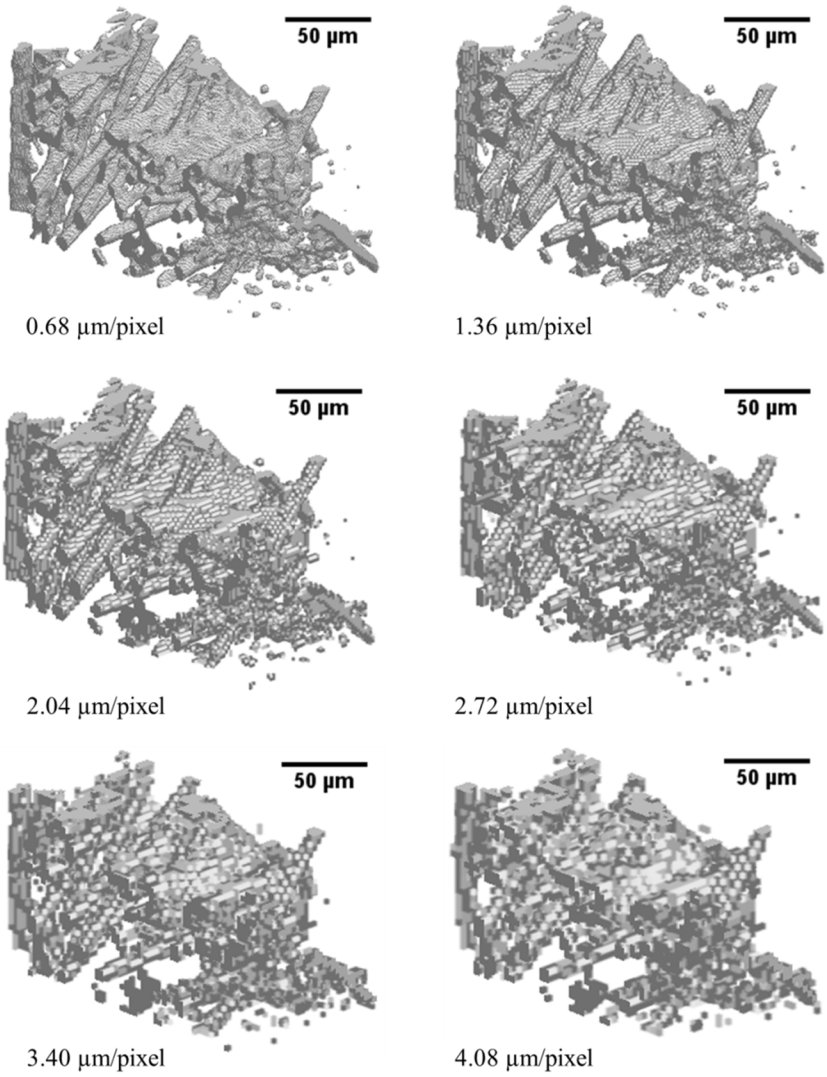

Figure 4.7 3D models of region 3 reconstructed at the resolutions of 0.68, 1.36, 2.04, 2.72, 3.40 and 4.08 µm/pixel respectively.

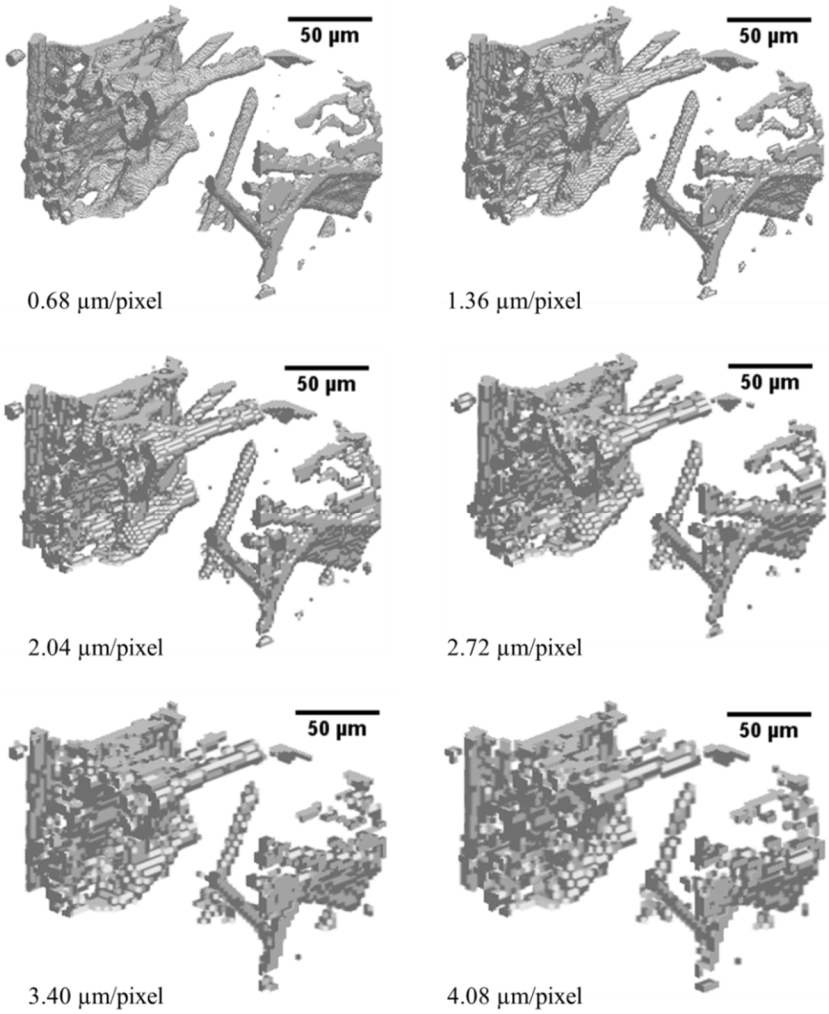

Figure 4.8 3D models of region 4 reconstructed at the resolutions of 0.68, 1.36, 2.04, 2.72, 3.40 and 4.08 µm/pixel respectively.

4.5 Results and Discussion

The single-phase LB model with the D3Q19 scheme was applied to each of the 4 regions of the GDL images reconstructed with the 6 different resolutions including 0.68, 1.36, 2.04, 2.72, 3.40 and 4.08 μm/pixel. In order to simulate gas flow through the GDL, the pressure difference of 10 Pa was applied to each region and the entire void space was assumed to be filled with air. The principal flow direction was set in the through-plane direction along the GDL thickness. The detailed gas velocity field obtained from the LB simulation was then used to predict the gas permeability through the simulated GDL domain by using Darcy's law. The spatial resolution of the LB model was set as equal to the pixel resolution of the reconstructed images. All simulations were carried out on a quad-core 2.33 GHz workstation with 3.25 GB RAM.

Fig. 4.9 (a)-(c) illustrate the simulated permeability in the principal through-plane flow direction (z-direction) and the off-principle in-plane flow directions (y- and x-directions) when the pressure gradient was applied in the through-plane direction. Fig. 4.9 (a)-(c) show that the gas permeability in all flow directions varies locally among each simulated region exhibiting the heterogeneous nature of the GDL. In order to compare the effect of varying resolutions, therefore, at each resolution the means were chosen as the representative values for all 4 regions. The mean simulated values of the gas permeability both in principal through-plane and off-principal in-plane flow directions, and the average calculation time for each resolution are shown in Table 4.2.

The results show that the variation of the image resolution contributes to a significant difference in the resulting permeability in all flow directions. Assuming that the GDL image reconstructed from the base resolution of 0.68 μm provides the most accurate set of permeability values, all sets of results over the whole range of resolutions show that the differences are up to 30%, 32% and 26% for the resulting through-plane permeability and in-plane permeability in y- and x-directions respectively, as illustrated in Fig 4.10. The permeability values for the 3.40 μm and 4.08 μm resolutions show the greatest deviation from that of the base resolution. The lowest resolution of 4.08 μm produces the largest difference in the resulting permeability from that of the base resolution in both through-plane z and in-plane x directions, whilst the 3.40 μm resolution

displays the greatest increase in permeability in the y-direction. This agrees with the visual inspection in which these two coarse images clearly lose their image quality compared to the images of the other four resolutions. Conversely, these two coarsest resolutions lead to a massive reduction in terms of computational time, from approximately 1620 minutes per region at the original resolution to just about 1 minute, as shown in Table 4.2.

Figure 4.10 also illustrates that the 1.36 μm image resolution produces the smallest difference of 7.1% from the original resolution for the through-plane permeability. The image resolutions of 2.04 and 2.72 μm, however, offer the smallest difference in resulting permeability with only 2.8% and 0.3% difference for the in-plane y- and x-directions respectively, while the differences are more than 13% and 8% respectively for the case of 1.36 μm resolution.

The results also indicate that the GDL image at the resolution of 2.72 μm provides the best compromise between accuracy and computational time. The resulting permeability values show a less than 8%, 5% and 0.3% difference for the principle through-plane direction and off-principle in-plane in y- and x-directions respectively, while computational time reduces greatly to just 4 minutes, which is approximately 400 times less than the base resolution. By utilising the 2.72 μm resolution, simulations are also able to analyse the gas flow characteristics in a 64 times larger domain.

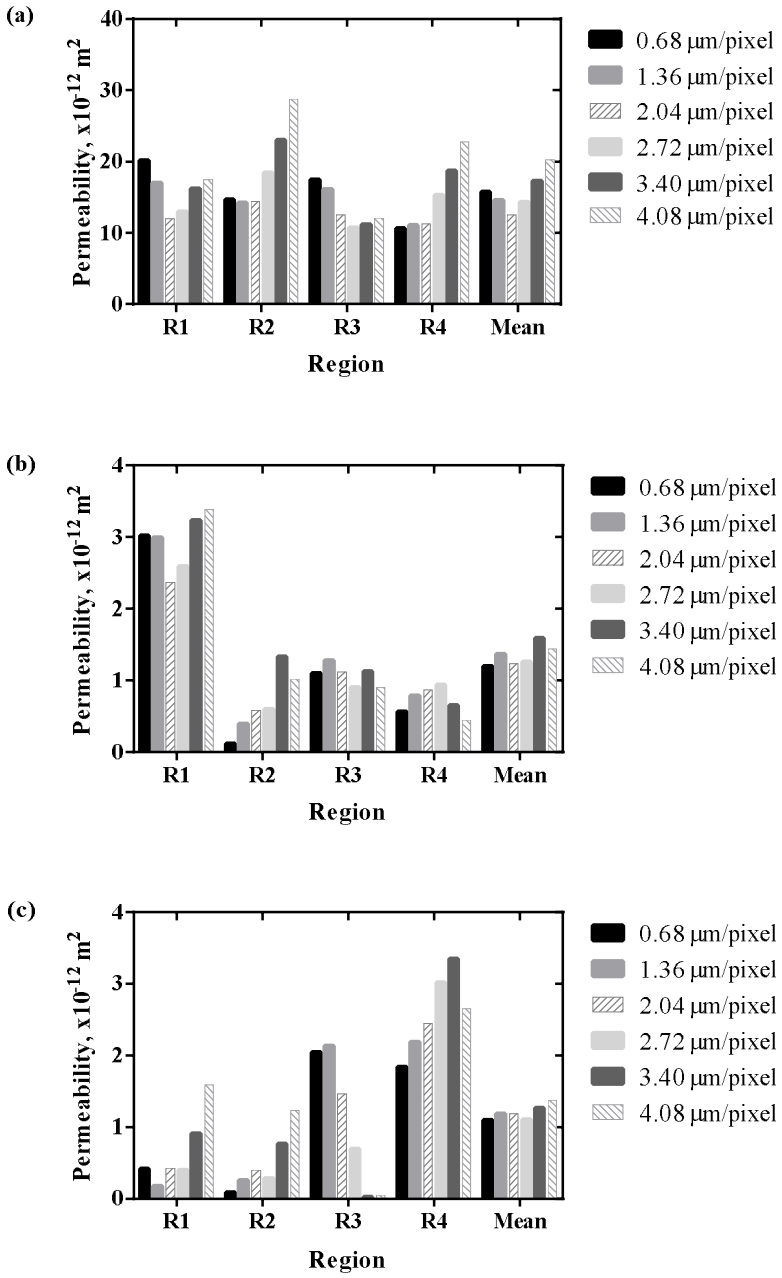

Figure 4.9 Simulated absolute permeability in (a) through-plane direction (z-direction); (b) in-plane y-direction; (c) in-plane x-direction, for the 4 regions with 6 different resolutions including mean values.

Table 4.2 Mean simulated through-plane permeability, in-plane permeability in y- and x-directions, and mean calculation time in each region of the reconstructed GDL sample at the resolutions of 0.68, 1.36, 2.04, 2.72, 3.40 and 4.08 μm/pixel respectively.

Resolutions (μm/pixel)	Mean through-plane permeability ($\times 10^{-12}$ m^2)	Mean in-plane permeability y-direction ($\times 10^{-12}$ m^2)	Mean in-plane permeability x-direction ($\times 10^{-12}$ m^2)	Mean calculation time (min)
0.68	15.7332	1.2022	1.0981	1620
1.36	14.6168	1.3642	1.1893	63
2.04	12.5515	1.2353	1.1845	10
2.72	14.3591	1.2612	1.1006	4
3.40	17.2916	1.5874	1.2636	1
4.08	20.2754	1.4397	1.3783	<1

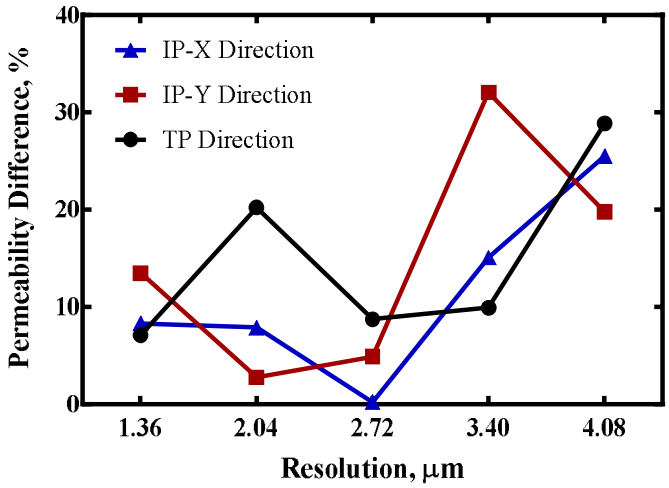

Figure 4.10 Percentage difference in the mean permeability in the through-plane (TP) direction and in-plane in x- (IP-x) and y- (IP-y) directions of the GDL images at resolutions of interest, compared with the 0.68 μm resolution image.

4.6 Conclusions

This study was conducted using the LB method and the X-ray computed tomography technique. The 3D models of the GDL at 6 different resolutions were generated via the X-ray reconstruction technique. Each of the images was then incorporated into the LB solver to predict its permeability. The effect of image resolution on gas permeability through the representative models of the actual GDL was studied. It was found that the resolution variation has a great impact on the resulting permeability in all flow directions. The coarser resolutions contribute to a change in resulting permeability of about 30% and 32% for principal and off-principal flow directions respectively. Conversely, the average computational time reduces greatly from 27 hours for fine resolution to less than one minute for the coarse images. The results suggest that the GDL image at the resolution of 2.72 μm, a 4 times larger than the original resolution, provides the best compromise between permeability values and computational time. It shows only 8% difference in permeability and took 400 times less in computational time when compared to the base 0.68 μm/pixel resolution. In addition, with this resolution it is possible to investigate gas flows in a 64 times larger domain. In conclusion, it is worth considering the effect of image resolution to identify the optimum resolution for the representative GDL model, which potentially improves computational efficiency in terms of computational time, resulting in substantially lower computational costs or even allowing simulations in a larger GDL volume whilst maintaining satisfactory accuracy.

Chapter 5
Characterisation of Heterogeneous Through-Plane Distributions of Porosity, Permeability and Tortuosity in Gas Diffusion Layers

5.1 Introduction

A GDL is a porous medium commonly made of carbon paper, carbon felt or carbon cloth. Carbon paper and carbon felt consist of randomly dispersed carbon fibres, whilst carbon cloth consists of woven bundles of carbon fibres [19]. The GDL allows reactant gases to be transported from gas channels to CLs where electrochemical reactions take place. The transport of reactant gases through the GDL, by both diffusion and convection, is dependent upon its material properties [17, 61]. Porosity, which is one of them, has a direct influence on the effective diffusion coefficient [47], tortuosity and permeability [61] and, thus, the gas and water transport through the GDL [17]. In addition, porosity significantly affects the uniformity of the distributions of the reactant gases to the CLs [169]. The two common methods to determine the porosity of the GDL are mercury intrusion porosimetry (MIP) and immersion. The MIP method evaluates the total pore volume by measuring the amount of mercury that has penetrated into the pores of a porous medium as a function of applied pressure. The immersion method, on the other hand, determines the porosity by weighing the sample before and after its immersion in a wetting fluid [47]. Recently, the advancement of imaging technology, such as X-ray tomography, allows for direct porosity measurement without the requirement of an intruding fluid. Ostadi et al. [106] determined the porosity of a GDL based directly on X-ray binary images. In each binary image, 0 and 1 represent a void and solid voxel of the reconstructed GDL respectively. The ratio between the number of void voxels and the number of total voxels in the entire GDL volume was obtained as porosity. Unlike Ostadi et al. [106], who reported porosity as a uniform value, Fishman et al. [56] reported the heterogeneous porosity distribution across the GDL thickness by employing X-ray tomography images. They also showed different porosity distributions for different types of GDL samples. With the tomography images, Fishman and Bazylak [170] also

examined the effect of PTFE and binding agents on porosity distribution. They concluded that PTFE and binding agents accumulate in low porosity areas, where the density of fibres is higher. In another work, Fishman and Bazylak [171] utilised analytical models available in the literature to predict the tortuosity and permeability distributions of the GDL samples based on the porosity distribution obtained in [56]. Kim and Lee [172] studied the effect of the freeze-and-thaw of liquid water in GDLs by comparing porosity distribution before and after freeze-and-thaw. They demonstrated the irreversible structure transformation through the decrease of porosity after freeze-and-thaw cycles. The variation of tortuosity and permeability after freeze-and-thaw cycles was also estimated based on porosity distribution. These studies provide insight into the heterogeneous porosity distribution of the GDL structures under normal and critical conditions, and how this affects transport properties through the use of the analytical model proposed by Tomadakis and Sotirchos (referred to as the TS model) [173, 174]. The TS model was originally developed for randomly oriented fibrous porous media, which allow the prediction of anisotropic permeability and tortuosity through one-dimensional, two-dimensional and three-dimensional random fibre beds in a convenient way without using any fitting parameters [62]. The TS model has been widely used to estimate permeability and tortuosity in fibrous materials and the results for the GDLs have been validated numerically and experimentally by several researchers including Nam and Kaviany [48] and Gostick et al. [62], who reported close agreement with their numerical and experimental results.

This study aimed to characterise the through-plane distributions of porosity, permeability and tortuosity of the newly reconstructed models of the GDL samples with paper and felt structure. The 3D digital volumetric models of the GDL samples were generated through the X-ray tomography (XCT) technique. The tomography image slices of each sample were then used to characterise the GDL properties, which include thickness, porosity, permeability and tortuosity. The thickness and local through-plane porosity distributions of each GDL were examined based on the tomography images. The resulting through-plane porosity distributions were then used to predict through-plane permeability and tortuosity distributions based on the TS model.

5.2 Materials and Methods

5.2.1 Materials

The GDL samples used in this study included Toray TGP-H-120 paper, SGL 24AA paper and Freudenberg H2315 felt GDLs. These are uncompressed GDL materials with no additional PTFE and MPL. The Toray TGP-H-120 and SGL 24AA have a paper structure composed of strands of carbon which are layered and compressed together. The strands of the paper-type are linear and mainly travel in the in-plane direction. As a result, a carbon matrix is required to hold the carbon strands together. The carbon matrix is usually referred to as a binder or carbonised binder. The Freudenberg H2315, on the other hand, has a felt microstructure in which the fibres are non-linear and pushed through the thickness direction. It requires no binder as its carbon strands travel in both the in-plane and through-plane direction, which hold the structure together. Throughout this chapter, GDLs are referred to as Toray, SGL and Freudenberg respectively. Fig. 5.1 – Fig. 5.3 show scanning electron microscopy (SEM) images of these GDL samples.

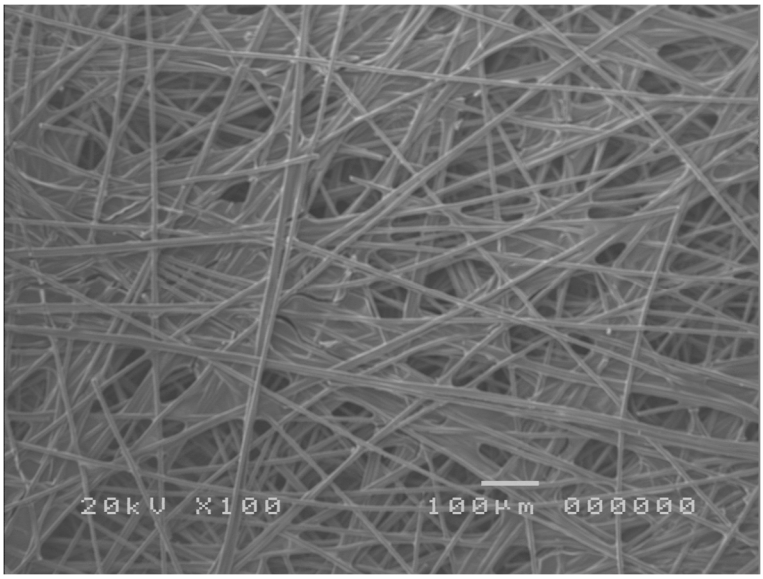

Figure 5.1 SEM micrograph of Toray TGP-H-120 paper GDL sample

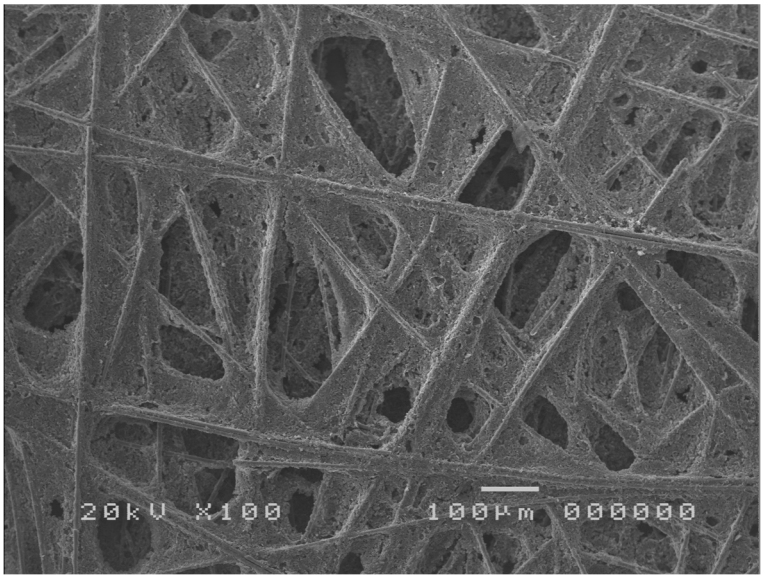

Figure 5.2 SEM micrograph of SGL 24AA paper GDL sample.

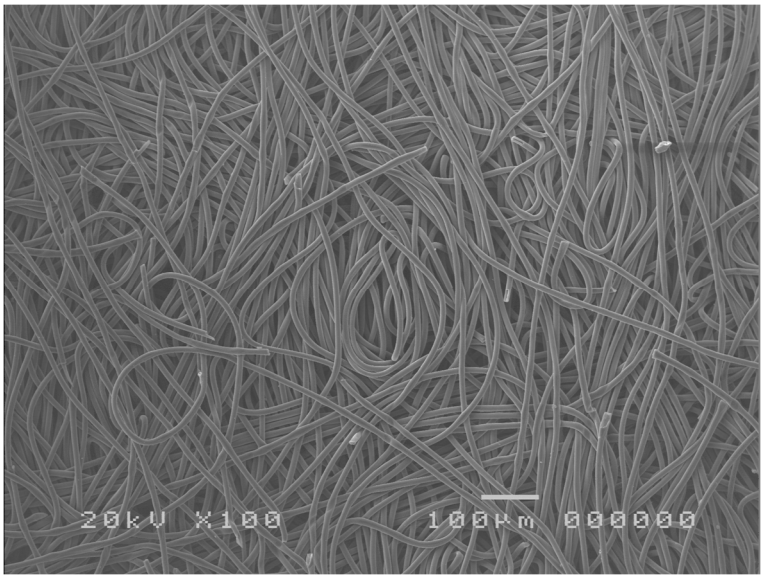

Figure 5.3 SEM micrograph of Freudenberg H2315 felt GDL sample.

5.2.2 X-ray Tomography Imaging

In this study, X-ray computed tomography (XCT) was used to generate 3D volumetric models of the GDL samples. The XCT is a non-invasive and non-destructive imaging technique for 3D visualisation of microstructures and, as such, it does not require extensive sample preparation. This technique has been successfully developed and applied by Ostadi et al. [19, 30, 31, 60, 69, 103-110, 159] for reconstruction of the woven and non-woven GDL samples for fluid flow analysis. There were three key steps involved in the 3D image generation, including progressive image acquisition, image reconstruction and image thresholding. Prior to the aforementioned processes, the sample preparation was carried out by carefully cutting a fine strip from the inner part of each sample, of about 2.5 mm, in order to obtain an approximate resolution of 1.25 μm/pixel. The sample size to be prepared was calculated by multiplication of the detector size and the targeted resolution. The preparation and following processes were applied to all tested samples.

5.2.2.1 Image Acquisition

The X-ray images of the samples were generated at a resolution of 1.25 μm using a desktop XCT scanner, a General Electric Phoenix nanotom® system with an X-ray source of 160kV (max) and 250μA (max). The sample was placed in a thin cylinder in front of the X-ray source, as shown in Fig. 5.4, and rotated step-by-step with a rotation step of 1 degree for 360 degrees in total. At each degree of rotation, 1 projection was captured by a 2304 × 2304 pixel^2 flat panel detector. Then, a set of 360 shadow images or projections was produced.

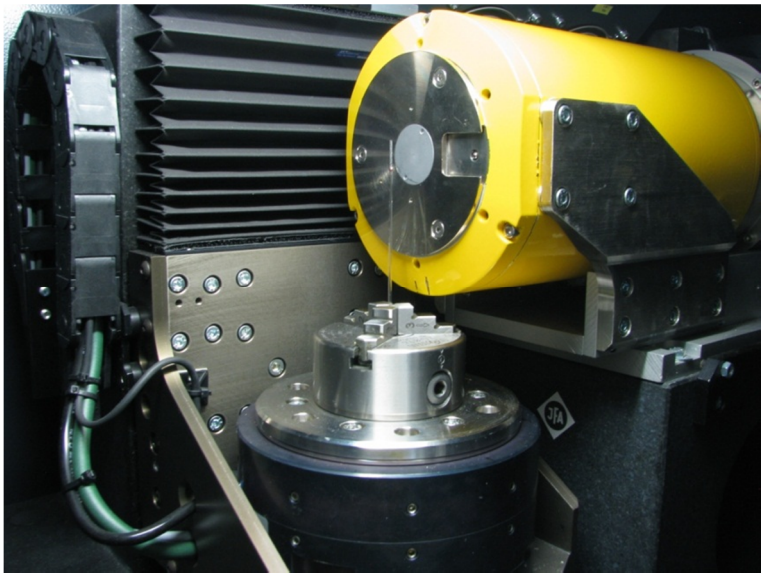

Figure 5.4 X-ray tomography imaging. A sample is placed in front of the X-ray source for image generation.

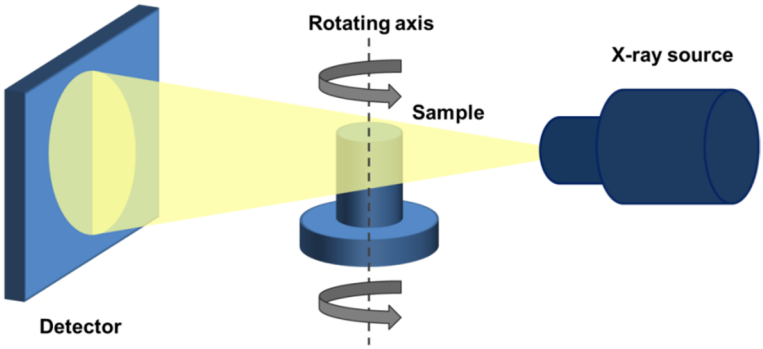

Figure 5.5 Schematic of X-ray tomography imaging technique. Adapted after [154].

5.2.2.2 Image Reconstruction

The 360 shadow images obtained from the process described above were then directly reconstructed into 3D volume using CT analyser software (Phoenix datos|x CT software) based on a filtered back-projection algorithm. This allowed the assembling of the images to be fully automated. The 3D reconstructed volume was then sliced in orthogonal planes to allow visualising from three different directions: one set of in-plane slices across the GDL thickness and two sets of through-plane slices crossing the width and length of the GDL samples.

5.2.2.3 Image Thresholding

In order to distinguish between solid and void space on the greyscale, a threshold process was carried out to turn the images into black-and-white binary images, in which solid spaces were represented by 1 and void spaces by 0. As described in [19, 159], this process required a reference image obtained using a scanning electron microscope (SEM). In this step, a 2D surface image from the reconstructed greyscale image was compared to the reference SEM image. The threshold level was then applied and progressively tuned until the average fibre diameter from the threshold image matched that of the SEM image [19, 159]. The decided threshold level was then applied to the entire stack of greyscale images. At this stage, all greyscale images were turned into binary image slices. In this study, the average fibre diameter measured from the SEM images was about 7.9, 8.2 and 9.5 μm for the Toray paper, SGL paper and Freudenberg felt respectively, which compared to the 8.0, 8.5 and 9.1 μm measured from the surface of the 3D digitally reconstructed image of each sample (as shown in Table 5.1). The errors in the average fibre diameter as a result of the threshold process were about 1.3, 3.7 and 4.2% for the Toray, SGL and Freudenberg respectively. Once the threshold process was completed, the pixel size of the image was then doubled to 2.5 μm. This was based on the findings from the previous study [175], which examined the effect of image resolution on the permeability of a carbon paper GDL using XCT and the LB model. Although the resolution variation had a significant impact on the resulting permeability in all flow directions, the 2.72 μm resolution showed the best compromise between permeability values and computational time. That study showed only about 8% difference in

permeability and took about 400 times less in computational time when compared to the base 0.68 μm resolution. This led to the decided image resolution for this work to be 2.5 μm/pixel. This was also in agreement with Hao and Cheng [29] in which the pixel size effect was tested on the stochastic model of the GDL with resolutions of 1.5 μm, 2.5 μm and 3.8 μm respectively, by performing drainage simulations where the 2.5 μm case showed almost the same results as the 1.5 μm case. The surface views of the reference SEM images and X-ray reconstructed images of each GDL sample are shown in Fig. 5.6 – Fig. 5.8. Examples of binary image slices of the three samples after the application of the threshold level are shown in Fig. 5.9 – Fig. 5.11.

Table 5.1 The average fibre diameter of the three tested samples measured in the SEM and X-ray reconstructed images.

Sample	Measured fibre diameter (μm)		
	SEM	**X-ray**	**% Error**
Toray TGP-H-120	7.9	8.0	1.3
SGL 24AA	8.2	8.5	3.7
Freudenberg H2315	9.5	9.1	4.2

The thresholded binary 2D cross-sectional images at 2.5 μm resolution were recombined to form a complete 3D digital representation of each GDL sample. Each binary element in the 3D digital model represents a cubic voxel equal to about 15.6 μm^3, where solid voxels are represented by 1 and void voxels are represented by 0. The digital and physical size of the Toray paper, SGL paper and Freudenberg felt are shown in Table 5.2. The sample size of 1125 μm × 1125 μm used in this study is in agreement with the sample size sensitivity analysis in [56], which was performed on paper, felt and cloth GDLs. They reported that a minimum 1000 μm × 1000 μm sample size was able to obtain a repeatable through-plane porosity distribution with less than 4% difference in distribution shape [56]. In this study, therefore, the sample size of 1125 μm × 1125 μm was sufficiently large to provide a repeatable result.

Table 5.2 Digital and physical size of Toray paper, SGL paper and Freudenberg felt GDLs.

Sample	**Toray TGP-H-120**	**SGL 24AA**	**Freudenberg H2315**
Resolution (μm/pixel)	2.5	2.5	2.5
Digital size (pixel^2)	450x450	450x450	450x450
Physical size (μm^2)	1125x1125	1125x1125	1125x1125

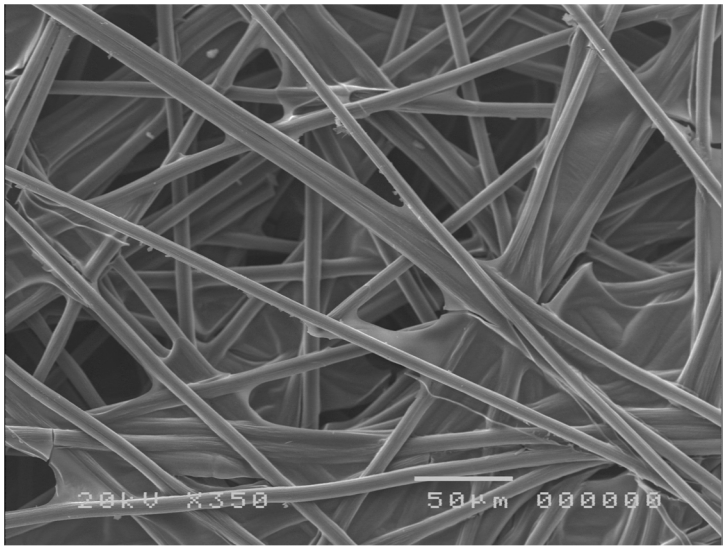

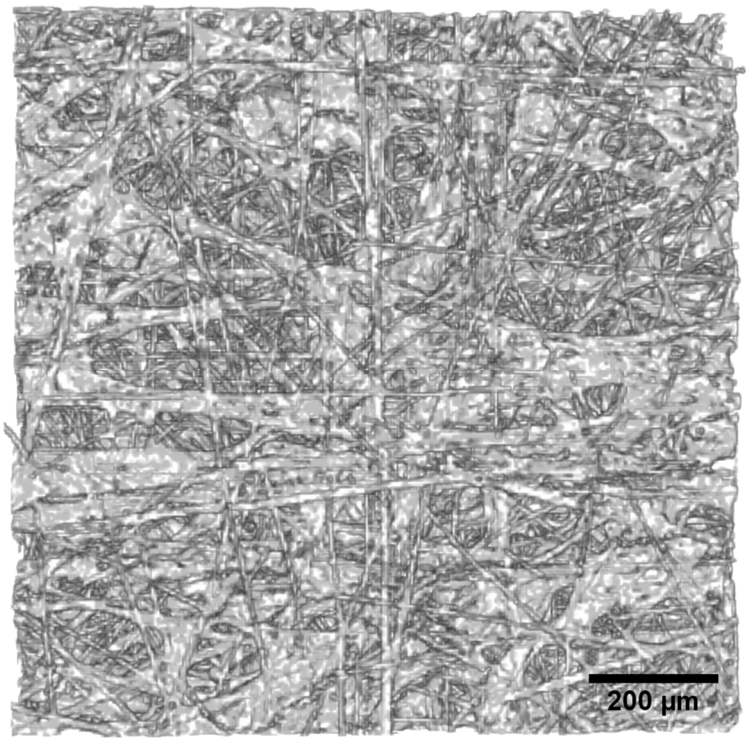

Figure 5.6 (a) SEM micrograph and (b) 2D surface X-ray reconstructed image of the Toray paper sample.

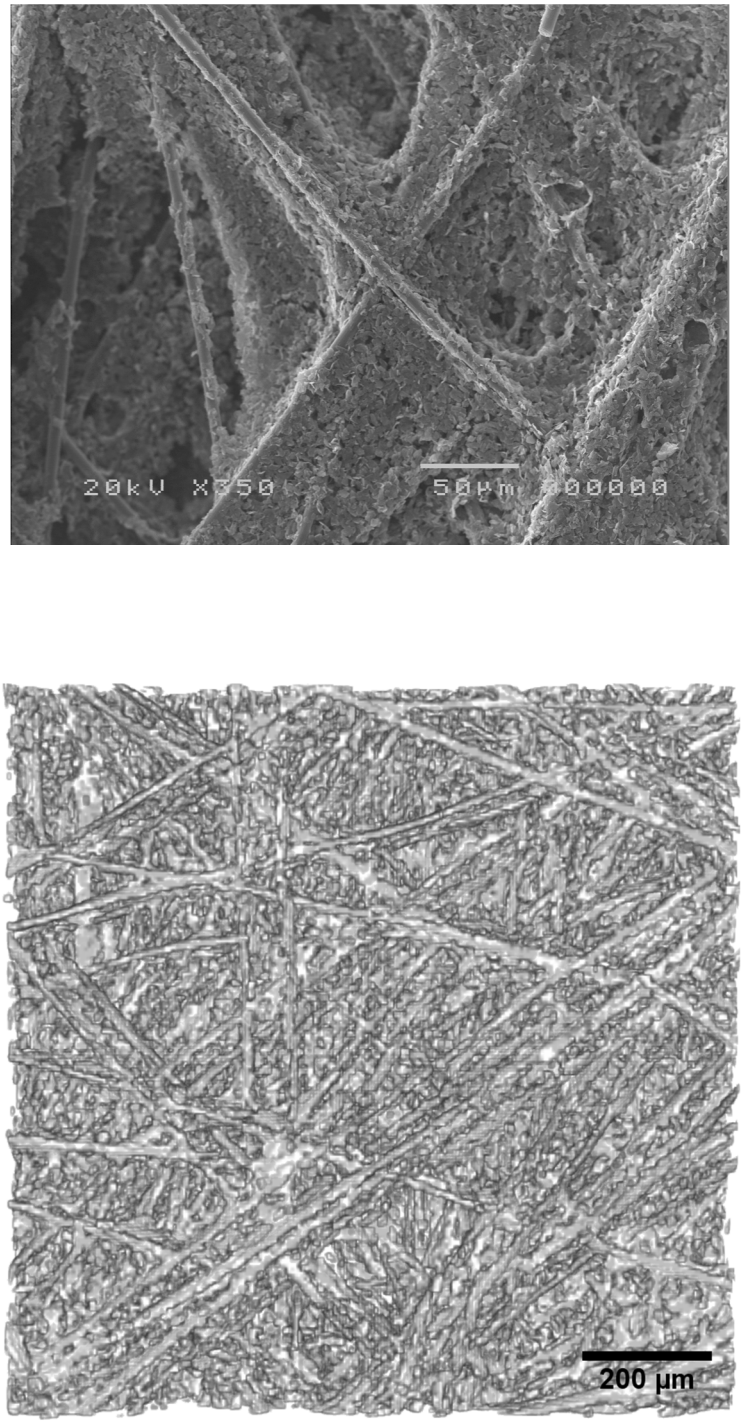

Figure 5.7 (a) SEM micrograph and (b) 2D surface X-ray reconstructed image of the SGL paper sample.

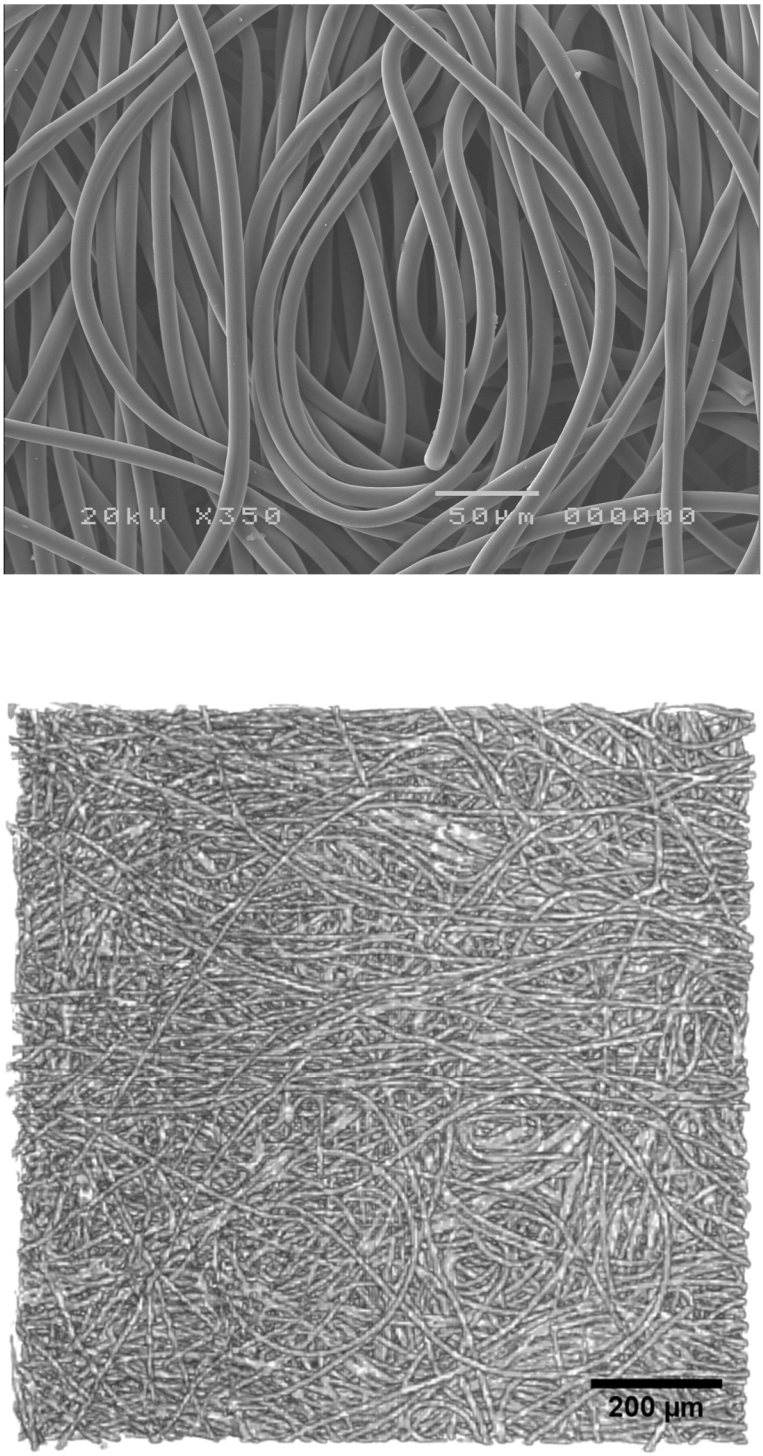

Figure 5.8 (a) SEM micrograph and (b) 2D surface X-ray reconstructed image of the Freudenberg felt sample.

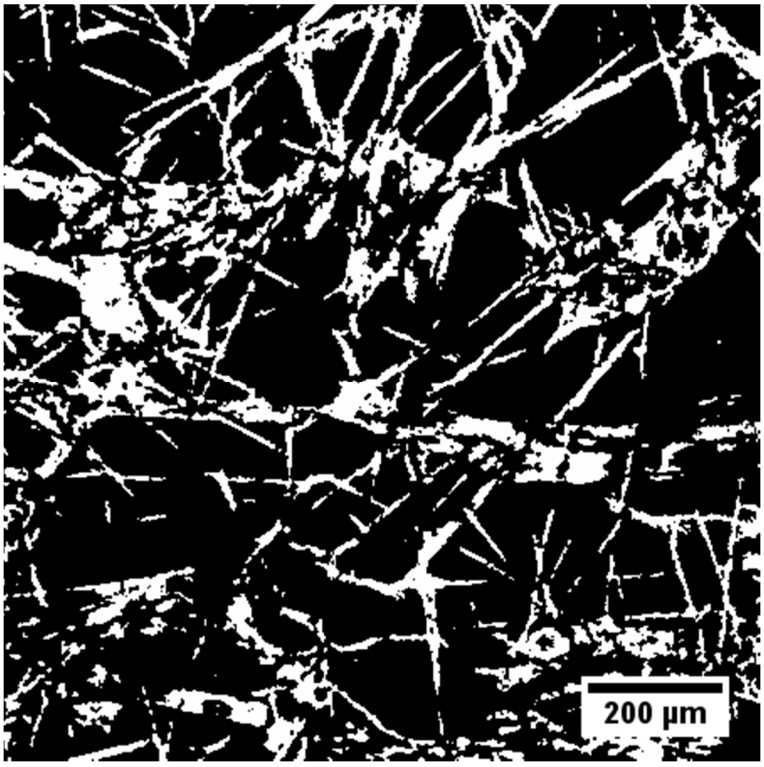

Figure 5.9 Binary image slice of the Toray paper GDL sample. The void spaces and solid phase are shown as black and white respectively.

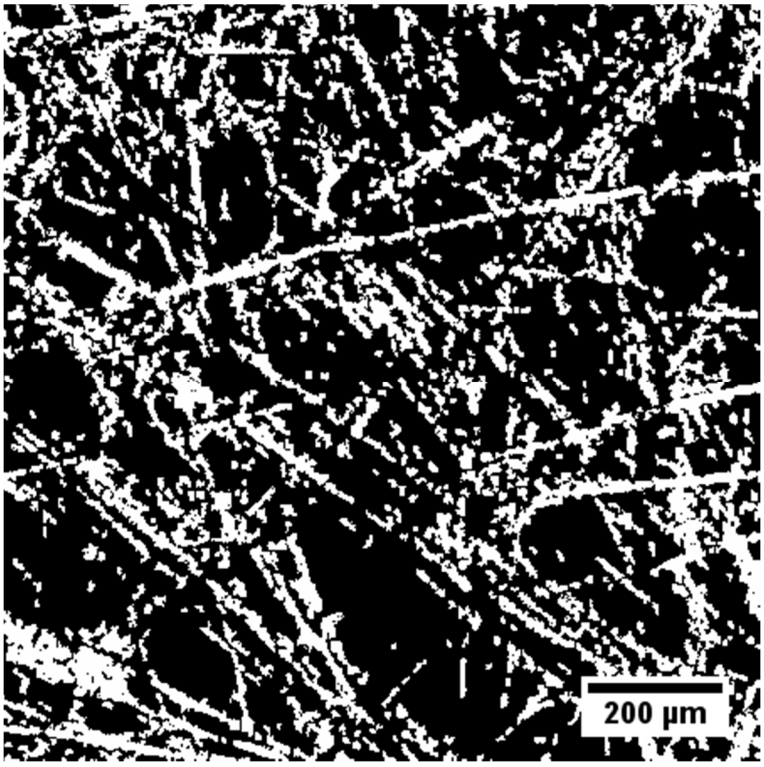

Figure 5.10 Binary image slice of the SGL paper GDL sample. The void spaces and solid phase are shown as black and white respectively.

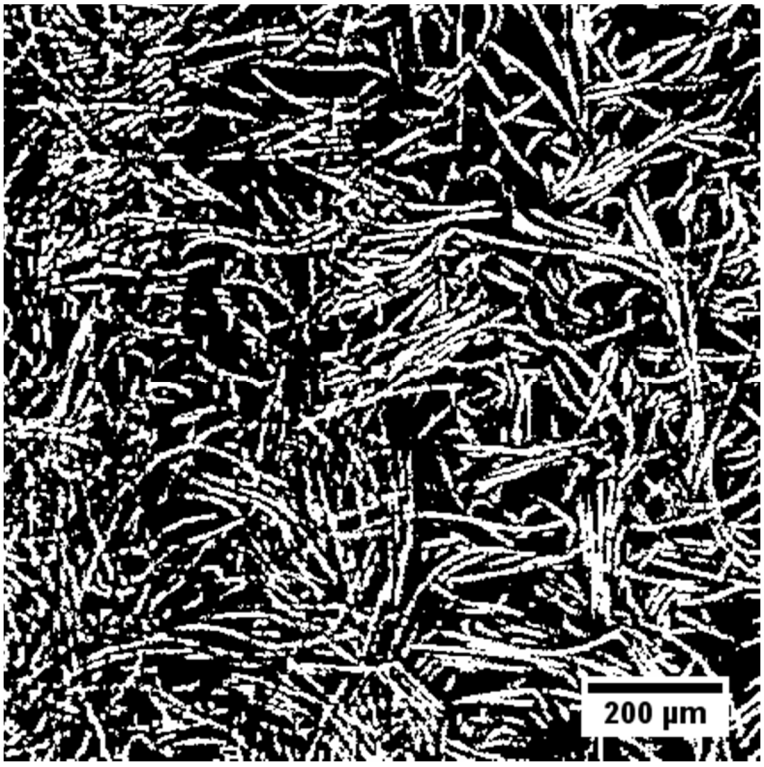

Figure 5.11 Binary image slice of the Freudenberg felt GDL sample. The void spaces and solid phase are shown as black and white respectively.

5.2.3 Thickness Estimation based on X-ray Tomography Images

In this work, the thickness of the GDL samples was measured directly based on the tomography images of each sample. Ten through-plane binary slices of each sample were chosen selectively from the entire stack of binary images for thickness measurement. For each slice, the thickness was measured at ten different positions by calculating the number of pixels in the thickness direction of the cross-sectional through-plane binary images of the X-ray reconstructed GDL samples. The ten selected slices of each sample chosen for measurement were evenly distributed throughout the stacks and the ten measuring points were located at equal distance on each slice. A binary slice from each GDL sample is shown in Fig. 5.12. The average measured thickness values of each sample with their standard deviation around the mean value are shown in Table 5.3 along with the thickness reported by corresponding manufacturers.

Table 5.3 Average measured thickness of Toray TGP-H-120 paper, SGL 24AA paper and Freudenberg H2315 felt GDLs.

	Average measured thickness (μm)		
GDL type	**Toray TGP-H-120**	**SGL 24AA**	**Freudenberg H2315**
Measured	360	190	222.5
SD	10.54	12.73	12.68
Manufacturer	363	190	222

Based on the direct measurement from the tomographic images, the average thickness of the Toray paper, SGL paper and Freudenberg felt is 360, 190 and 222.5 μm respectively. The standard deviations around the average values of each are 10.54, 12.73 and 12.68 μm respectively. As a percentage, therefore, the spread around the average measured value is 2.9%, 6.7% and 5.7% respectively. The average values of the measured thickness for each GDL sample closely agree with the thickness reported by manufacturers (Toray, Japan; SGL, Germany; Freudenberg, Germany) which are 363, 190 and 222 μm respectively for the corresponding GDLs. Throughout this chapter, these average values of the measured thickness are referred to as ‘effective thickness’.

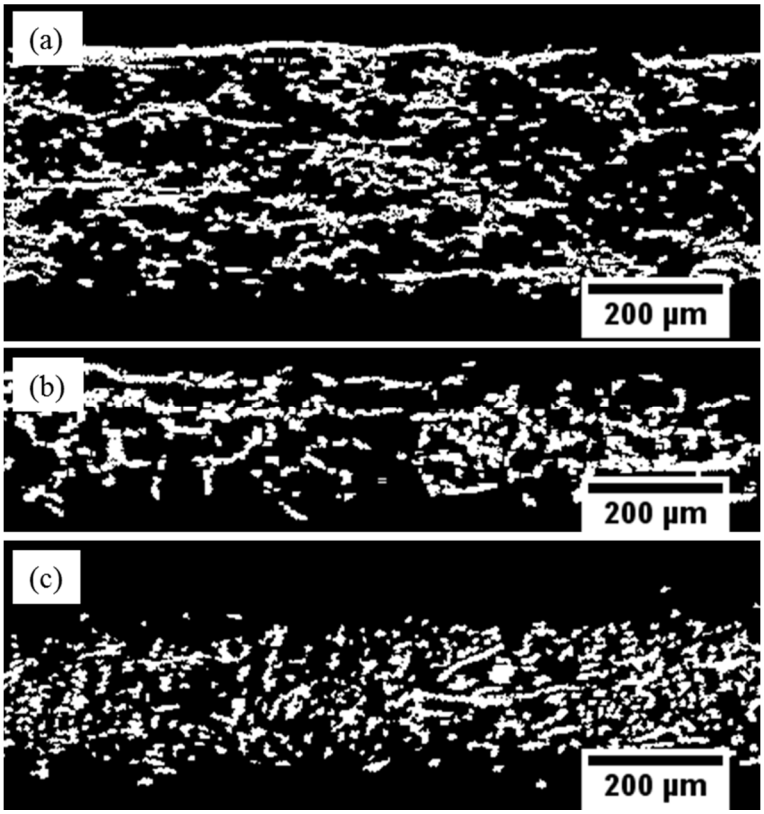

Figure 5.12 Binary slices of (a) Toray paper (b) SGL paper and (c) Freudenberg felt GDL samples.

5.2.4 Calculation of Permeability and Tortuosity through Analytical Modelling

5.2.4.1 Permeability

Gas permeability can be calculated through two analytical models, which include the Carman-Kozeny (CK) model as equation (1.6) and the Tomadakis and Sotirchos (TS) model. According to [62], the TS model is more convenient for modelling compared to the Carman-Kozeny model since the TS model does not require any fitting parameters. Instead, the model requires only porosity and fibre diameter as input parameters. In this chapter, the TS model was used to calculate the permeability for the GDL samples. The TS model for absolute permeability is as follows [174]:

$$K = \frac{\varepsilon}{8(\ln \varepsilon)^2} \frac{(\varepsilon - \varepsilon_p)^{(\alpha+2)} r_f^2}{(1-\varepsilon_p)^{\alpha} [(\alpha+1)\varepsilon - \varepsilon_p]^2} \tag{5.1}$$

where r_f is the fibre radius, ε is the porosity, ε_p is the percolation threshold porosity and α is a fitted value. The percolation threshold ε_p is the minimum porosity with an open-pore space required for permeation through the material [171]. The values of ε_p and α for various types of fibre structure and flow directionalities are listed in Table 5.4.

5.2.4.2 Tortuosity

In addition to calculating permeability as a function of porosity, the TS model can also be used to predict the tortuosity of the porous material [62]. Among different models, the Bruggeman model is the most widely used to calculate tortuosity [176]. This model, however, is based on the porosity of packed spherical particles, which do not resemble the GDL structure. In contrast, Tomadakis and Sotirchos [173] introduced the following tortuosity model based on the Monte Carlo simulations for randomly oriented fibrous porous media, which resembles more the GDL structure:

$$\tau = \left(\frac{1-\varepsilon_p}{\varepsilon - \varepsilon_p} \right)^{\alpha} \tag{5.2}$$

Table 5.4 Parameters used in the TS model, Eq. (5.1) and Eq. (5.2) [173, 174].

Structure	Flow direction	ε_p	α
1D	Parallel to fibres	0	0
	Normal to fibres	0.33	0.707
2D	Parallel to fibre planes	0.11	0.521
	Normal to fibre planes	0.11	0.785
3D	All directions	0.037	0.661

For PEMFC modelling, in addition, Nam and Kaviany [48] suggested the TS model for the GDL and the Bruggeman model for the CL. In this chapter, therefore, the TS model was used to calculate absolute gas permeability and tortuosity of the GDL samples.

5.3 Results and Discussion

5.3.1 Porosity Distribution based on X-ray Tomography Images

5.3.1.1 Local Through-Plane Porosity Distribution

The local porosity distribution profiles for the Toray TGP-H-120 paper, SGL 24AA paper and Freudenberg H2315 felt GDL samples in the through-plane direction are shown in Fig. 5.13 (a)-(c). The local porosity of each slice is defined as the ratio of the number of void voxels to the total GDL voxels. The total GDL voxels include both material voxels and void voxels. As seen in the porosity distribution figures (Fig. 5.13 (a)-(c)), the local through-plane porosity distribution of each tested sample can generally be divided into two surface regions and a centre or core region. The surface region is defined as the region from the surface of the GDL, which makes contact with open space outside the GDL to the core region of the GDL. The core region is defined as the region of the GDL situated between the two surface regions. The transition from the surface region to the core region is noted by the local minima of porosity at each side of the GDL. In this study, the thickness of the bulk volume (referred to as 'bulk thickness' throughout this chapter) is defined according to Fishman et al. [56], whereby each in-plane slice contains at least 1% solid material, which can capture the entire surface region with the exception

of the outermost frayed surface region. In addition to the bulk porosity value and the core porosity values, the effective porosity values which are calculated based on the effective thickness (see Section 5.2.3) are also reported and compared with the bulk value and core value.

For the Toray paper, porosity in the surface region decreases sharply towards the core region of the GDL. The transition from surface to core region for the Toray paper occurred at about 33.8 μm from the surface of each side. As seen, the surface regions contribute only about 17.5% of the entire GDL thickness, while the core region accounts for the majority of the GDL thickness with more than four fifths of the GDL thickness (82.5%). In the core region, where the GDL has a lower porosity value compared to the surface regions, the porosity distribution of the Toray paper exhibits as peaks and troughs consisting of 3 peaks and 4 troughs with a maximum peak-to-trough difference of about 11%. This is similar to the trend observed in [56], where peaks and troughs are shown in the core region. The peaks and troughs pattern suggests that the Toray TGP-H-120 paper, which is the thickest GDL in the TGP-H range, might consist of 4 or more plies of the thinner GDL in the same product range (Toray TGP-H-030), as pointed out by Mathias et al. [15], Gao et al. [77], Maheshwari et al. [177], Hinebaugh et al. [57] and Fishman et al. [56]. Mathias et al. [15] noted that the thicker paper GDL is composed of multiple thin plies compressed together. Similarly, Gao et al. [77] concluded that the thicker Toray paper GDLs are made of two or more plies of the thin TGP-H-030 ply. In addition, Maheshwari et al. [177] found that the performance of the PEMFC built from original Toray paper and from custom three-ply paper GDL were comparable. They pointed out that the Toray paper might be manufactured with the same method in which the thinner GDLs are layered and pressed together to make a thicker GDL. Considering the local porosity maxima in the core region of the Toray paper, these local maxima could be the result of pressing thinner plies together. According to Fishman et al. [56], the compression of two high porosity surface regions of two neighbouring plies would create a new region with a lower porosity, which appears as local maxima in the porosity distribution profile. As a result, the frequency of the porosity distribution variation indicates the number of plies, while the amplitude denotes the degree of compression for building a thicker GDL [56].

Conversely, the through-plane porosity distribution profile for the SGL paper exhibits a significant difference from the Toray paper. The surface regions of the SGL paper are considerably thicker, with approximately 82.5 μm thickness from the outer surface to the core region of the GDL. Unlike the Toray paper, the two surfaces of the SGL paper make up about 70% of the entire GDL thickness. The porosity decreases more slowly from the surface region to the core region compared to that of the Toray paper, where a sharp steep porosity profile was clearly observed on both sides of the GDL surface regions. For the core region, the porosity distribution of the SGL paper exhibits an inverted normal distribution or a valley with a lowest porosity of about 73%. The valley pattern together with a thin thickness of about 237.5 μm indicates that the SGL 24AA paper may consist of a single-ply layer in contrast to what was observed in the thick Toray TGP-H-120 paper, which was made up of multiple plies of a thinner GDL. The local porosity distribution of the SGL paper is also consistent with the porosity distribution results presented in [56], in which a single-ply paper GDL (Toray TGP-H-030) exhibits a valley trend and about two-thirds of its thickness consist of surface regions. The similar trend in porosity distribution between these two single-ply papers from different manufacturers (SGL 24AA in this study and Toray TGP-H-030 in [56]) suggests that these two papers were manufactured using similar procedures and that this is possibly a common porosity distribution characteristic found in any single-ply paper GDL. We attribute this similarity to the common process of paper fabrication of a single-ply paper GDL. Therefore, the peaks and troughs distribution observed in the Toray TGP-H-120 paper is very likely a result of the combination of several valleys of a single-ply paper GDL.

The through-plane porosity distribution profile for the Freudenberg felt GDL displays a distinct difference from the paper GDLs. The surface regions are thicker than those of the Toray paper and SGL paper, with approximately 87.5 μm for each side which contributes to more than half of the thickness (57.4% of the entire thickness) of the Freudenberg felt GDL. For the core region, the porosity displays a more uniform distribution with a maximum variation of only about 4.7% in contrast to what was observed in the paper GDLs, where the maximum variation was about 11.0% and 6.1% for the Toray paper and the SGL paper respectively. The uniform or smooth distribution profile in the core region of the felt GDL in contrast to the profile of the paper GDL was

also reported in [56] and [172]. The core porosity region exhibiting a more uniform distribution is possibly a result of the entanglement process used during fabrication. This entanglement process causes the felt fibres to travel in both in-plane and through-plane directions exhibiting a uniform porosity distribution. This agrees with the explanation in [172], where it was pointed out that the smooth porosity profile in the core region of the felt GDL was due to the anisotropic connection of its fibres in contrast to an almost 2D connection in paper GDL. In addition, Fishman et al. [56] reported a similar trend with a somewhat flat through-plane porosity distribution in the core region between two felt GDLs manufactured by two different manufacturers (Freudenberg and SGL) and attributed this similarity to the common procedure for felt fabrication (i.e. entanglement process).

Based on the definition of surface and core regions, the bulk thickness and the core thickness of the Toray paper, the SGL paper and the Freudenberg felt can be obtained. These values are shown in Table 5.5 along with the value of the effective thickness (measured in Section 5.2.3). In addition, the thickness values provided by corresponding manufacturers are also listed in Table 5.5 for comparison. As seen in Table 5.5, the effective thickness of each sample shows better agreement with the values reported by manufacturers than the bulk thickness and the core thickness.

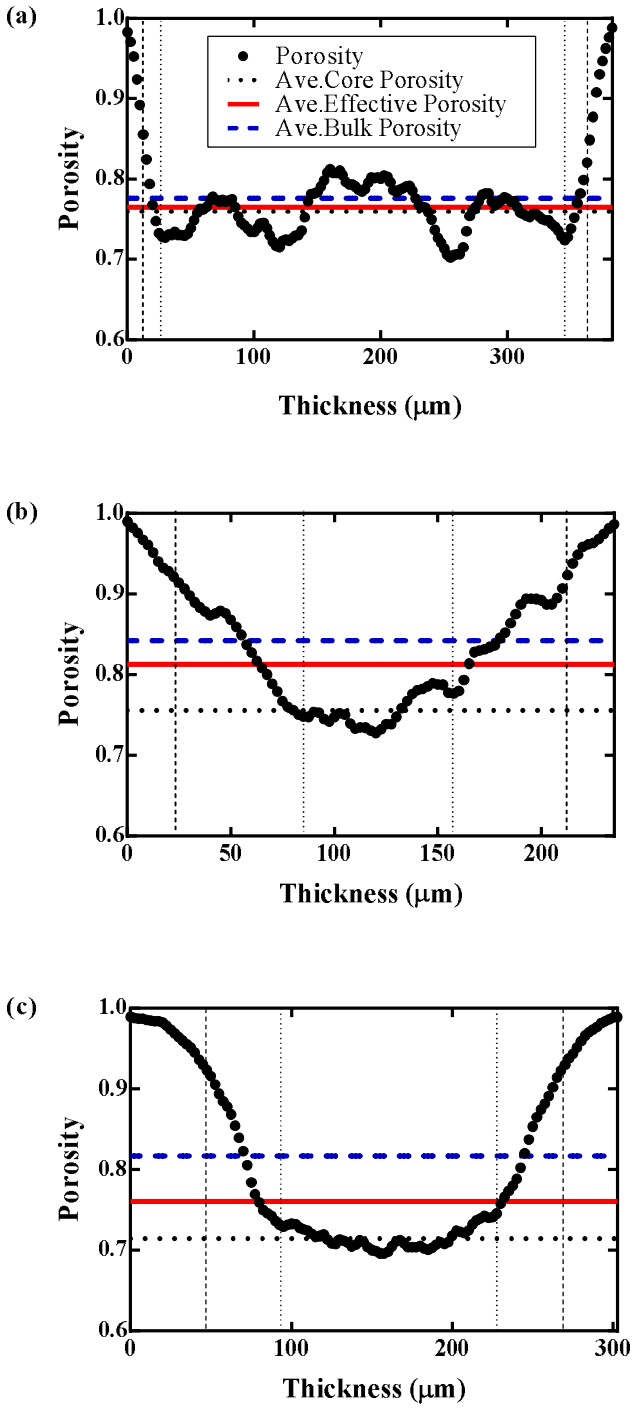

Figure 5.13 Porosity distributions in the through-plane direction for (a) Toray TGP-H-120 paper, (b) SGL 24AA paper and (c) Freudenberg H2315 felt GDL samples.

Table 5.5 Average bulk thickness, average effective thickness and average core thickness of Toray paper, SGL paper and Freudenberg felt GDLs compared to the thickness provided by corresponding manufacturers.

	Thickness (μm)			
GDL type	Bulk	Effective	Core	Manufacturer
Toray	385	360	317.5	363
SGL	237.5	190	150	190
Freudenberg	305	222.5	160	222

5.3.1.2 Average Porosity

The average bulk porosity, average effective porosity and average core porosity of the Toray paper, the SGL paper and the Freudenberg felt are listed in Table 5.6. As shown in Table 5.6, the average bulk porosity, average effective porosity and average core porosity of the Toray paper agree well with the porosity value reported by the manufacturer (0.78, Toray, Japan). In addition, the bulk and core values are almost identical to the values reported in [56] (0.787 and 0.76 respectively), which used the same method. For the SGL paper, the average values are significantly lower than the values reported in the literature (0.87 [178] and 0.88 [179]). The difference from the reported values is possibly due to the heterogeneous nature of the GDL and the batch-to-batch variation of GDL manufacturing. These factors may contribute to a different porosity value even within the same piece of GDL (area-to-area variation) and among different batches. This batch-to-batch variation is also referred to as lot-to-lot variability [180] and has been previously reported in [63, 170]. For the Freudenberg felt, the effective porosity value agrees well with the porosity value reported in the literature which ranges between 0.75-0.78 [181, 182], while the core value is significantly lower than the reported values. As the results suggested, the effective porosity, which was calculated based on the effective thickness in the previous section, shows good agreement with the values reported in the literature and the manufacturer's specifications.

Table 5.6 Average bulk porosity, average effective porosity and average core porosity of Toray paper, SGL paper and Freudenberg felt GDLs compared to the porosity values provided by the corresponding manufacturers and reported in the literature.

	Porosity			
GDL type	Bulk	Effective	Core	Manufacturer/Literature
Toray	0.776	0.763	0.760	0.780
SGL	0.842	0.813	0.756	0.87-0.88
Freudenberg	0.817	0.761	0.715	0.75-0.78

5.3.2 Local Through-Plane Permeability Distribution

The through-plane permeability distributions of the Toray paper, SGL paper and Freudenberg felt plotted in logarithm scale are shown in Fig. 5.14 (a)-(c) and the average values of the bulk permeability, the effective permeability and the core permeability of each GDL are presented in Table 5.7. The permeability distribution figures show that the through-plane permeability of each GDL exhibits a corresponding variation to the through-plane porosity distributions respectively.

The distribution of the through-plane permeability for the Toray paper shows a similar pattern to the through-plane porosity distribution, displaying as peaks and troughs in the core region of its thickness. In the core region, the through-plane permeability of the Toray paper has a maximum peak-to-trough variation ranging from 2.19×10^{-12} to 8.56×10^{-12} m^2. The permeability sharply increases from the core region and reaches maximum values at its surfaces on both sides of the GDL structure. The average bulk permeability, average effective permeability and average core permeability in the through-plane direction are 5.69×10^{-11}, 5.16×10^{-12} and 4.59×10^{-12} m^2 respectively. Considering these permeability values, the values of the effective permeability (5.16×10^{-12} m^2) and the core permeability (4.59×10^{-12} m^2) are in agreement with the permeability reported by the manufacturer (8.54×10^{-12} m^2), as listed in Table 5.7. In contrast, the bulk permeability value is one order of magnitude larger than that of the manufacturer.

For the SGL paper, the through-plane permeability distribution shows an inverted normal distribution curve. In the core region, the through-plane permeability of the SGL

paper shows variation ranging from 3.15×10^{-12} to 6.70×10^{-12} m^2. The permeability of the SGL exponentially increases from its lowest point at the middle of the core region towards both ends of the GDL. The average bulk permeability, average effective permeability and average core permeability in the through-plane direction are 2.00×10^{-10}, 1.61×10^{-11} and 4.55×10^{-12} m^2 respectively. Interestingly, the bulk permeability (2.00×10^{-10} m^2) is two orders of magnitude larger than the typical permeability values reported in the literature [15]. Again, the effective permeability seems to have a better agreement with the literature.

As with the SGL paper, the through-plane permeability profile of Freudenberg felt exhibits an inverted normal distribution with greater uniformity in the centre region of the GDL. The through-plane permeability of the Freudenberg felt in the core region shows a slight variation ranging from 2.69×10^{-12} to 4.59×10^{-12} m^2, which is much smaller than what was observed in the paper GDLs. The permeability steadily increases from the core region and reaches maximum values at its surfaces on both sides of the GDL structure. The average bulk permeability, average effective permeability and average core permeability are 5.38×10^{-10}, 1.29×10^{-11} and 3.36×10^{-12} m^2 respectively. Once again, while the average bulk permeability is two orders of magnitude larger than the value reported by the manufacturer (8.36×10^{-12} m^2), the effective permeability shows better agreement with the value reported by the manufacturer.

According to Fishman et al. [171], the massive difference of the average bulk porosity values to the values reported in the literature by one to two orders of magnitude can be explained by the absence of surface regions in experimental investigations. In experiments, a GDL is actually in contact with the testing apparatus, which can lead to a decrease of GDL thickness. In contrast, the tested GDLs in this study were completely uncompressed. Therefore, it is reasonable to correlate the reported permeability values from the manufacturers and the literature with the effective values calculated in this study.

Overall, the average effective permeability values of each sample shows better agreement with the values reported by the manufacturers than the average bulk values and the average core values. In addition, it was found that the SGL paper exhibits the greatest

effective permeability value of 1.61×10^{-11} m^2, while the Toray paper has the lowest value of 5.16×10^{-12} m^2.

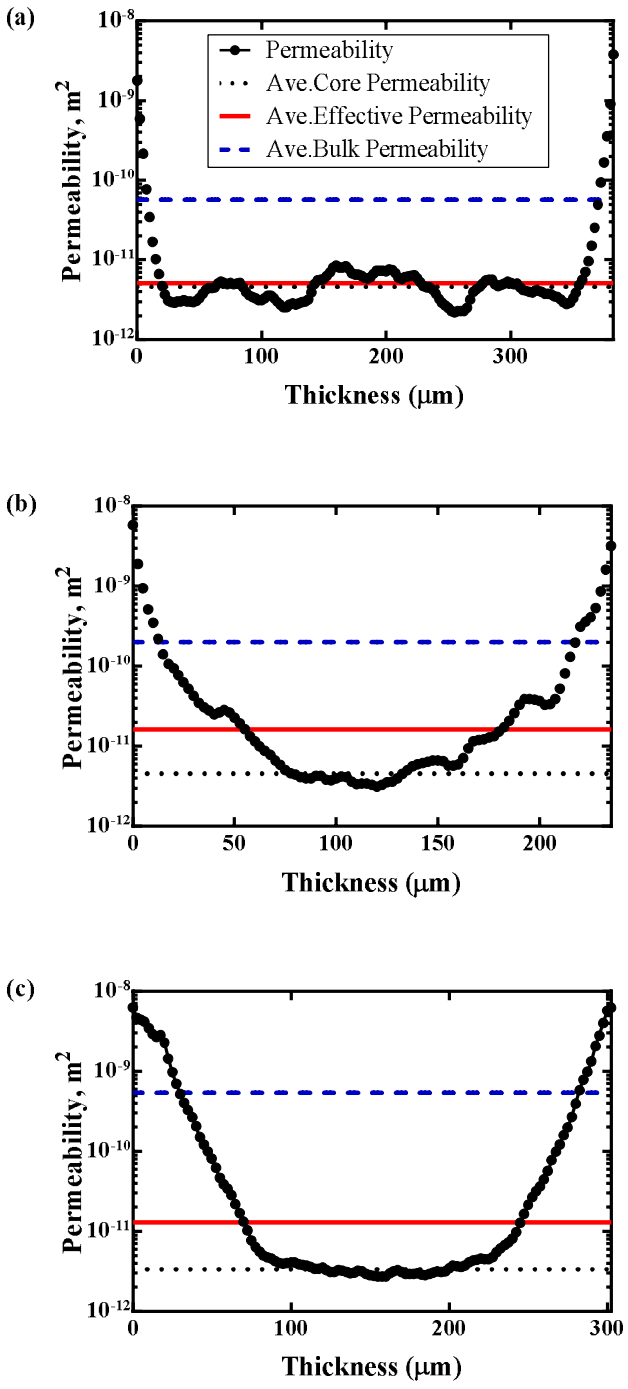

Figure 5.14 Permeability distributions in the through-plane direction for (a) Toray TGP-H-120 paper, (b) SGL 24AA paper and (c) Freudenberg H2315 felt GDL samples.

Table 5.7 Average bulk permeability, average effective permeability and average core permeability in the through-plane direction of Toray paper, SGL paper and Freudenberg felt GDLs based on the TS model, compared to the permeability provided by the corresponding manufacturers.

	Through-plane permeability × 10^{-12} m^2			
GDL type	Bulk	Effective	Core	Manufacturer
Toray	56.904	5.163	4.589	8.539[1]
SGL	200.308	16.102	4.551	-
Freudenberg	538.282	12.881	3.360	8.355[2]

[1] The permeability values were calculated from 412 l/m^2s based on the EN ISO 9237 standard (Toray, Japan).

[2] The permeability values were calculated from 1.65 × 10^3 ml·mm/(cm^2·hr·mmAq) based on the EN ISO 9237 standard (Freudenberg, Germany).

5.3.3 Local Through-Plane Tortuosity Distribution

Fig. 5.15 (a)-(c) show through-plane tortuosity distribution for the Toray paper, SGL paper and Freudenberg felt, calculated based on the TS model. The through-plane tortuosity of the paper (Toray and SGL) and felt (Freudenberg) GDLs are inversely proportional to the through-plane porosity distributions, where the local tortuosity maxima correspond to the local porosity minima and the local tortuosity minima correspond to the local porosity maxima. The average bulk tortuosity, average effective tortuosity and average core tortuosity are listed in Table 5.8.

In the core region of the paper GDLs, the through-plane tortuosity distribution of the Toray paper displays as peaks and troughs, while exhibiting a normal distribution curve for the SGL paper. For the Freudenberg felt, similar to the SGL paper, the through-plane tortuosity of the felt GDL displays a normal distribution curve albeit with a more uniform distribution of tortuosity in the core region.

According to Table 5.8, the average bulk tortuosity, average effective tortuosity and average core tortuosity of the three samples are almost similar displaying only a

small variation ranging from 1.175 to 1.262 for bulk tortuosity, 1.210 to 1.288 for effective tortuosity and 1.282 to 1.354 for core tortuosity. As observed, the core region shows the greatest tortuosity values suggesting that the core region of each sample is more heterogeneous than the surface region.

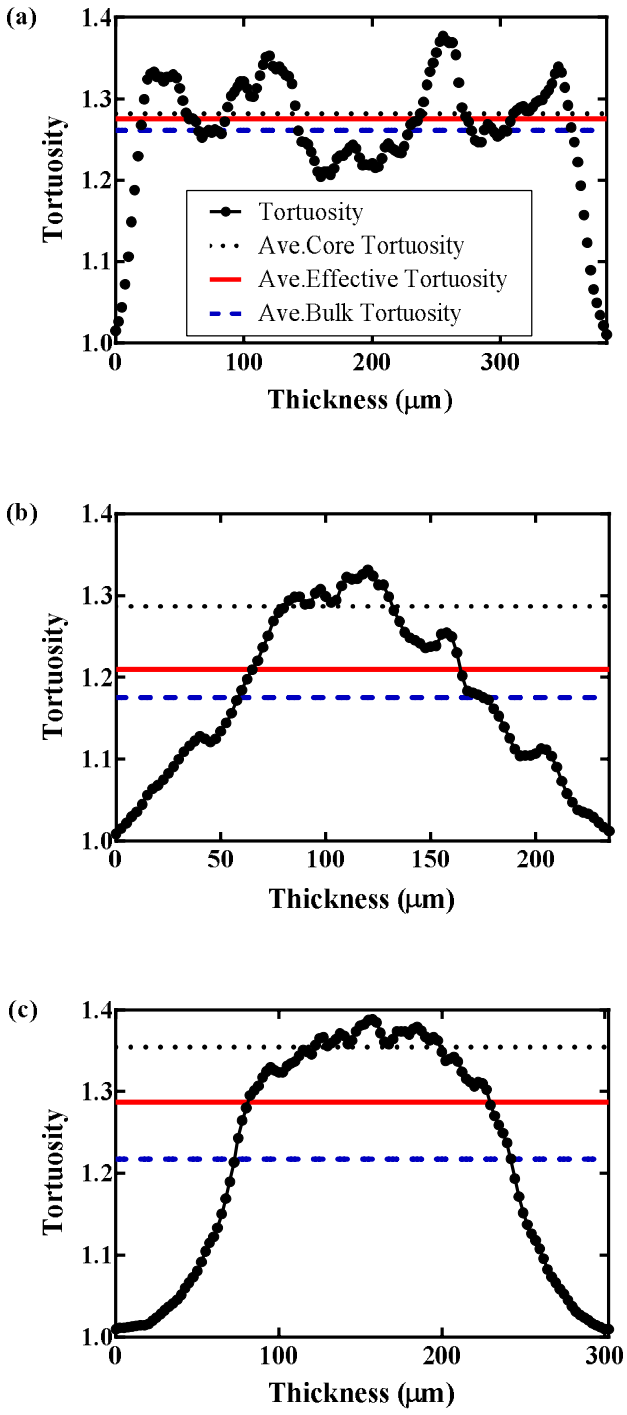

Figure 5.15 Tortuosity distributions in the through-plane direction for (a) Toray TGP-H-120 paper, (b) SGL 24AA paper and (c) Freudenberg H2315 felt GDL samples.

Table 5.8 Average bulk tortuosity, average effective tortuosity and average core tortuosity in the through-plane direction of Toray paper, SGL paper and Freudenberg felt GDLs calculated based on the TS model.

	Through-plane tortuosity		
GDL type	Bulk	Effective	Core
Toray	1.262	1.277	1.282
SGL	1.175	1.210	1.287
Freudenberg	1.218	1.288	1.354

5.4 Conclusions

In this chapter, we reconstructed the 3D digital binary volumetric models of the untreated GDL samples with paper and felt structures using the X-ray computed tomography technique. The key material parameters of each reconstructed GDL sample, including thickness, porosity, tortuosity and permeability, were characterised. The thickness and the local porosity distributions of each GDL were examined based on cross-sectional binary slices. The resulting local through-plane porosity distributions were then used to predict local through-plane tortuosity and permeability distributions using the Tomadakis and Sotirchos (TS) model.

This work has demonstrated the heterogeneous through-plane distribution of porosity, tortuosity and permeability. For porosity distribution, the paper-type and felt-type GDLs exhibit a distinct difference in through-plane porosity distribution. The felt GDL presents a core region that is more uniform than the paper one. On the other hand, the GDLs with paper structure exhibit a valley pattern distribution and peaks and troughs distribution for the thin paper and thick paper respectively. Based on the TS model, the local tortuosity and permeability distributions of each sample were examined. It was observed that the tortuosity distribution is inversely proportional to the porosity distribution, whilst the permeability distribution exhibits a similar trend with that of porosity. For each property, the average value was determined for the bulk region, effective region and core region. Better agreement was found with the average values of

the effective region, which were defined based on the thickness measured directly from the tomographic binary slices, and the values reported in the literature.

In Chapter 7, the X-ray reconstructed models of the GDL samples were employed to investigate the behaviour of liquid water in the GDL samples. Additionally, the local porosity distribution of each GDL observed in this chapter was used as additional information for understanding water transport behaviours in the GDL structures.

Chapter 6
Characterisation of Permeability and Tortuosity of Gas Diffusion Layers using the Lattice Boltzmann Method

6.1 Introduction

In the previous chapter, we characterised the through-plane distribution of some key material properties of the GDL samples, including porosity, tortuosity and permeability, using tomography images and an analytical model available in the literature, namely the Tomadakis and Sotirchos (TS) model. The results illustrated the heterogeneous distribution of each property across the thickness for each sample. It was also found that the average porosity, permeability and tortuosity calculated based on the effective thickness, which measured directly from the tomography images, provided better agreement with data reported in the literature. The TS model, however, which originally developed based on a structure of randomly distributed cylindrical straight fibres, could lead to unrealistic results since the GDL structures are not actually found in such an idealised shape. Conversely, the Lattice Boltzmann (LB) model can incorporate the actual structure of the GDLs into the model and has been increasingly utilised to investigate flows in complex geometries like those of the GDLs. In this chapter, therefore, the single-phase LB model was employed to characterise the absolute through-plane permeability and tortuosity of the GDL samples. The results from the two models were then compared and validated against data in the literature. The GDL samples with their effective thickness were integrated into the model to simulate gas flow through each sample at microscopic scale and the detailed velocity distribution in the void space of each sample domain was then used to calculate the permeability and tortuosity of each GDL sample.

6.2 Single Phase Lattice Boltzmann Modelling

In this chapter, the three-dimensional single-phase single-relaxation-time (SRT) LB model with the D3Q19 scheme developed by the University of Liverpool was utilised to simulate gas flow through the GDL samples. In the LB model, a pressure difference was applied to each GDL domain in the thickness direction to drive the flow through it, while

the other four sides were treated as periodic boundaries where the particles exiting the domain from one side re-enter through its opposite side. The bounce-back scheme for no-slip boundaries was used to solve fluid-solid boundary conditions by assuming that any fluid particle that hits a solid boundary during the streaming step is simply bounced back to its original position at the end of each time step. The SRT LB model has been described in Chapter 2 (Section 2.4) and the D3Q19 scheme has been shown in Fig. 2.2.

6.3 Permeability Calculation

In the LB model, a pressure difference is applied to two opposite sides of the domain to drive the flow. The detailed gas velocity distribution in the void space of the GDL domain at the microscopic scale obtained in the LB simulation is then used to calculate the absolute permeability at the macroscopic scale by using Darcy's law. The detailed explanation and key equations for permeability calculation have been described in Chapter 4 (Section 4.3).

6.4 Tortuosity Calculation

In the LB model, tortuosity is defined as the ratio of the flow path length of fluid particles to the average distance that these travel in the pressure gradient direction. The GDL is highly anisotropic, its tortuosity, therefore, varies with flow direction and can be calculated based on the method used by Nabovati and Sousa [183]. When the pressure difference is applied in an arbitrary direction j, the tortuosity in the j direction is:

$$\tau_j = \frac{\sum_i u_{ave}(x_i)}{\sum_i \left| u_j(x_i) \right|} \tag{6.1}$$

where u_j is the velocity component in direction j and u_{ave} is the velocity magnitude calculated from:

$$u_{ave}(x_i) = \sqrt{u_x(x_i)^2 + u_y(x_i)^2 + u_z(x_i)^2} \tag{6.2}$$

6.5 Simulation

GDL samples with effective thickness obtained from Chapter 5 were employed in this study. The digital and physical size of the Toray paper, SGL paper and Freudenberg felt GDL samples are as shown in Table 5.2. The reconstructed 3D images of each GDL sample were saved as a 3D array of binary digits. Each binary digit represents a voxel where 0 indicates void space and 1 indicates solid space. Due to the limitations of computational power, each GDL sample was equally spilt into 4 small portions in order for our computers to handle the LB calculations. The sizes and porosities of each portion for each GDL sample are shown in Table 6.1 and Table 6.2 respectively. The 4 split regions of each sample are shown in Fig. 6.1 – Fig. 6.3. The porosity values are also illustrated in Fig. 6.4. In order to characterise the absolute permeability of each GDL sample, the pressure difference of 10 Pa was applied to each region of the GDL samples. The entire void space was assumed to be filled with air and the principal flow direction was set to be in the through-plane direction.

Table 6.1 Digital and physical size of each simulated region (regions 1-4) for LB simulation of Toray paper, SGL paper and Freudenberg felt GDLs.

Sample	**Toray TGP-H-120**	**SGL 24AA**	**Freudenberg H2315**
Resolution (μm/pixel)	2.5	2.5	2.5
Digital size (pixel^3)	225x225x144	225x225x76	225x225x89
Physical size (μm^3)	562.5x562.5x360	562.5x562.5x190	562.5x562.5x222.5

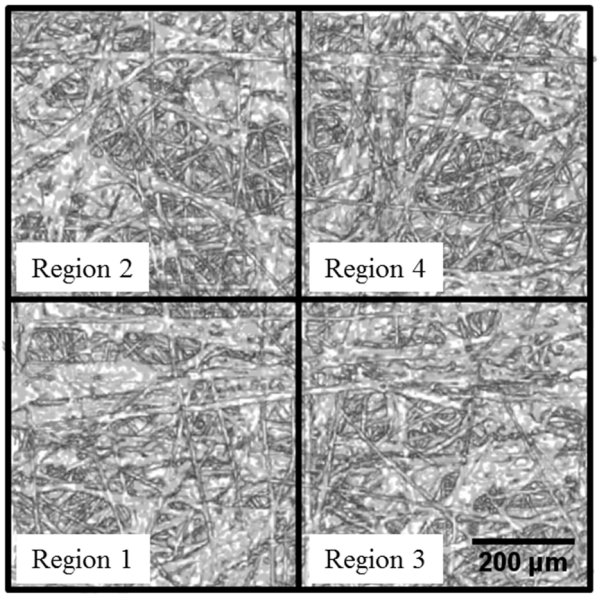

Figure 6.1 2D image of the X-ray reconstructed Toray TGP-H-120 paper GDL.

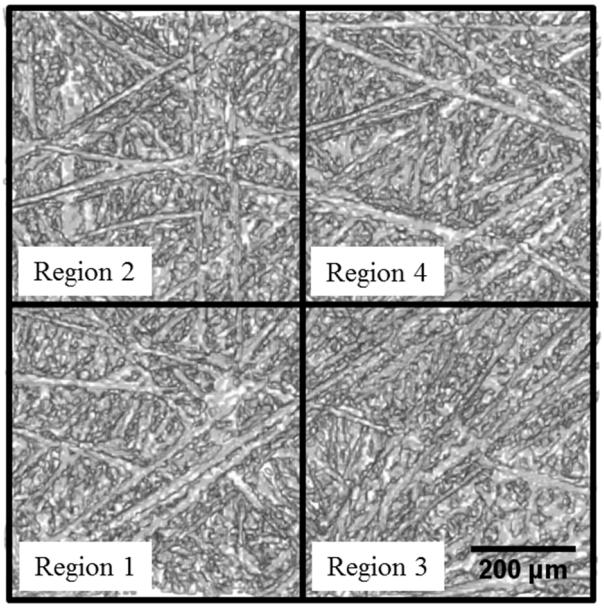

Figure 6.2 2D image of the X-ray reconstructed SGL 24AA paper GDL.

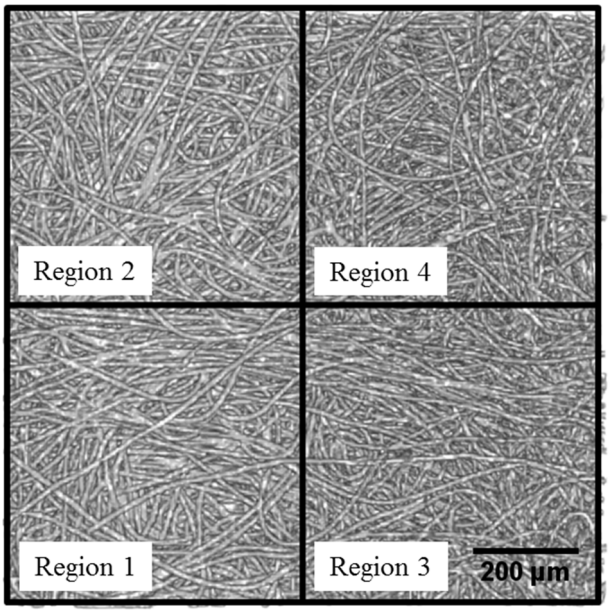

Figure 6.3 2D image of the X-ray reconstructed Freudenberg H2315 felt GDL.

6.6 Results and Discussion

6.6.1 Local Porosity

Fig. 6.4 shows the porosity for each of the 4 regions and the mean porosity values for the Toray paper, SGL paper and Freudenberg felt GDL samples. In addition, the porosity values reported in the literature are also included in Fig. 6.4. The porosity values of all Toray regions are almost identical, with only 0.3% deviation around the mean porosity (0.763), while a slightly larger deviation of about 1.4% around the mean value (0.813) for the SGL regions and a significantly larger deviation of about 3.3% around the mean value (0.761) for the Freudenberg felt regions were observed. This suggests that the Toray paper has a more uniform structure along the planar direction than the SGL paper and Freudenberg felt. The Freudenberg felt, on the other hand, is more heterogeneous along the planar direction than the paper GDLs. According to the figure above, the porosity values of the Toray paper and the Freudenberg felt show good agreement with the values reported in the literature whilst the value of the SGL paper shows a noticeable variation of about 6% from the value reported in [178]. As discussed in the Chapter 5 (Section

5.3.1.2), we attribute this porosity difference to the batch-to-batch variation and the heterogeneous nature of the GDL. Regarding the porosity values reported in Fig. 6.4, various methods have been employed to determine the porosity for GDLs. Cho and Mench [178] employed the immersion method to determine the porosity for the SGL. Totzke et al. [182] calculated porosity for the Freudenberg felt directly from the image result of the GDL obtained by synchrotron X-ray imaging. Likewise, Parikh et al. [181] calculated the porosity for the Freudenberg felt from the SEM image analysis.

Table 6.2 Porosity of each simulated region (regions 1-4) of the Toray paper, SGL paper and Freudenberg felt GDLs.

Sample	Toray TGP-H-120	SGL 24AA	Freudenberg H2315
Region 1	0.760	0.807	0.797
Region 2	0.766	0.835	0.737
Region 3	0.766	0.811	0.788
Region 4	0.761	0.798	0.721
Mean	0.763	0.813	0.761
SD	0.003	0.014	0.033

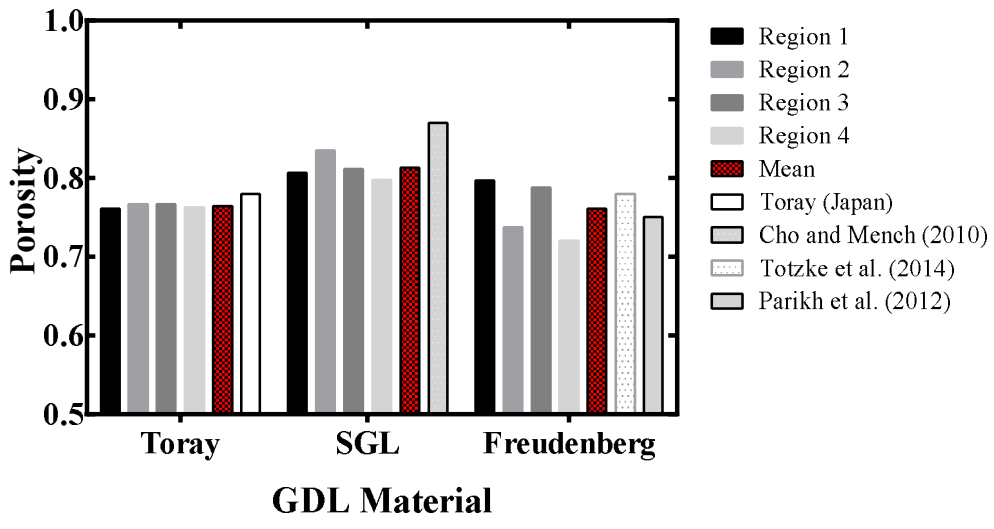

Figure 6.4 Comparison of porosity values of regions 1-4 and their means for Toray paper, SGL paper and Freudenberg felt against some of the available data in the literature.

6.6.2 Through-Plane Absolute Permeability

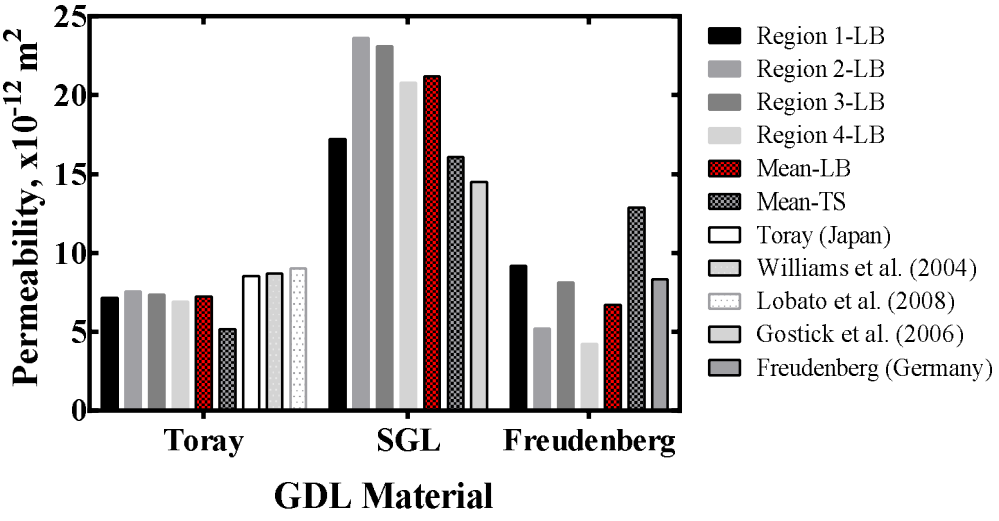

Figure 6.5 Comparison of the LB simulated through-plane permeability values of regions 1-4 and their means for Toray paper, SGL paper and Freudenberg felt against the mean values from the TS model and some of the available data in the literature.

Fig. 6.5 shows the simulated through-plane permeability for each of the 4 regions and the mean values based on LB simulation for the Toray paper, SGL paper and Freudenberg felt GDL samples. For comparison, the mean effective permeability values calculated based on the TS model and some of the values reported in the literature are also included in the figure. All values are in the through-plane direction. The mean simulated absolute permeability in the through-plane direction based on the LB model of the Toray paper, SGL paper and Freudenberg felt are 7.239×10^{-12} m^2, 21.193×10^{-12} m^2 and 6.693×10^{-12} m^2 respectively. The mean permeability of the Toray paper and the Freudenberg felt based on the LB model closely agree with the values reported by the manufacturers (8.539×10^{-12} m^2 for the Toray paper and 8.355×10^{-12} m^2 for the Freudenberg felt). For the Toray paper, the mean permeability based on the LB model also falls within the values reported in the literature. Using the in-house apparatus, Williams et al. [50] measured the permeability of gas flow through a Toray TGP-H-120 paper and reported

the value of 8.69×10^{-12} m^2. Lobato et al. [184] conducted a similar test with the in-house apparatus and reported the value of 9.21×10^{-12} m^2. Compared to the Toray paper, permeability values reported in the literature for the SGL paper (SGL 24AA) and Freudenberg felt (Freudenberg H2315) are relatively rare. For the SGL 24AA, there is no permeability value provided in the literature. The value for this SGL 24AA paper, however, can be reasonably compared with the value reported for the SGL 24BA paper since it has the same structure with the SGL 24AA, albeit with 5% PTFE added. Gostick et al. [62] reported the value of 14.5×10^{-12} m^2 for the SGL 24BA by using the in-house testing apparatus for through-plane permeability. Based on the value reported by Gostick et al. [62], we can reasonably expect a higher permeability value for the SGL 24AA, as it is a plain GDL without PTFE coating. Therefore, the permeability value of the SGL 24AA paper calculated based on the LB model in this study seems to be in reasonable agreement with the value reported by Gostick et al. [62].

Conversely, based on the TS model, the through-plane permeability for the Toray paper, SGL paper and Freudenberg felt are 5.163×10^{-12} m^2, 16.102×10^{-12} m^2 and 12.881×10^{-12} m^2 respectively. Comparing the permeability values based on the TS model and the LB model, the values based on the latter show better agreement with the values provided by the manufacturers and those reported in the literature. Again, this can be attributed to the capability of the LB approach to incorporate the actual structure of the GDLs into the model, which can thus provide a more realistic result.

6.6.3 Through-Plane Tortuosity

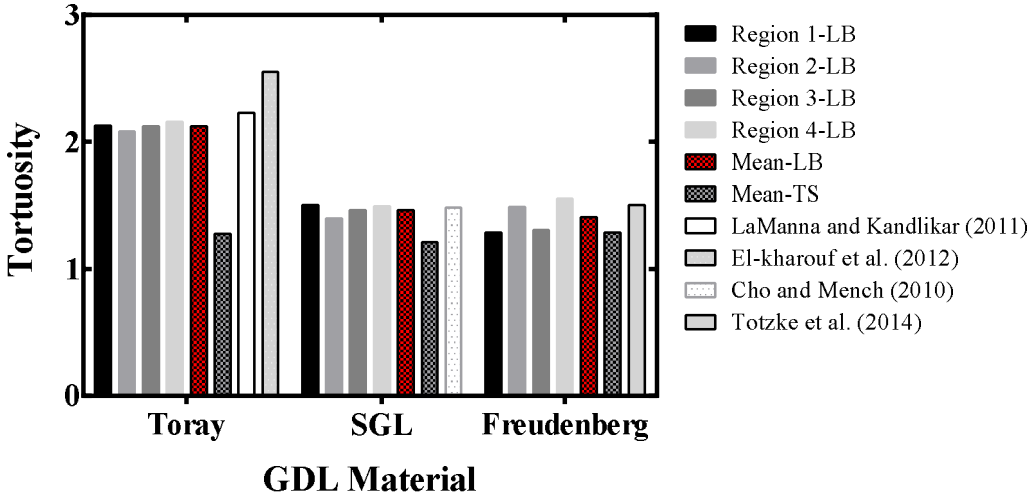

Figure 6.6 Comparison of the LB simulated through-plane tortuosity values of regions 1-4 and their means for Toray paper, SGL paper and Freudenberg felt against the mean values from the TS model and some of the available data in the literature.

Fig. 6.6 shows the simulated through-plane tortuosity for each of the 4 regions and the mean values based on LB simulation for the Toray paper, SGL paper and Freudenberg felt GDL samples. For comparison, the mean effective tortuosity values calculated based on the TS model and some of the values reported in the literature are also presented in the figure. All values are in the through-plane direction. For the Toray paper, the mean tortuosity value calculated based on the LB model and the TS model differ considerably. The mean value of the 4 regions simulated by the LB model is 2.123 and the mean value based on the TS model is 1.277. Using the LB approach, the tortuosity value shows better agreement with the values reported in the literature. LaManna and Kandlikar [185] reported a tortuosity value of 2.23 based on the effective diffusion coefficient obtained experimentally, whilst El-kharouf et al. [186], using a mercury porosimeter, reported a tortuosity value of 2.55 for the Toray TGP-H-120. For the SGL paper, the mean tortuosity values based on the LB and TS models were reported as 1.463 and 1.210 respectively. Again, the values from the LB approach closely agree with the value

reported in the literature. Using the porosity obtained experimentally through the immersion method, Cho and Mench [178] predicted the tortuosity based on the Macmullin number correlation and reported a tortuosity of 1.48 for the SGL 24AA paper. For the Freudenberg felt, the mean tortuosity values based on the LB and TS models were found to be 1.408 and 1.288 respectively. Once again, the values from the LB approach show very good agreement with the value reported in the literature. Totzke et al. [182] reported the tortuosity values of 1.50 for the Freudenberg H2315 felt using the synchrotron X-ray imaging and the skeletonisation algorithm.

As seen in Fig. 6.6, the mean values based on the TS model for both paper and felt samples are almost identical (1.277, 1.210 and 1.288 for the Toray paper, SGL paper and Freudenberg felt respectively). In contrast, the mean tortuosity values based on the LB model vary considerably from 1.408 to 2.123. This is possibly because the TS model for tortuosity relies only on the porosity value as the sole input parameter into the model. Therefore, the three samples which have somewhat similar porosity values (0.761-0.813) reveal almost identical tortuosity values. In addition, the TS model was originally developed for randomly oriented fibrous porous media in which all binder clusters are assumed to be fibre shaped. The LB model, on the other hand, treats all solid materials (carbon fibres and binding materials) as they truly appear. Hence, the LB model possibly provides a more realistic tortuosity value for GDLs. This explanation can reasonably be used to explain the considerable difference in the resulting tortuosity values between the LB and TS models observed in the Toray paper. As seen in Fig. 5.9, the Toray paper is more clustered than the other two samples. The clustering of carbon fibres and binding materials can contribute to the significant difference in the resulting tortuosity between that calculated based on the TS model and that based on the LB model, since the TS model assumes all clusters generated from the aggregation of fibres and binders as fibre shaped. In contrast, when using the LB approach, where the actual structure is considered, this clustering pattern possibly creates more resistance to gas flow contributing to higher tortuosity, as observed in the Toray paper.

Below, in Table 6.3, a comparison of mean permeability and tortuosity values of Toray paper, SGL paper and Freudenberg felt with respect to their effective thickness based on the TS model and the LB model, is presented.

Table 6.3 Comparison of mean permeability and tortuosity of Toray paper, SGL paper and Freudenberg felt based on the LB model and the TS model.

GDL	Thickness (μm)	Porosity	LB model		TS model	
			Permeability ($\times 10^{-12}$ m^2)	Tortuosity	Permeability ($\times 10^{-12}$ m^2)	Tortuosity
Toray	360	0.763	7.239	2.123	5.163	1.277
SGL	190	0.813	21.193	1.463	16.102	1.210
Freudenberg	222.5	0.761	6.693	1.408	12.881	1.288

6.7 Conclusions

In this chapter, we simulated gas flow through the X-ray reconstructed GDL samples using the single-phase LB model. The detailed gas velocity distribution at microscopic scale obtained from the LB simulation was then used to predict the through-plane permeability and tortuosity of each sample. The porosity, permeability and tortuosity values were compared with data available in the literature, as well as with the average permeability and tortuosity calculated based on the TS model obtained from Chapter 5.

The averaged through-plane permeability and tortuosity of each GDL sample showed close agreement with the values reported in the literature. By comparing the average values of each property based on the LB model and the TS model, it was found that the average values based on the LB model better agreed with the values reported in the literature. This can be attributed to the capability of the LB approach to incorporate the actual microscopic features of the GDLs into the model, such as the carbonised binder randomly distributed on the GDL fibres. This is in contrast to the TS model, which considers the GDL as a stack of purely straight fibres.

Chapter 7
Liquid Water Transport in Gas Diffusion Layers

7.1 Introduction

A GDL plays a crucial role in the overall performance of a PEMFC by providing pathways for reactant gases to be transported from a gas supply channel to a CL, and product water to be removed from the CL to the gas channel. Excessive presence of liquid water in the GDL hinders the access of reactant gases to the active sites of the catalyst layer leading to decreased performance of the PEMFC. Therefore, GDLs are usually treated with a hydrophobic agent to render their fibres more hydrophobic in order to facilitate gas transport and water removal. Numerous studies have been conducted to investigate water transport in the PEMFC in recent years; however, the behaviour of liquid water in the GDL at a pore-level is poorly understood. Experimental methods such as nuclear magnetic resonance (NMR) imaging, neutron imaging, X-ray imaging and direct optical visualization remain difficult to comprehend at a microscopic level because of the limit in spatial and temporal resolutions [13]. Litster et al. [75] employed a fluorescence microscopy technique together with optical photography to visualise through-plane liquid water in the GDL. From the same group, Bazylak et al. [59] examined the influence of compression on liquid water transport behaviour in GDL materials using the same technique, and found that compressed regions of the GDL provided preferential pathways for liquid water transport leading to breakthrough in the test apparatus. Their works show advancements in visualising liquid water behaviour; however, their technique allowed visualisation only at the upper layers of the GDL due to the opacity of the material.

Macroscopic models [10, 48, 187-191] have been developed and applied in order to predict the saturation distribution of liquid water. These models, however, which are based on the theory of volume averaging and assume that the GDL is a homogeneous material, fail to incorporate the influence of the pore morphology of the GDL on liquid water transport behaviour [85]. In addition, these models depend on empirical relationships of capillary pressure-saturation and relative permeability-saturation to

predict the behaviour of liquid water in the GDL. Capillary pressure is commonly expressed as a function of saturation via the Leverett function and, thus, likely entail higher inaccuracy levels, as it was originally derived based on experimental data of homogeneous soil or a sand bed with uniform wettability, which is significantly different from the actual GDL structural characteristics [4, 85, 192]. This poses major limitations in macroscopic models where a realistic detailed description of the liquid water transport process cannot be obtained.

Pore-scale models, such as pore network (PN) and Lattice Boltzmann (LB) models, have emerged as favourable models for simulating flow through porous media, as they can unveil the underlying influence of microscopic features on liquid water transport in the GDL at a pore-level. Several PN models have been developed to simulate water movement in 2D [25, 57, 98, 193, 194] and 3D pore networks [43, 89, 94-97, 195-198]. Using the PN approach, Sinha and Wang [43] modelled mixed-wettability GDL and found that liquid water preferentially flows through connected hydrophilic networks. Chapuis et al. [25] and Chraibi et al. [98] studied the impact of GDL wettability on water invasion in 2D network models and demonstrated the transition from stable displacement to capillary fingering with the change of wettability from hydrophilic to hydrophobic. Hinebaugh et al. [57] and Hinebaugh and Bazylak [94] modelled commercial GDLs based on the heterogeneous porosity distribution input obtained through X-ray tomography visualisation and suggested that GDLs should be designed to have smooth porosity distribution with few local minima. More recently, Lee et al. [97] extended the PN model to study liquid water transports in uniformly hydrophobic GDLs in contact with flow field plates having interconnected ribs and gas channel. Though the PN models can provide a microscopic insight of water transport and distribution in the GDL under various surface properties and boundary conditions, the PN models are still limited to creating simplified GDLs that may lead to inaccurate results. In the PN models, the complex structure of the actual GDL is commonly simplified to a regular sphere [198] or cubic pores [95] connected by columnar throats in the case of 3D pore networks, and to an array of randomly distributed equal-sized disks [25, 57] or an array of disks with random diameters [98] in the case of 2D pore networks.

Alternatively, the Lattice Boltzmann (LB) method has gathered interest as it is found to be particularly useful in fluid flow simulations in porous media due to its capability to incorporate complex boundaries of actual GDL structures as manufactured [19, 85]. To date, most studies on fluid transport in the GDL integrate artificial structures generated by stochastic simulation techniques to the LB models [42, 91, 122-124, 130-132, 199]. Mukherjee et al. [122] deployed the LB model to study two phase transport and flooding behaviour in the GDL and CL. Mukherjee et al. [123] have also used it to study the influence of compression on two phase transport and flooding behaviour. Mukherjee et al. [42] also examined the impact of durability on flooding behaviour by comparing the randomly distributed mixed wettability GDL with the purely hydrophobic GDL. Park and Li [125] used a 2D LB model to study two phase behaviour in a slice of a paper GDL, whilst Tabe et al. [126] also used a 2D model to discover liquid water invasion patterns. Niu et al. [124] considered the influence of pressure gradients and hydrophobicity by evaluating relative permeability and saturation relations. Hao and Cheng [29] investigated the effect of surface wettability by simulating liquid water invasion in a carbon paper GDL with uniform and non-uniform wettability. For the uniform wettability cases, their results indicated the decrease in saturation level of liquid water in the GDL with more hydrophobicity. For the non-uniform wettability case, the results indicated that water preferentially passed through the hydrophilic passages in the GDL. Chen et al. [128, 129] investigated the effects of channel land on liquid water behaviour and distribution in the 2D GDL and gas channel and found that a hydrophilic GC leads to less liquid water accumulation in the GDL than in the case of a hydrophobic GC. The microstructures were all reconstructed using stochastic simulation techniques. The stochastic method operates by using a set of structural inputs obtained from specifications or measured data to construct a porous medium [85, 122]; however, this method is not able to replicate fully an actual GDL sample. The stochastic technique also struggles to model the binding material that holds the fibres together in carbon paper. The binding material is either seen as a thin film (Fig. 5.1) or a rough surface (Fig. 5.2). Many modelling techniques ignore the binder but this is known to alter the pore size and shape. In addition, several assumptions have been made which make the stochastic model more unrealistic. For these reasons, more effort has been spent studying the GDL using X-ray computed tomography (XCT). Rama et al. [19] conducted a study on the feasibility of

using the combined methods of XCT and LB model to simulate fluid flow at the pore level in the GDL. The simulated result was then compared with the experimental result using a Frazier air tester and the error of the simulation study was found to be only 3% greater than the measured one. They concluded that the agreement between the two results indicated that the combination of XCT and LB model can capture accurately the microstructure of the GDL and the fluid flow through it. This, along with other studies [30, 31, 60, 69, 103-110] showed that using XCT to generate 3D microstructures provides great promise towards more realistic structural delineation and pore-scale modelling of the fluid transport in the GDLs.

Reviewing previous literature shows that GDLs have been heavily simulated using various techniques to discover a wide range of results. It is apparent that an increased number of studies have chosen to use XCT, LB method or both to simulate GDL properties and water transport. Considerable work has been conducted to show how water flow through the domain under various conditions. It is evident that not much work has been completed to examine the effect of wettability on water transport using fully modelled GDLs and LB method. Most of these works relied on either simplifying the 2D model [128, 129, 131, 132] of the GDL or a virtual stochastic model [29, 42, 122-124, 130, 199]. Chraibi et al. [98] explored the influence of wettability on water invasion patterns and saturation but used a very simple model. The model used was a 2D array of disk placed on a squared lattice. The disks represent the fibres in a GDL with random diameters and distribution. Recently, Rama and colleagues [30, 31] developed and applied the X-ray based LB method to model liquid water intrusion into a paper GDL. The works examined the influence of two different levels of wettability on water transport in a paper GDL with a finite thickness [30] and a full thickness GDL [31]. The results indicated a decrease in saturation in the hydrophobic case for any given intrusion pressure. Although the application of LB method has been increasingly employed to simulate liquid water transport in the GDL under various conditions, a comparison of liquid water transport behaviour in different GDL structures using the LB method is rare since only a single GDL material was utilised in most of these studies.

This study sets out to investigate the effects of GDL structure on liquid water transport behaviour including invasion patterns, saturation distribution and breakthrough

behaviour under varying wettability conditions by using the combination of LB method and XCT technique. The GDLs with paper and felt structures were reconstructed into 3D digital volumetric models via the XCT process. The digital models were then incorporated into a LB solver to model water saturation distribution through the GDL domains. The GDL wettability was also altered so that the effect on liquid water behaviour in the GDL could be examined. The wettability of a GDL sample is defined by the contact angle (θ) of liquid water with the solid surface of the GDL sample. Wettability is considered to be hydrophilic for $0°<\theta<90°$ and hydrophobic for $90°<\theta<180°$. The range $80°<\theta<100°$ is usually referred to as moderate or neutral or intermediate wettability. Illustration of different wetting conditions of the GDL has been shown in Fig. 1.5. In this study, the GDL samples were tested over the contact angles of 60°, 80°, 90°, 100°, 120° and 140° under applied pressure differences of 5kPa, 10kPa and 15kPa.

7.2 X-ray Reconstructed GDL Models

The GDL samples used in this study were Freudenberg H2315 felt, Toray TGP-H-120 paper and SGL 24AA paper. There was no PTFE and MPL applied on these samples. These share the following similarities: all are non-woven and composed of several layers of carbon fibres forming a carbon felt and a carbon paper. They differ, however, in the structural configuration of the fibres. The Freudenberg felt has curved fibres which travel in both through- and in-plane directions holding the structure together. The Toray and SGL papers have straight fibres, which travel mainly in the in-plane direction. The fibres of the paper-type are held together with a carbonized binder. The binders of the two papers, however, are different in their characteristics. The SGL binder is much rougher than that of the Toray paper. This rough binder spreads over the fibres of the sample lying in both in-plane and through-plane directions, as shown in Fig. 5.2. In contrast, the Toray paper has a smooth, sheet-like, binder which mainly aligns in the in-plane direction as shown in Fig. 5.1. Throughout the thesis, GDLs are referred to as Toray, SGL and Freudenberg respectively.

The reconstructed models of these GDL samples were acquired by the XCT. The details of the XCT process were described in Chapter 5. Fig. 7.1-Fig. 7.3 show the X-ray reconstruction of the GDL samples.

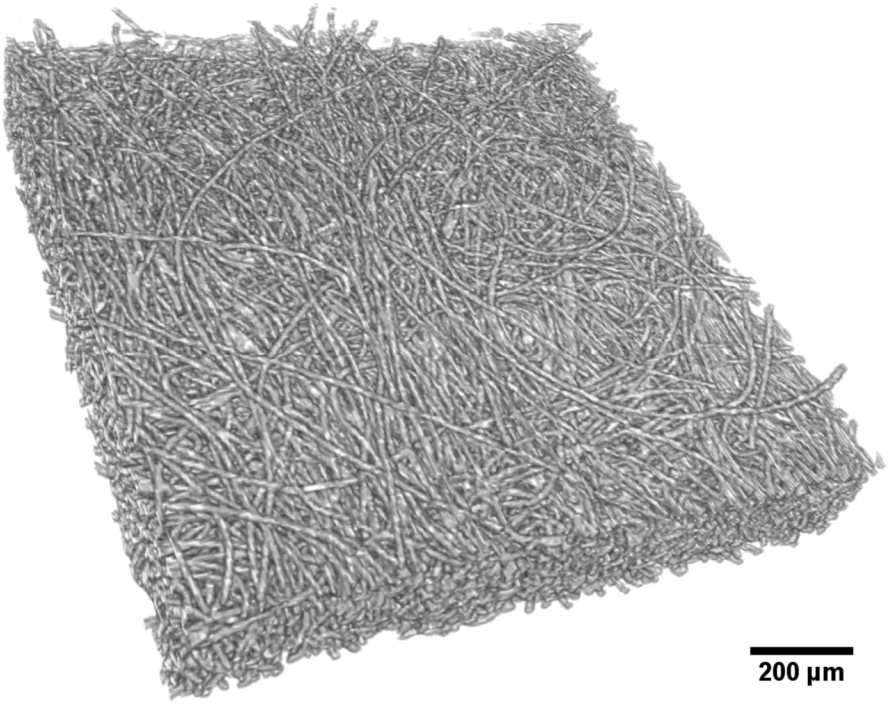

Figure 7.1 3D binary model of the Freudenberg felt GDL sample.

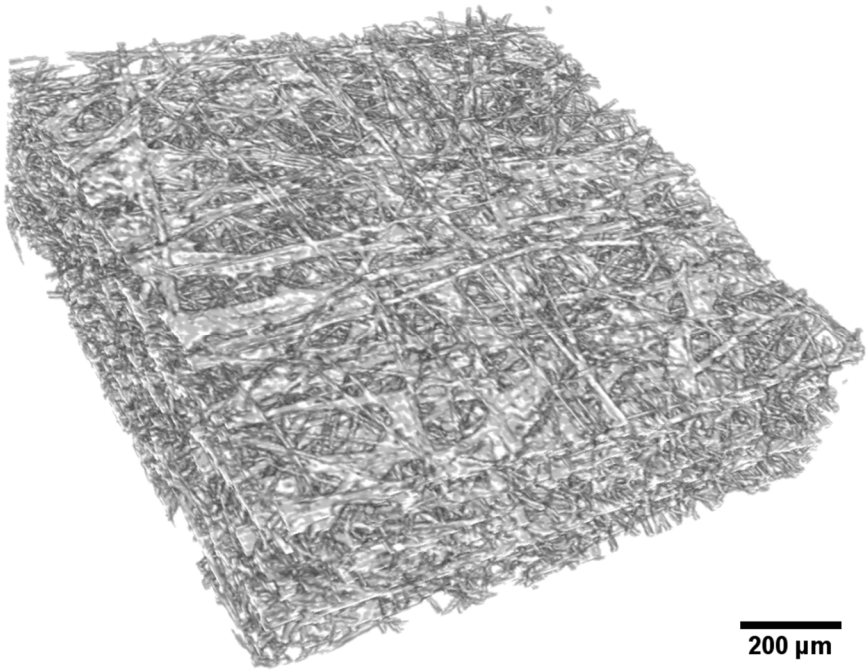

Figure 7.2 3D binary model of the Toray paper GDL sample.

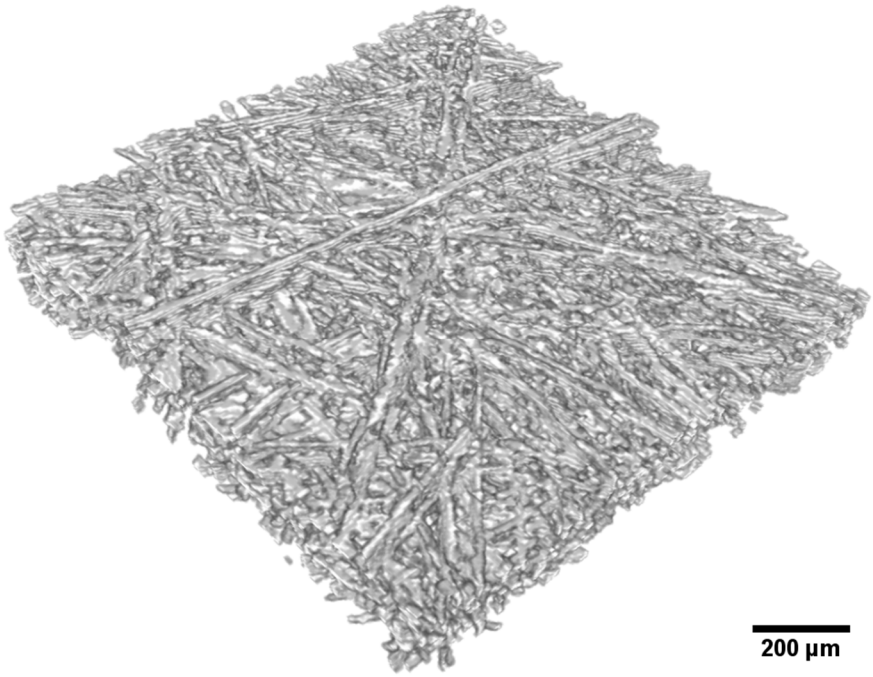

Figure 7.3 3D binary model of the SGL paper GDL sample.

7.3 Two-Phase Lattice Boltzmann Modelling

In multiple relaxation time (MRT) LB model, the evolution of fluid particle distribution functions for each fluid is described by the following equation [114]:

$$f_{i,k}\left(x+\xi_i\delta t, t+\delta t\right)=f_{i,k}\left(x,t\right)+\Omega^k\left[f_{i,k}^{eq}\left(x,t\right)-f_{i,k}\left(x,t\right)\right] \tag{7.1}$$

where $f_{i,k}\left(x,t\right)$ is the particle distribution function for fluid k at location x and time t, moving with velocity ξ_i in the ith direction, $f_{i,k}^{eq}\left(x,t\right)$ is the equilibrium distribution function for fluid k, which is the value of $f_{i,k}\left(x,t\right)$ at equilibrium state, δt is a time increment during which the particle travels from one location to another. The MRT LB model has been described in Chapter 2 (Section 2.5). In this study, the D3Q19 model was utilized and the lattice velocity ξ_i is defined as in Eq. (2.2). The equilibrium distribution functions for each fluid for the D3Q19 model are given by

$$f_{i,k}^{eq}=w_i\rho_k\left[1-\frac{3}{2}u_k^{eq}\cdot u_k^{eq}\right] \quad i=0,$$

$$f_{i,k}^{eq}=w_i\rho_k\left[1+3\xi_i\cdot u_k^{eq}+\frac{9}{2}\left(\xi_i\cdot u_k^{eq}\right)^2-\frac{3}{2}u_k^{eq}\cdot u_k^{eq}\right] \quad i=1,2,3,...,18, \tag{7.2}$$

where w_i is a weighting factor depending on the magnitude of the velocity ξ_i ($w_i=1/3$ for $\left|\xi_i\right|=0$, $w_i=1/18$ for $\left|\xi_i\right|=\delta x/\delta t$ and $w_i=1/36$ for $\left|\xi_i\right|=\sqrt{2}\delta x/\delta t$), c_s is the speed of sound and is given by $c_s=\frac{1}{\sqrt{3}}\delta x/\delta t$. The equilibrium velocity u_k^{eq} for fluid k is calculated by [114, 115]

$$\rho_k u_k^{eq}=\rho_k u'+\tau_k F_k \tag{7.3}$$

where u' is the bulk fluid velocity of the two fluids and is calculated by

$$u'=\frac{\sum_k \rho_k u_k/\tau_k}{\sum_k \rho_k/\tau_k} \tag{7.4}$$

where ρ_k is the macroscopic density of fluid k and is calculated by

$$\rho_k = \sum_{i=0}^{18} f_{i,k} \tag{7.5}$$

and u_k is the velocity of fluid k and is calculated by

$$\rho_k u_k = \sum_{i=0}^{18} \xi_i f_{i,k}(x,t) \tag{7.6}$$

The total force F_k acting on fluid k includes fluid-fluid interaction F_{f-f}^k and fluid-solid interaction F_{f-s}^k and is expressed as:

$$F_k = F_{f-f}^k + F_{f-s}^k \tag{7.7}$$

Fluid-fluid interaction force

In the SC model, for simplicity, only the interactions with the nearest-neighbouring sites are considered to define the inter-particle force. The fluid-fluid interaction force F_{f-f}^k on fluid k at location x is the sum of the forces between fluid k at x and fluid $\bar{k}$ at neighbouring sites x' and is given by [115]

$$F_{f-f}^k(x) = -\rho_k(x) \sum_{x'} \sum_{\bar{k}} G_{k\bar{k}}(x,x') \rho_{\bar{k}}(x')(x'-x) \tag{7.8}$$

where $G_{k\bar{k}}(x,x')$ is the Green's function representing the strength of the reaction between the two fluids. $G_{k\bar{k}}(x,x')$ is defined as zero for the same fluid component and different from zero for different fluid components. For the D3Q19 model, the Green's function $G_{k\bar{k}}(x,x')$ is calculated as follows:

$$G_{k\bar{k}}(x,x') = \begin{cases} g_{k\bar{k}}, & |x-x'| = 1, \\ g_{k\bar{k}}/2, & |x-x'| = \sqrt{2}, \\ 0, & otherwise \end{cases} \tag{7.9}$$

where $g_{k\bar{k}}$ is the interaction strength between fluid components k and $\bar{k}$. By choosing $g_{k\bar{k}}$ properly, fluid can separate automatically [30, 113, 200].

Fluid-solid interaction force

The interaction force between fluid k at location x and solid wall at location x' is given by [136]

$$F_{f-s}^{k}(x) = -\rho_k(x)\sum_{x'} G_{ks}(x,x')(x'-x) \tag{7.10}$$

At the fluid-solid interface, the solid is considered as a phase with constant density. In order to be consistent with the fluid-fluid interaction, the interaction parameter $G_{ks}(x,x')$ is given by

$$G_{ks}(x,x') = \begin{cases} g_{ks}, & |x-x'|=1, \\ g_{ks}/2, & |x-x'|=\sqrt{2}, \\ 0, & otherwise \end{cases} \tag{7.11}$$

where g_{ks} is the interaction strength between fluid k and the solid wall. g_{ks} defines the wall wettability. By altering g_{ks} for each fluid component, a desired contact angle θ between fluid-fluid interface and a wall can be obtained [113].

7.4 Model Validation

In a system consisting of water and air, such as the GDL in PEMFCs, the density ratio ρ_a/ρ_w and viscosity ratio μ_a/μ_w of the two fluids are 1:800 and 1:15 respectively, which is beyond the ability of the SC LB model since such a high density ratio could lead to numerical instability [30, 31]. To determine whether liquid water intrusion into the GDL can be simulated by this model, some non-dimensional numbers, including the Bond number, capillary number, Reynolds number and Weber number, were calculated. The Bond number $Bo = g(\rho_w - \rho_a)D^2/\sigma$ defines the ratio of gravitational force to interfacial force. The capillary number $Ca = \mu_w U_w/\sigma$ denotes the ratio of viscous force to interfacial force. The Reynolds number $\mathrm{Re} = \rho_w U_w D/\mu_w$ represents the ratio of inertial

force to viscous force. The Weber number $We = \rho_w U_w^2 D/\sigma$ denotes the ratio of inertial force to interfacial force. From the numbers above, D is the average pore diameter in the GDLs, g is the gravitational acceleration, U_w, ρ_w and μ_w are the velocity, density and viscosity of liquid water respectively, ρ_a and μ_a are the density and viscosity of air respectively, and σ is water-air interfacial tension. The average pore diameter in the GDLs is about 10 μm [30, 31]. In the GDL of an operating PEMFC, the approximated values of the three dimensionless numbers are as follows; 1.6×10^{-4} for the Bond number, 2.47×10^{-8} – 1.92×10^{-7} for the capillary number, 1.65×10^{-4} – 2.12×10^{-4} for the Reynolds number and 4.08×10^{-12} – 4.07×10^{-11} for the Weber number [31]. The value of the Bond number indicates that the effect of gravity is negligible with respect to the interfacial tension force. Likewise, the value of the capillary number shows that the viscous force is also negligible compared to the capillary force. The Reynolds number in this case reveals that the inertial force is negligible in comparison with the viscous force. Additionally, the value of the Weber number emphasises the effect of inertia and is insignificant with respect to the interfacial tension force. Accordingly, the large density and viscosity difference of air and water, which affect inertial, gravitational and viscous forces, appears to have a very limited effect on water transport in the GDL. Hence, it can be concluded that water intrusion into GDLs is primarily controlled by capillary action. Based on the above analysis, the comparable density and viscosity values of water and air are safely assumed in the SC LB model [30, 31].

The two-phase LB model also requires the two input parameters, the fluid-fluid interaction strength parameter $g_{k\bar{k}}$ and the fluid-solid interaction strength parameter g_{ks}, to be predetermined. $g_{k\bar{k}}$ characterises the fluid-fluid interfacial tension, whilst g_{ks} characterises the wettability of the solid wall. These two parameters, however, are not practically measurable. In order to determine the fluid-fluid interaction strength parameter $g_{k\bar{k}}$ and the fluid-solid interaction strength parameter g_{ks}, a series of numerical experiments were carried out in [30]. According to [30], the fluid-fluid interaction strength parameter $g_{k\bar{k}}$ was evaluated through a bubble test, and the fluid-solid interaction strength parameter g_{ks} was evaluated through a static droplet test. In the bubble test, the formation of bubbles with different diameters was simulated in a domain

consisting of 50×50×50 cubic voxels. All boundaries were treated as periodic boundaries. When the two fluids reached steady state, the pressure difference ΔP across the fluid-fluid interface was calculated based on Laplace's law as:

$$\Delta P = P_N - P_W = 2\sigma / R \tag{7.12}$$

where P_N is the pressure just outside the bubble, P_W is the pressure just inside the bubble, σ is the interfacial tension between the two fluids, and R is the radius of the bubble. In all simulations, the initial fluid densities were defined as $\rho_1 = 0$ and $\rho_2 = 1.0$ inside the bubble, and as $\rho_1 = 1.0$ and $\rho_2 = 0$ outside the bubble. The parameter $g_{k\bar{k}}$ was set to 0.001. Steady state was set to be achieved when the relative difference of the overall fluid velocity between two time steps was less than 10^{-6}. Simulations were carried out for several initial bubble diameters. The change of pressure difference across the surface of the bubble with respect to $2/R$ was examined and it was in agreement with Eq. (7.12) giving an interfacial tension of 0.18 in lattice unit.

In the droplet test, according to [30], the formation of a droplet on a solid wall was simulated with different values of the fluid-solid interaction strength parameter g_{ks}. Periodic boundaries were applied to other sides of the domain. Other parameters remained the same as in the bubble test. Once the two fluids reached steady state, the contact angle θ was evaluated from the final droplet radius R, droplet height H and the length of contact area between droplet and solid wall L as follows [31]:

$$\tan\theta = \frac{L}{2(R-H)} \tag{7.13}$$

The final radius R is calculated from H and L as [31]:

$$R = \frac{H}{2} + \frac{L^2}{8H} \tag{7.14}$$

Simulations were conducted using various g_{ks} values to obtain steady droplets with different contact angles. When $g_{ks} = 0$, the solid wall is neutral and the contact angle is 90°; when $g_{ks} > 0$, the solid wall is hydrophobic and the contact angle is greater

than 90°; and, when $g_{ks} < 0$ the solid wall is hydrophilic and the contact angle is less than 90° [30, 31].

7.5 Simulation and Boundary Setup

In this study, liquid water intrusion through the GDL samples was simulated by applying a pressure difference across the thickness of each GDL sample. To simulate water movement into the initially dry GDL, a water reservoir was added to the GDL structure at the front end and an air reservoir was added at the opposite end. The pressure difference was then imposed across these two ends in the through-plane direction to force liquid water to travel through the GDL domain. The prescribed pressures were imposed at the first layer of the water reservoir and the last layer of the air reservoir. The other four sides of the domain were treated as periodic boundaries in which any particle leaving the domain from one face with certain properties returns to the opposite face of the domain with the same properties. The bounce-back scheme for no-slip boundary conditions was used to solve the fluid-solid interface (i.e. solid wall) by assuming that any particle that hit a solid wall during the streaming step was simply bounced back to its original location. The three-dimensional model (D3Q19), containing 19 velocity directions, was utilised in this study. The D3Q19 scheme assumes that the particles at each node can travel in 19 velocity directions in the three-dimensional lattice regime. In this study, the isothermal condition is assumed.

The GDL samples used in this study are the Freudenberg H2315 felt, Toray TGP-H-120 paper and SGL 24AA paper. They were acquired by X-ray tomography at a resolution of 2.5 μm/pixel. Due to the limitations of computational power, only a small portion of each GDL sample was chosen for simulations. The reconstructed domain of each sample is shown in Fig. 7.4-Fig. 7.6. The digital and physical size of each sample domain is shown in Table 7.1.

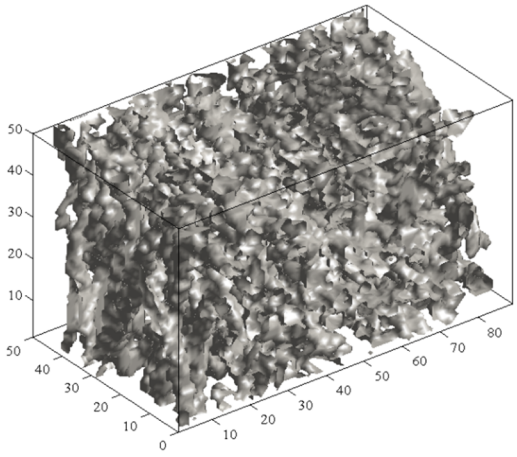

Figure 7.4 Freudenberg felt simulated domain.

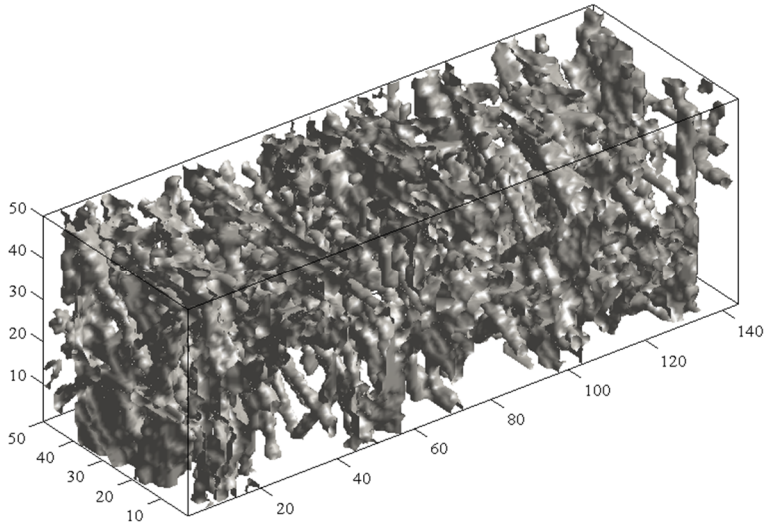

Figure 7.5 Toray paper simulated domain.

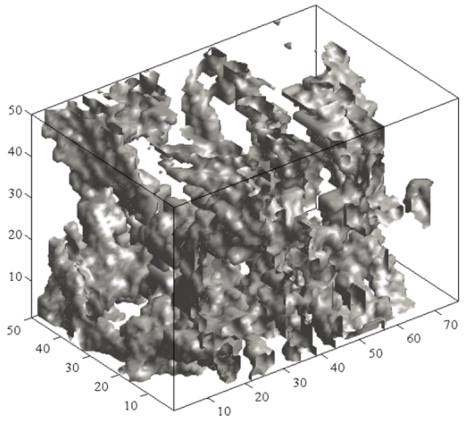

Figure 7.6 SGL paper simulated domain.

Table 7.1 Digital and physical sizes of each sample domain.

Sample	Freudenberg H2315	Toray TGP-H-120	SGL 24AA
Resolution (μm/pixel)	2.5	2.5	2.5
Digital size (pixel^3)	50x50x89	50x50x144	50x50x76
Physical size (μm^3)	125x125x222.5	125x125x360	125x125x190

In this study, the three GDL samples were tested over the contact angles of 60°, 80°, 90°, 100°, 120° and 140° under applied pressure differences of 5kPa, 10kPa and 15kPa. By varying the contact angle and pressure difference, comparisons can be drawn on the effects they have on liquid water behaviour in each GDL sample. The simulations were run until water broke through the outlet or it was clear that the water was not going to invade any further into the GDL structures.

7.6 Results and Discussion

In this study, the effects of GDL structures on liquid water transport behaviour, including invasion patterns, saturation distribution and breakthrough behaviour, under varying

wettability conditions and applied pressures were examined by using a combination of the LB method and XCT technique. The simulated domain of the Freudenberg felt, Toray paper and SGL paper (Fig. 7.4-Fig. 7.6) were integrated into a two-phase LB solver developed by the University of Liverpool. Each sample was tested over the contact angles of 60°, 80°, 90°, 100°, 120° and 140° under applied pressure differences of 5kPa, 10kPa and 15kPa.

7.6.1 Invasion Pattern

Fig. 7.7-Fig. 7.15 show water intrusion into the GDL samples (Freudenberg felt, Toray paper and SGL paper) at varying stages of simulation time. The first figure in each row shows the beginning stage of intrusion whilst the third figure displays the stage at which water has broken through or stopped its invasion into the sample.

Effects of GDL Wettability

The invasion figures of the three GDL samples (Fig. 7.7-Fig. 7.15) indicate that wettability has a significant effect on the invasion pattern of liquid water through the tested samples. They show the change of invasion pattern as the wettability, represented by contact angle, changes from hydrophilic to hydrophobic. For the hydrophilic contact angles, the water displaces air in a uniform manner with homogeneous invasion. It proceeds through the sample saturating all the pores as it travels with a flat invasion front. For the moderate contact angles, the same invasion pattern occurs and the water moves forward with nearly flat front saturating the sample as it moves. At the hydrophilic and moderate angles, the capillary resistance force for liquid water invasion in the GDL sample depends little on pore size. Thus, it is relatively easy for water to fill the pores, either small or large, resulting in a homogeneous invasion. This phenomenon is known as stable displacement. The Freudenberg felt, Toray paper and SGL paper at hydrophilic contact angles present the same pattern of invasion. Water enters the GDL domain at the interface between water reservoir and the GDL and then travels along the sample thickness with stable displacement. It occupies almost all pores in a cross section then proceeds to the next cross section until reaching the sample outlet (i.e. the interface between the GDL and air reservoir) for the Freudenberg felt and SGL paper or until stopping its invasion (at about 70% of the sample thickness) for the Toray paper. This

phenomenon is similar to the simulation result in [29] in which liquid water travelled with a stable displacement in a stochastic reconstructed GDL with the contact angle of 92°.

For the hydrophobic contact angles, on the other hand, the water no longer moves with a flat front. Instead, the water passes through the sample but partially saturates the domain by occupying certain void spaces in the porous network of the GDL sample. This phenomenon is known as capillary fingering. Capillary fingering appears because of the variance in pore size and the resulting capillary resistance forces. A large pore requires less effort for liquid water to flow through it than a small pore. For smaller pores, the pressure required to move water down the pore throat will be too great, so no flow will occur at those small pores. Accordingly, liquid water preferentially chooses the largest pores to invade on its advancing path as larger hydrophobic pores create smaller resistance force. The capillary fingering observed in hydrophobic GDLs agrees with the results reported in [29, 31, 122, 129].

It is observed that the transition between stable displacement and capillary fingering is not a gradual process but occurs very abruptly. For hydrophilic contact angles ($60°<\theta<90°$), water travels with a flat invasion front saturating all pores. For hydrophobic contact angles ($100°<\theta<140°$), however, the water moves with capillary fingering. The results indicate that the transition between the two phenomena does not occur at the moderate contact angle of 90°, as shown in the work of Chraibi et al. [98]. Chraibi et al. demonstrated that there was a transition between 80° and 100°. However, the technique used to simulate a porous media did not replicate a real GDL. This study shows that the transition occurs in the region of $100°<\theta<120°$ for the Freudenberg felt and Toray paper and the region of $90°<\theta<100°$ for the SGL paper. Without further work and simulations at smaller increments of contact angle the precise angle cannot be confirmed**.**

Effects of GDL Structure

The Freudenberg felt, Toray paper and SGL paper all show capillary fingering at hydrophobic contact angles. Water travels through the sample with capillary fingering; however, it exhibits different natured capillary fingering for each sample. For the Freudenberg felt, liquid water entering the GDL forms convex water fronts due to hydrophobicity of the GDL. As more water enters the inlet of the sample domain, several

water fronts start penetrating into the domain showing a finger-like invasion. As observed, water selects some pathways to travel through the domain depending on the local capillary resistance force, although mainly in the through-plane direction (thickness direction). At 120° and 140°, a similar invasion pattern is observed; however, water shows smaller fingering fronts for the 140° case. This suggests the influence of the degree of hydrophobicity on water invasion characteristics. Unlike the Freudenberg felt, invasion of liquid water in the in-plane direction is clearly seen in the Toray paper. Water enters the domain and then selectively travels through large pores in the through-plane direction. Interestingly, at certain cross sections (at about 35% and 70% of the thickness) water invades the in-plane direction and appears to occupy all pores at that cross section. This brings attention to the difference in structure of the two types of GDLs, paper and felt. Based on the structure analysis in Chapter 5, it was found that the Toray paper has a much larger variation in porosity along the thickness of the sample. The porosity variation exhibits as peaks and troughs with a peak-to-trough difference of about 11% (Fig. 5.13(a)). This agrees with the visual inspection of the Toray paper structure. From visual analysis, the large area which lacks fibres can be easily distinguished from the areas which are much more densely populated with carbon fibre strands and a binding material. The high porosity area lacking of fibres creates a bulk void volume which acts as a large pore. Since water preferentially chooses the largest pore to invade in a hydrophobic domain, it tends to travel in the in-plane direction where larger void space is present, than in the through-plane direction where the dense fibres and binding material create much smaller pores which are more difficult to pass through. The Freudenberg felt, on the other hand, has a much more consistent structure in the thickness direction. As a result, there is less variation in porosity distribution along the sample thickness with only about 4.7% variation in the core region, as shown in Fig. 5.13(c) in Chapter 5. Thus, water in the Freudenberg felt travels in any direction, either through-plane or in-plane depending on the local capillary resistance force. In this study, however, the results suggested that water favourably travels in the through-plane direction of the felt sample. For the SGL paper, water travels through the sample with capillary fingering at hydrophobic angles, similar to the other samples. As the liquid water front moves further in the thickness direction, water also invades the SGL sample in the in-plane direction but does not fully saturate the cross section as observed in the Toray sample. Instead, water

travelling in the SGL sample shows an increase in water-occupied pore space in certain cross sections but not full saturation. Interestingly, water entering the SGL domain forms a more convex, sphere-like shaped, invasion front than those of the Freudenberg felt and Toray paper. This sphere-like invasion front is primarily due to the combined effect of strong wall adhesion forces from the interaction with highly hydrophobic fibres/binder and the structure of the sample. This indicates the strong influence of structure on the capillary fingering invasion of liquid water in hydrophobic GDL.

Effects of Applied Pressure Difference

This study compared the intrusion pattern of liquid water under applied pressure difference of 5kPa, 10kPa and 15kPa. Considering the three pressure differences, it is observed that the difference in pressure shows no effect on the intrusion pattern of liquid water. The Freudenberg felt, Toray paper and SGL paper present the same trend under varying pressure differences applied across the sample thickness. For all pressure differences, a stable displacement is observed in hydrophilic and moderate contact angles and a capillary fingering is observed in hydrophobic contact angles. The only exception is that the intrusion pattern at 5kPa of the Freudenberg felt displays a stable displacement for all contact angles. This is again due to the effect of surface wettability and resulting capillary resistance forces in which the high hydrophobic angles (120° and 140°) create high capillary resistance; thus, even higher applied pressure difference is required to overcome this capillary resistance. At 120° and 140° with 5kPa, it seems that the pressure difference was not sufficiently great to force water to move forward and make a significant intrusion distance to exhibit an obvious intrusion pattern. As observed, water travels only a very short distance then stops at about 10% of the sample thickness. It can be assumed that an increase in pressure difference above 5kPa would allow capillary fingering to present its characteristics at hydrophobic angles.

It is clear that wettability has a significant impact on water invasion patterns through the GDL samples. It governs the change of invasion pattern from stable displacement to capillary fingering with the switch of contact angle from hydrophilic to hydrophobic. As regards applied pressure, on the other hand, it is found that the difference in applied pressure across the sample thickness does not affect the invasion pattern of liquid water in the GDL sample. However, applied pressure difference is found

to control the invasion distance of liquid water and thus breakthrough occurrence. In addition, the structure of the GDL sample is found to influence the nature of capillary fingering invasion of liquid water in the hydrophobic domain but has no effect on invasion patterns in hydrophilic domains.

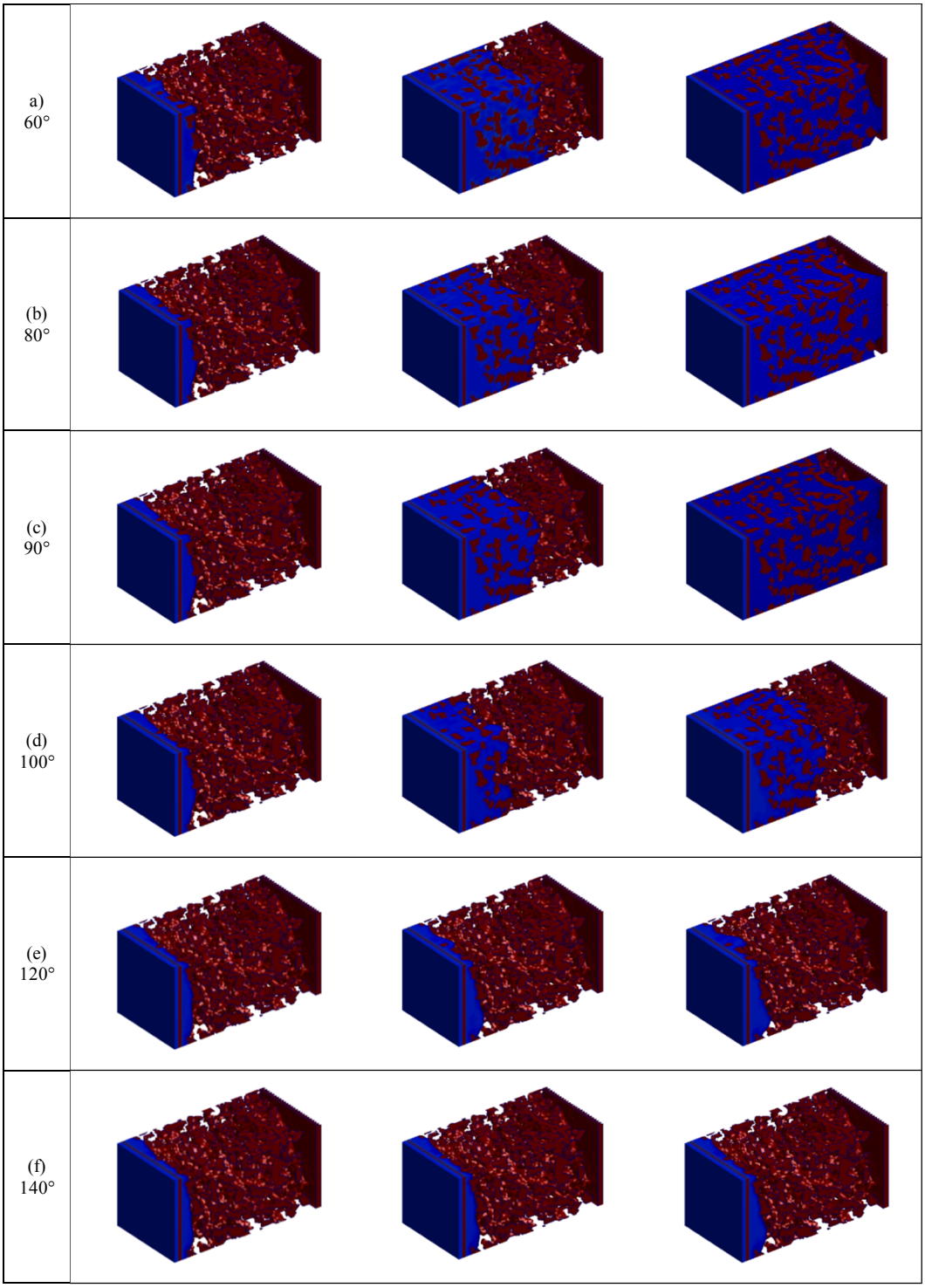

Figure 7.7 Freudenberg felt intrusion patterns at contact angle of a) 60° b) 80° c) 90° d) 100° e) 120° f) 140° under 5kPa pressure difference.

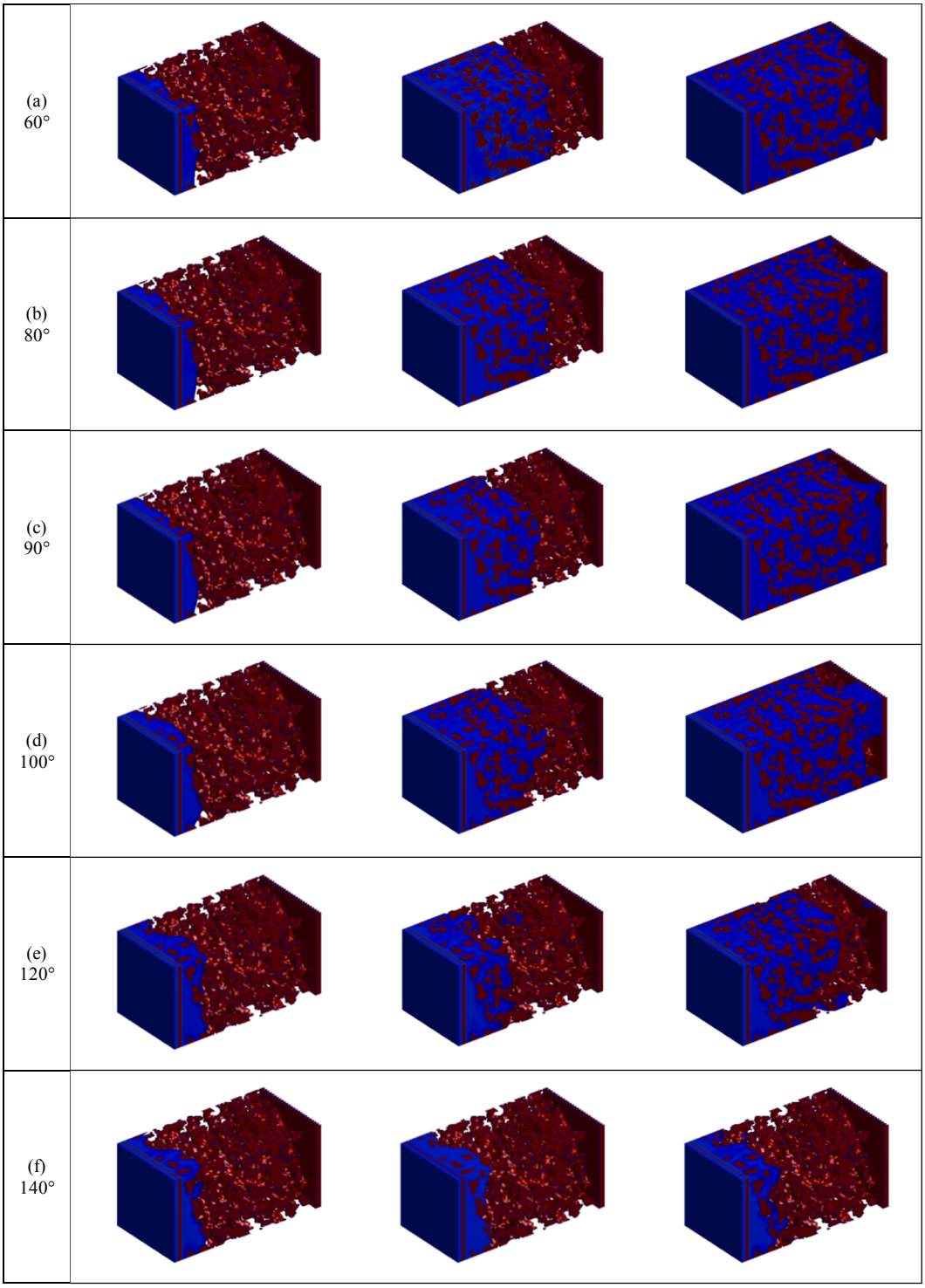

Figure 7.8 Freudenberg felt intrusion patterns at contact angle of a) 60° b) 80° c) 90° d) 100° e) 120° f) 140° under 10kPa pressure difference.

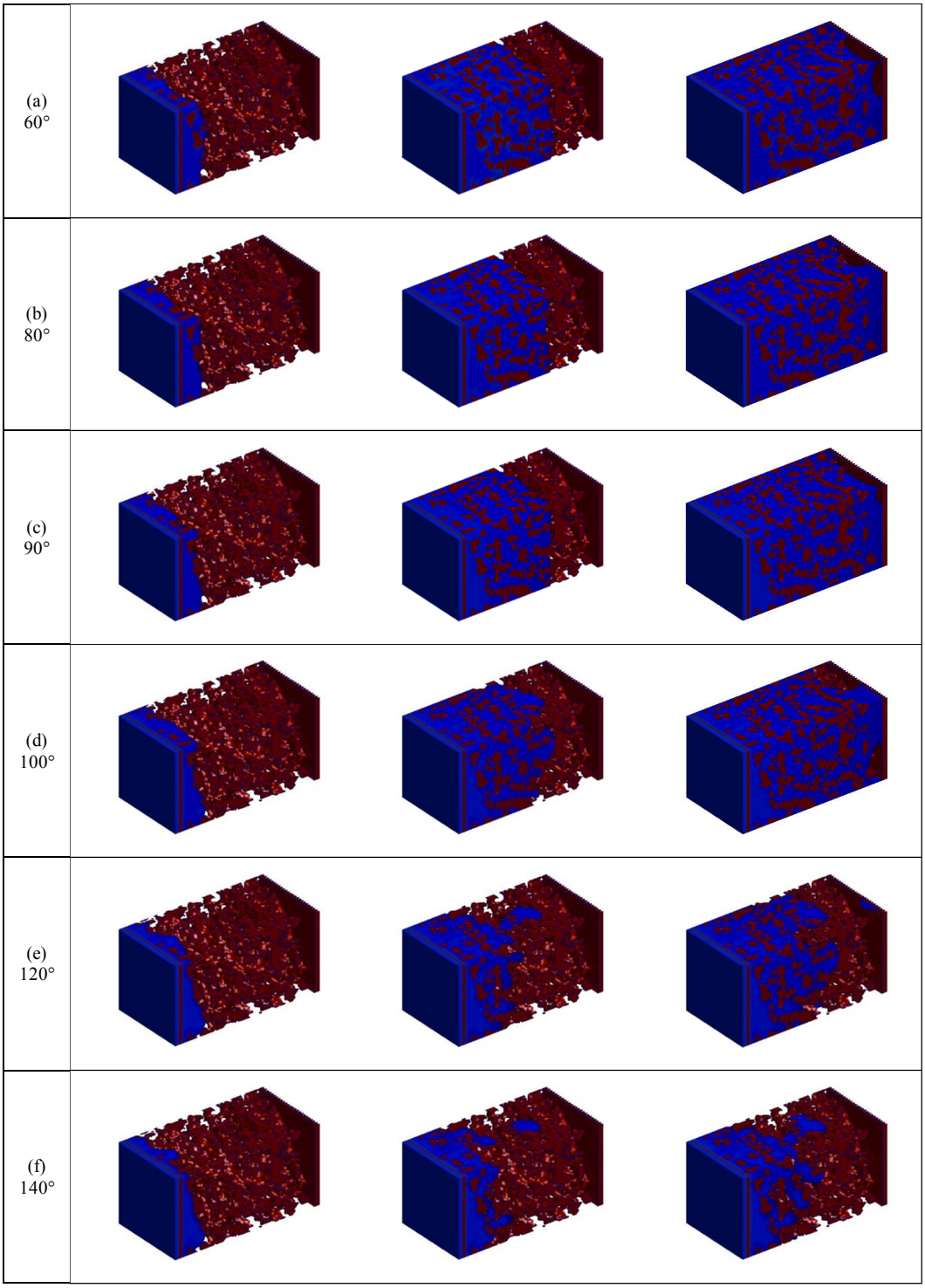

Figure 7.9 Freudenberg felt intrusion patterns at contact angle of a) 60° b) 80° c) 90° d) 100° e) 120° f) 140° under 15kPa pressure difference.

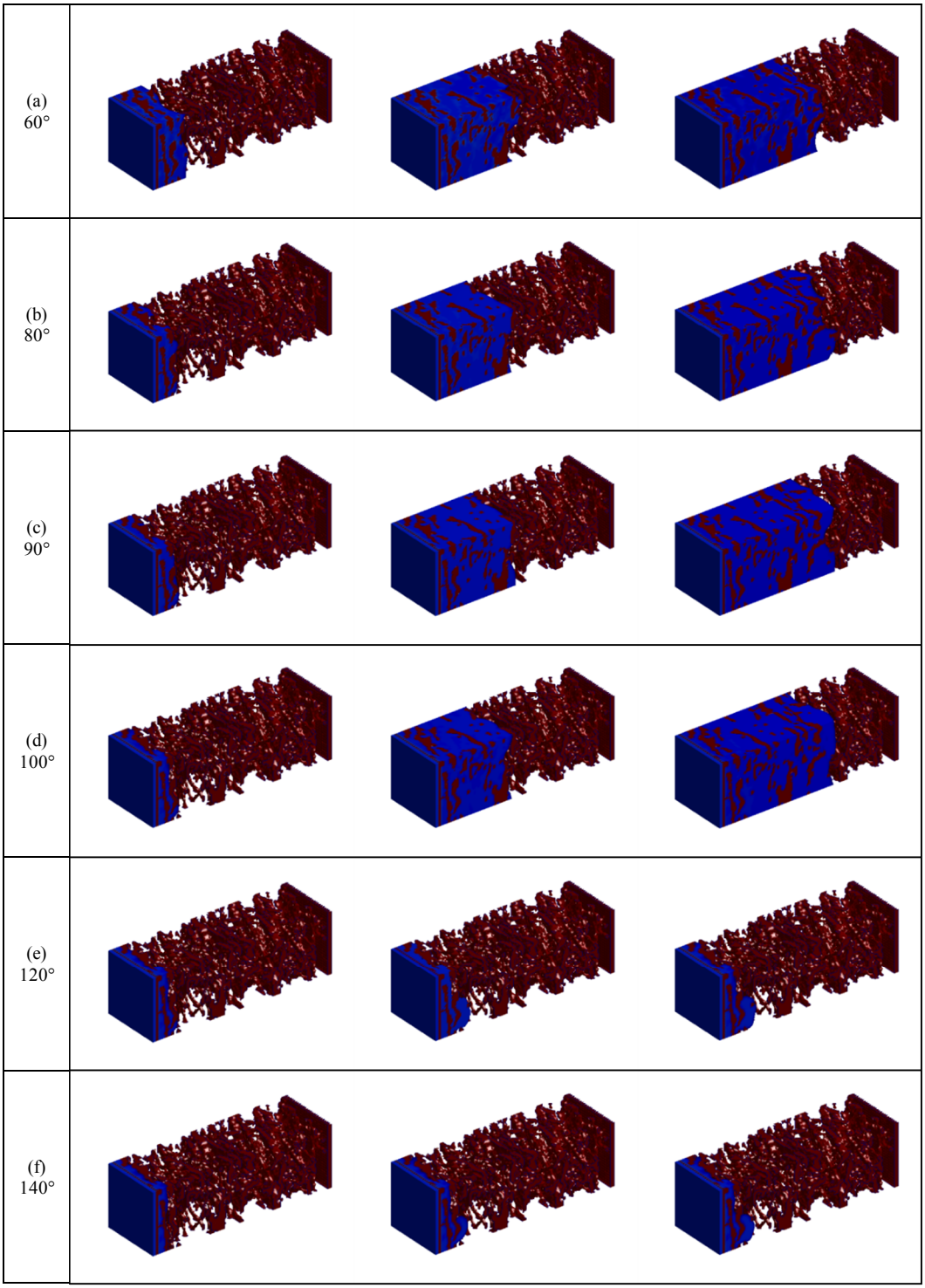

Figure 7.10 Toray paper intrusion patterns at contact angle of a) 60° b) 80° c) 90° d) 100° e) 120° f) 140° under 5kPa pressure difference.

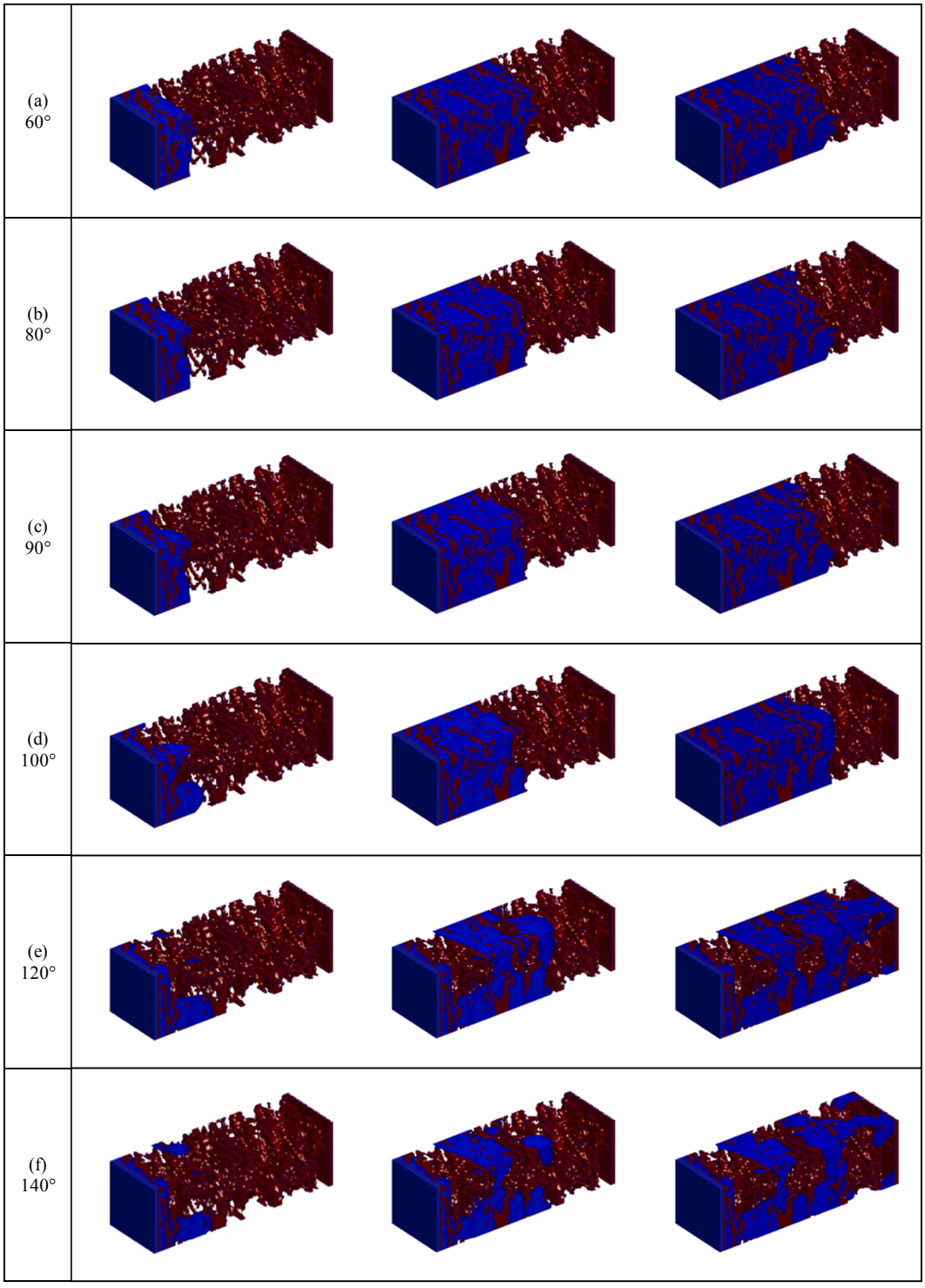

Figure 7.11 Toray paper intrusion patterns at contact angle of a) 60° b) 80° c) 90° d) 100° e) 120° f) 140° under 10kPa pressure difference.

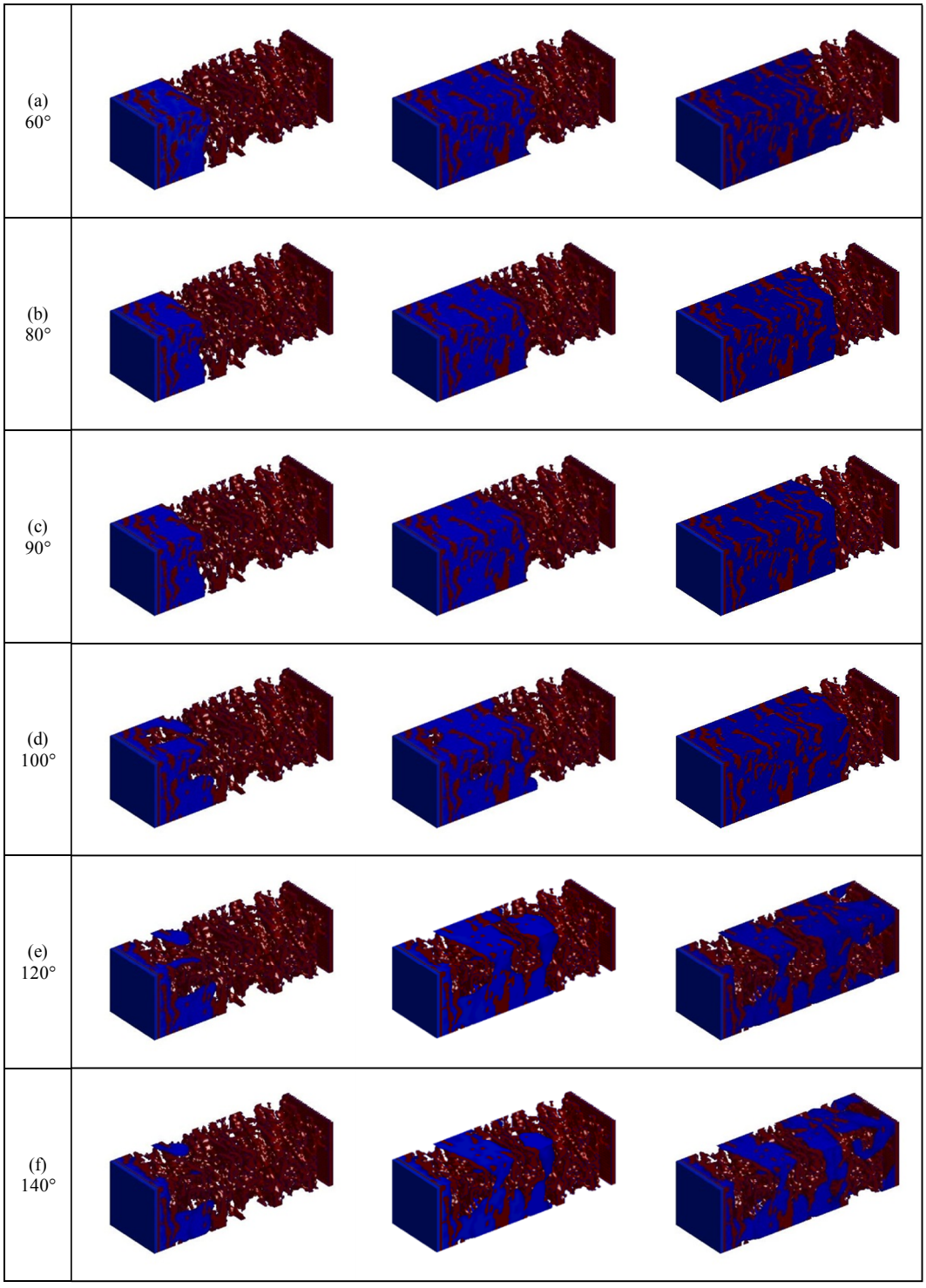

Figure 7.12 Toray paper intrusion patterns at contact angle of a) 60° b) 80° c) 90° d) 100° e) 120° f) 140° under 15kPa pressure difference.

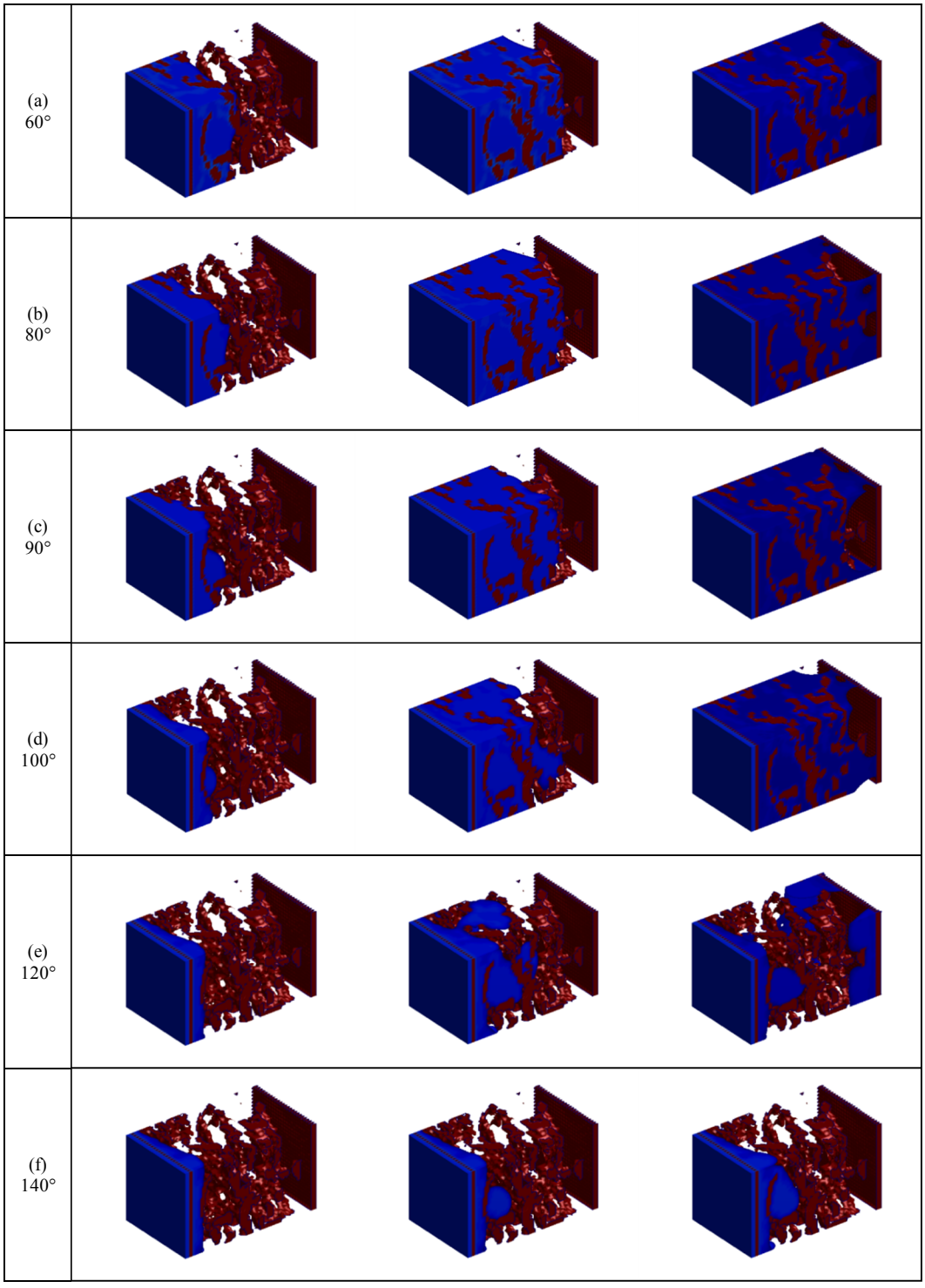

Figure 7.13 SGL paper intrusion patterns at contact angle of a) 60° b) 80° c) 90° d) 100° e) 120° f) 140° under 5kPa pressure difference.

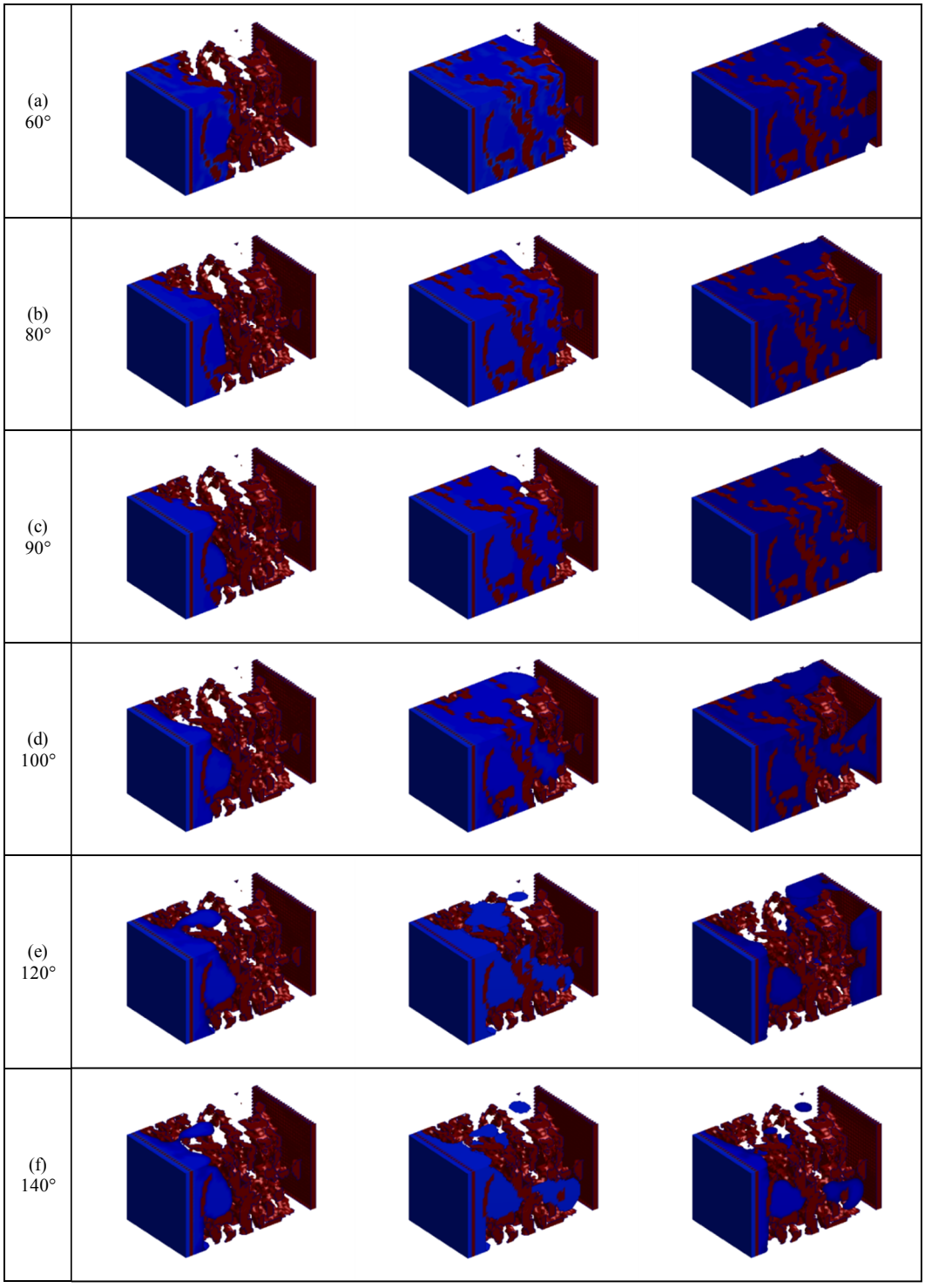

Figure 7.14 SGL paper intrusion patterns at contact angle of a) 60° b) 80° c) 90° d) 100° e) 120° f) 140° under 10kPa pressure difference.

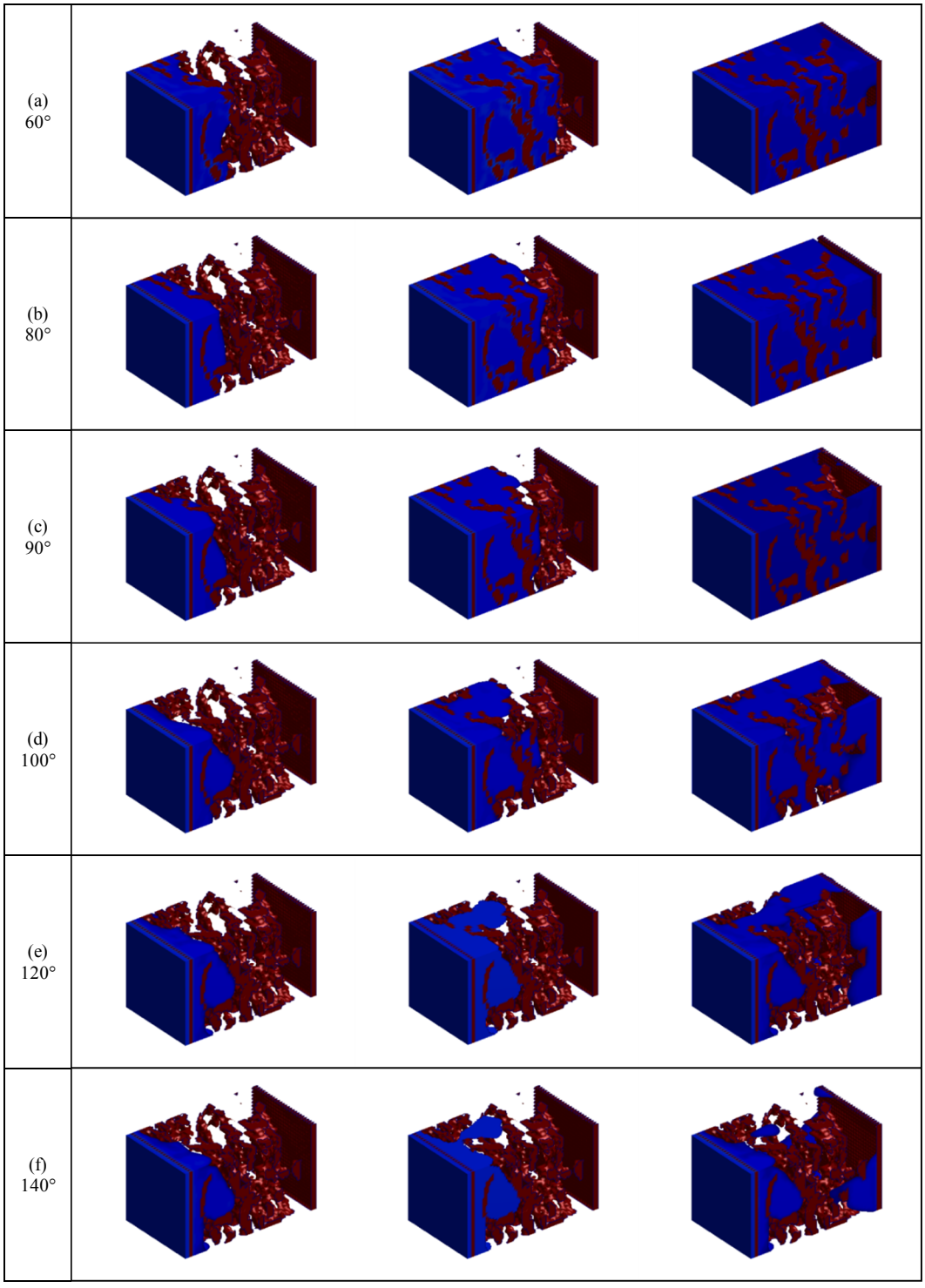

Figure 7.15 SGL paper intrusion patterns at contact angle of a) 60° b) 80° c) 90° d) 100° e) 120° f) 140° under 15kPa pressure difference.

7.6.2 Water Saturation Distribution

Fig. 7.16-Fig. 7.24 are graphical representations of the liquid water evolution through the GDL structures. They offer the average cross sectional saturation levels along the through-plane direction (thickness direction) of the GDL samples at chosen time steps. The average cross sectional saturation is defined as the ratio of the area occupied by liquid water to the total void area in the cross section. Hence, saturation is noted in the range of zero to one, where zero is no water saturation and one is full saturation. The simulations were run until water broke through the outlet or it was clear that the water was not going to invade any further into the GDL structures.

The saturation figures (Fig. 7.16-Fig. 7.24) confirm what was observed in the intrusion figures (Fig. 7.7-Fig. 7.15). They show the evolution of the saturation profile along the GDL thickness and demonstrate the change of intrusion pattern from stable displacement to capillary fingering as the wettability changes from hydrophilic to hydrophobic. The stable displacement is characterised by somewhat flat saturation front profiles, which indicate water occupying almost all void spaces in the cross section of the sample thickness. On the other hand, the more complex saturation profile with concave shapes corresponds to capillary fingering invasion in which water invades only certain pores partially saturating the void area in the cross section. Hence, the average saturation level in each cross section of the capillary fingering profile is usually lower than that of the stable displacement profile.

GDL with Felt Structure

For the Freudenberg felt sample at 5kPa, all contact angles display a stable displacement saturation profile. At 5kPa, it is observed that the intrusion distance of liquid water decreases with an increasing contact angle from hydrophilic to hydrophobic. Water passes through the sample thickness in all hydrophilic and moderate angles (up until 90°). With an increasing contact angle, however, it is shown that a longer time period is needed for breakthrough, from 98.96ms at 60° to 203.13ms at 90°. From the contact angle of 100° upwards, water does not pass through the domain. At 100° angle, the intrusion distance increases consistently with time, but it shows a very small increase at 416.67ms where the intrusion distance is at about 60% of the sample thickness and then stops. For

the 120° and 140° case, invasion stops at about 15-20% of the sample thickness. The 10kPa case displays a stable displacement front and breakthrough at hydrophilic and moderate contact angles up until 100° in this case. For the hydrophobic contact angle of 120°, water passes through the sample thickness with capillary fingering in which a significant drop in saturation is observed, as seen in Fig. 7.17. At 140°, water travels with capillary fingering but stops its invasion at about 40% of the sample thickness which is about 20% further in intrusion distance than that of the 5kPa. This suggests the effect that applied pressure difference has on intrusion distance. Again, it is seen that the breakthrough time increases with increasing contact angles, from 62.50ms at 60° to 359.38ms at 120° contact angle. The 15kPa pressure difference shows a very similar trend to the 10kPa, with the only difference being that water passes through the sample thickness at all contact angles. The saturation figures show stable displacement profiles for the hydrophilic and moderate contact angles up until 100° and capillary fingering for the hydrophobic contact angles of 120° and 140°. Again, the breakthrough time increases with increasing contact angles, from 41.67ms at 60° to 109.38ms at 140°. Comparing the breakthrough time of the 15kPa case with that of the 5kPa and 10kPa cases, it can be seen that breakthrough time decreases as the applied pressure difference increases.

GDLs with Paper Structure

For the Toray paper at 5kPa, the saturation profiles display a stable displacement front at hydrophilic and moderate contact angles (up until 100°) and a capillary fingering front at hydrophobic contact angles (120° and 140°). At 5kPa, it is seen that water does not break through the sample outlet at any contact angles. Up until 100° at 5kPa, water passes through about 60-70% of the sample thickness and then stops, while at 120° and 140° the intrusion stops at a much shorter distance of about 15-20% of the sample thickness. Interestingly, at 100° with 5kPa, a stable displacement is observed but small pockets of air are not displaced by liquid water at 208.33ms and 416.67ms. These pockets of air are soon filled by liquid water in the following time steps; however, this is possibly a very early stage of capillary fingering. The 10kPa and 15kPa cases exhibit the same trend. Up until the contact angle of 100°, stable displacement is shown and again intrusion only extends about 70% into the sample thickness, similar to the 5kPa case. As with the 5kPa case, the transition between stable displacement and capillary fingering seems to be at

100° for the 10kPa and 15kPa cases. At 10kPa with 100°, the profiles present a significant decrease in saturation in the cross sections at 31.25ms and 62.50ms, showing up to 20% of void spaces in the cross section not being occupied before water rises again at 125.00ms and saturates all pores. At 15kPa with 100°, though a stable displacement with a flat front profile is observed, small pockets of void areas are not displaced by liquid water until 250ms. This is again possibly a very early stage of capillary fingering. For the contact angle beyond 100°, capillary fingering is observed in which large void spaces are not filled by liquid water. At 120° and 140° with 10kPa and 15kPa, it is seen that water saturation levels drop sharply and then rise again, fully saturating the cross sections of the sample. This appears as peaks and troughs in which saturation drops to below 20%. Further down the sample thickness, however, the cross section is fully saturated, as seen in Fig. 7.20 and Fig. 7.21. This characteristic at 120° and 140° with 10kPa and 15kPa differs from that of the Freudenberg felt sample. For the Freudenberg felt, once the saturation levels start to fall, they never rise to saturate fully a cross section. Some regions show a small increase in saturation but this reduces as the water moves further into the sample thickness, as seen in Fig. 7.17 and Fig. 7.18. This variance again would bring attention to the difference in structure of the two samples. Hinebaugh et al. [94] modelled the pore structure and predicted water saturation of GDLs using the PN model. Their work demonstrates that the peaks and valleys in the porosity profiles of thick carbon papers generate highly saturated regions in the GDL, with low porosity regions corresponding to high saturation regions. This would explain the peaks and troughs seen in Fig. 7.20 and Fig. 7.21. There are regions of low and high porosity across the GDL structure creating high and low saturated regions.

Considering pressure differences applied across the Toray paper, it is seen that an increase in pressure difference does not seem to affect the saturation profile for all contact angles. However, an increase in pressure difference forces the water to pass through the hydrophobic domains in decreased time.

Unlike the Freudenberg felt in which breakthrough time increases with an increasing contact angle, the Toray paper at 10kPa and 15kPa displays an opposite trend. Breakthrough time decreases from 229.17ms at 120° to 182.29ms at 140° for the 10kPa case and from 98.96ms to 93.75ms for the 15kPa case. Again, it is seen that an increase in

applied pressure difference, from 10kPa to 15kPa, significantly decreases breakthrough time, from 229.17ms to just 98.96ms for the 120° case and 182.29ms to 93.75ms for the 140° case, which is about 50% for both cases.

As regards the SGL paper, its general trend is more similar to the Freudenberg felt than its paper counterpart. At 5kPa, a stable displacement is observed at all hydrophilic contact angles, whereas a capillary fingering is observed at all hydrophobic contact angles. At 100°, its invasion pattern seems to shift from stable displacement to capillary fingering, as seen in Fig. 7.22 where a sudden drop in saturation at 156.25ms is clearly observed. Interestingly, the saturation level soon regains to saturate fully the cross section as time moves on and the profile becomes stable and flat-fronted again. By analysing the invasion figure (Fig. 7.13), however, it is obvious that the transition is at about 100° since the fingering is clearly observed in Fig. 7.13(d) showing an existence of unoccupied void spaces. Up until the contact angle of 120° at 5kPa, water consistently passes through the domain showing an increase in breakthrough time with increasing contact angles from 104.17ms at 60° to 291.67ms at 120°. At 140°, water does not exit the domain as it stops its invasion at about 40% of the sample thickness. This suggests the effect of contact angle (i.e. surface wettability) on breakthrough, as higher contact angles create greater capillary resistance and subsequently prohibit water to pass through the sample thickness. The 10kPa and 15kPa cases present a very similar trend. In general, water breaks through with stable displacement for hydrophilic and moderate contact angles, and with capillary fingering for hydrophobic contact angles (from 100° onwards). Similar to the 5kPa case, the transition between stable displacement and capillary fingering occurs at the region of 90° to 100° for both 10kPa and 15kPa cases. The saturation figures also display an increase in breakthrough time with increasing hydrophilic contact angles. Breakthrough time increases from 62.50ms at 60° to 72.92ms at 90° for the 10kPa case and from 41.67ms at 60° to 46.88ms at 90° for the 15kPa case. On the other hand, breakthrough time in the hydrophobic region decreases with increasing contact angle from 78.13ms at 100° to 52.08ms at 140° for the 10kPa case and from 36.46ms at 100° to 26.04ms at 140° for the 15kPa case. The phenomenon of the decreasing breakthrough time is similar to what was seen in the Toray paper at 10kPa and 15kPa. As with the Freudenberg and Toray samples, again, it is observed that an increase in applied pressure difference substantially decreases breakthrough time. For example, at

120° breakthrough time decreases from 291.67ms at 5kPa to just 62.50ms at 10kPa, and to only 31.25ms at 15kPa.

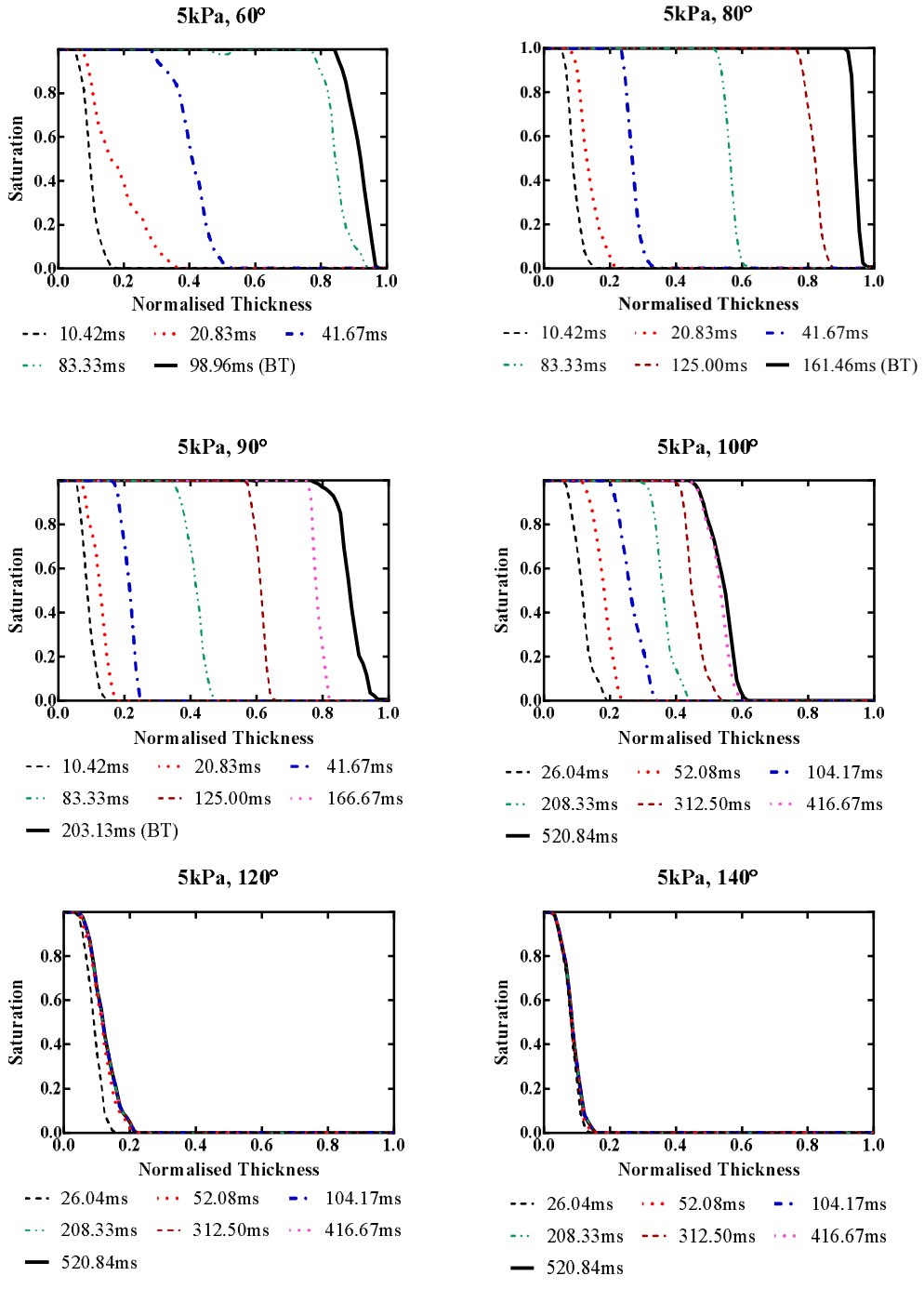

Figure 7.16 Water distributions across the thickness of the Freudenberg felt at the applied pressure difference of 5kPa.

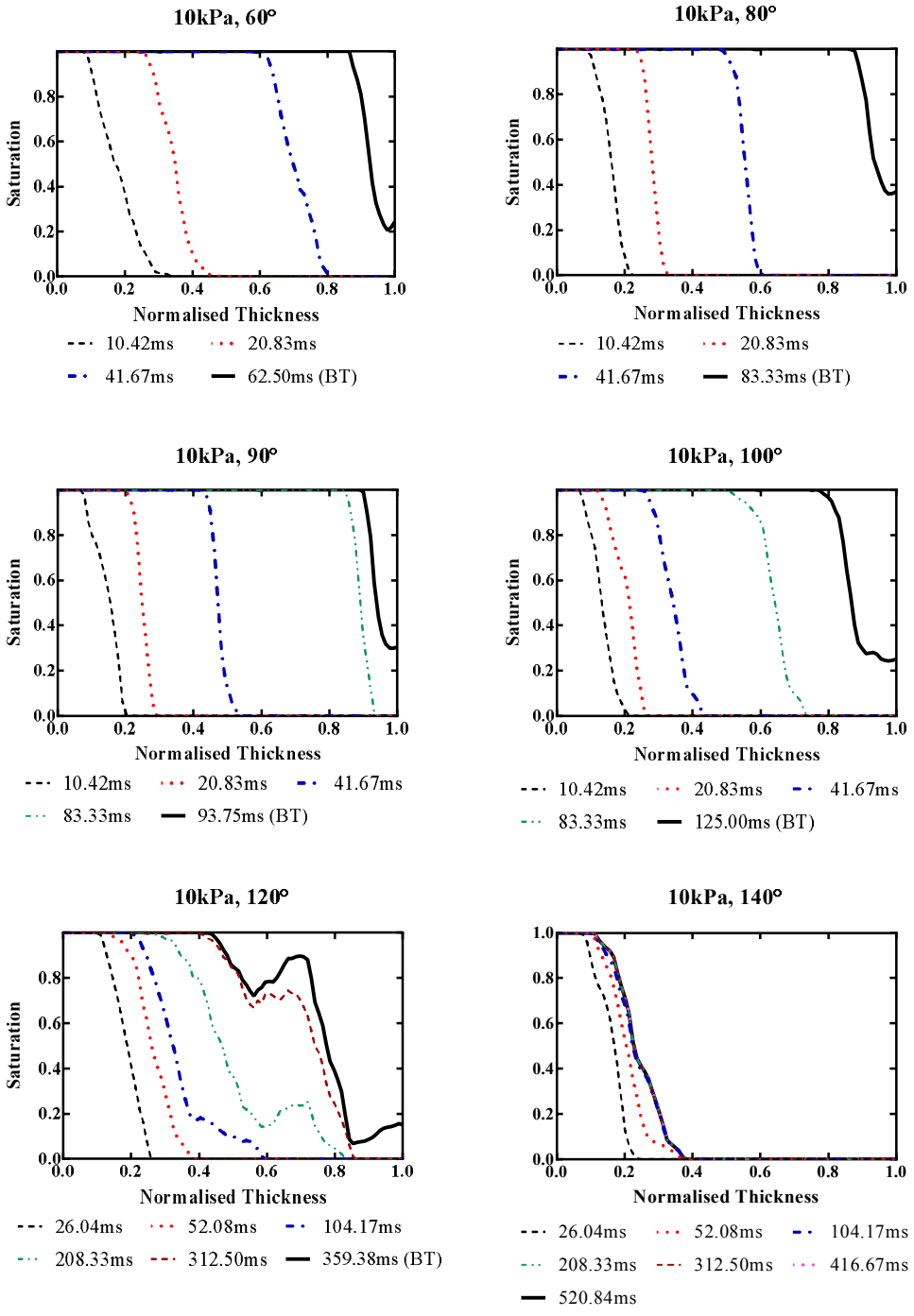

Figure 7.17 Water distributions across the thickness of the Freudenberg felt at the applied pressure difference of 10kPa.

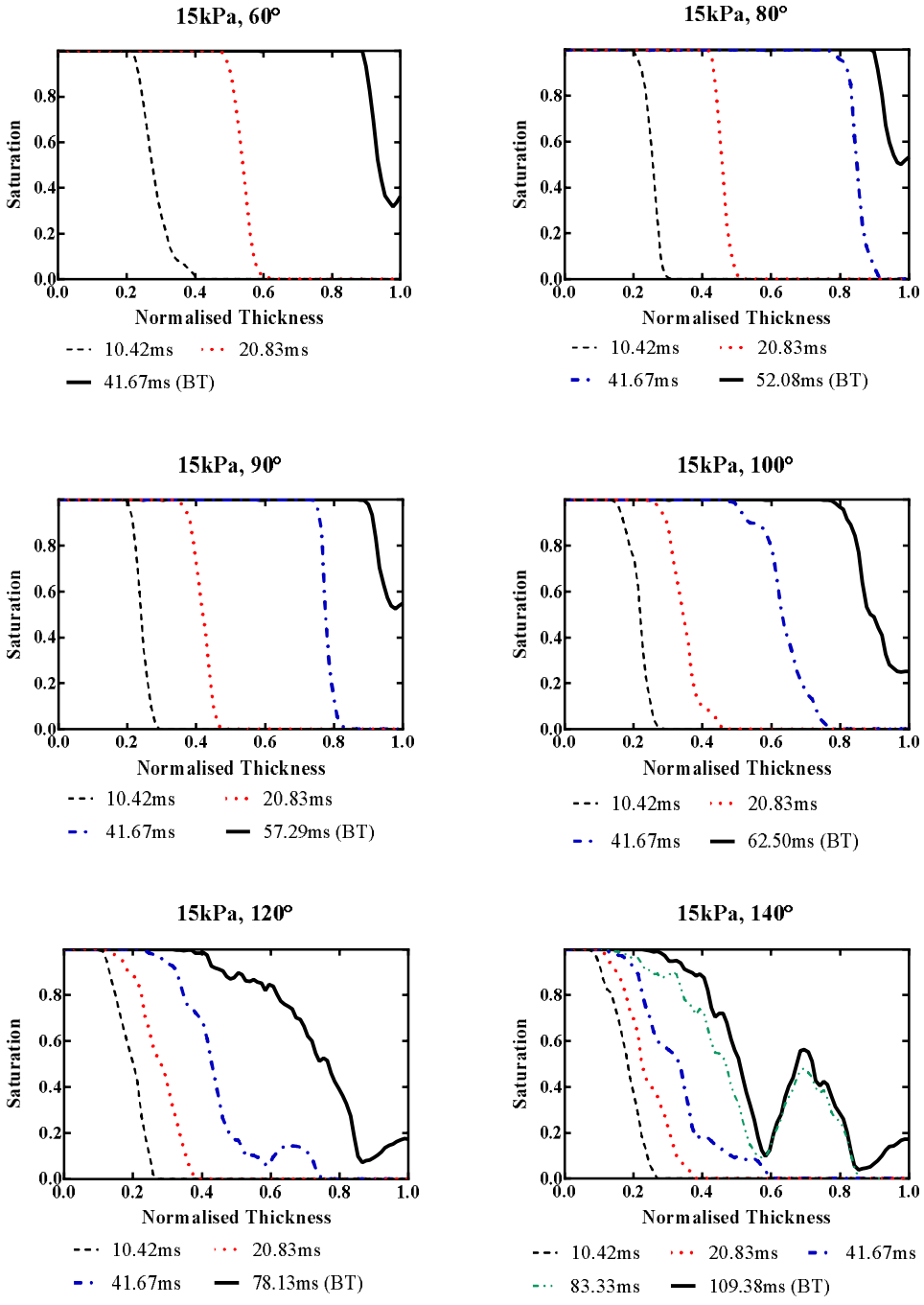

Figure 7.18 Water distributions across the thickness of the Freudenberg felt at the applied pressure difference of 15kPa.

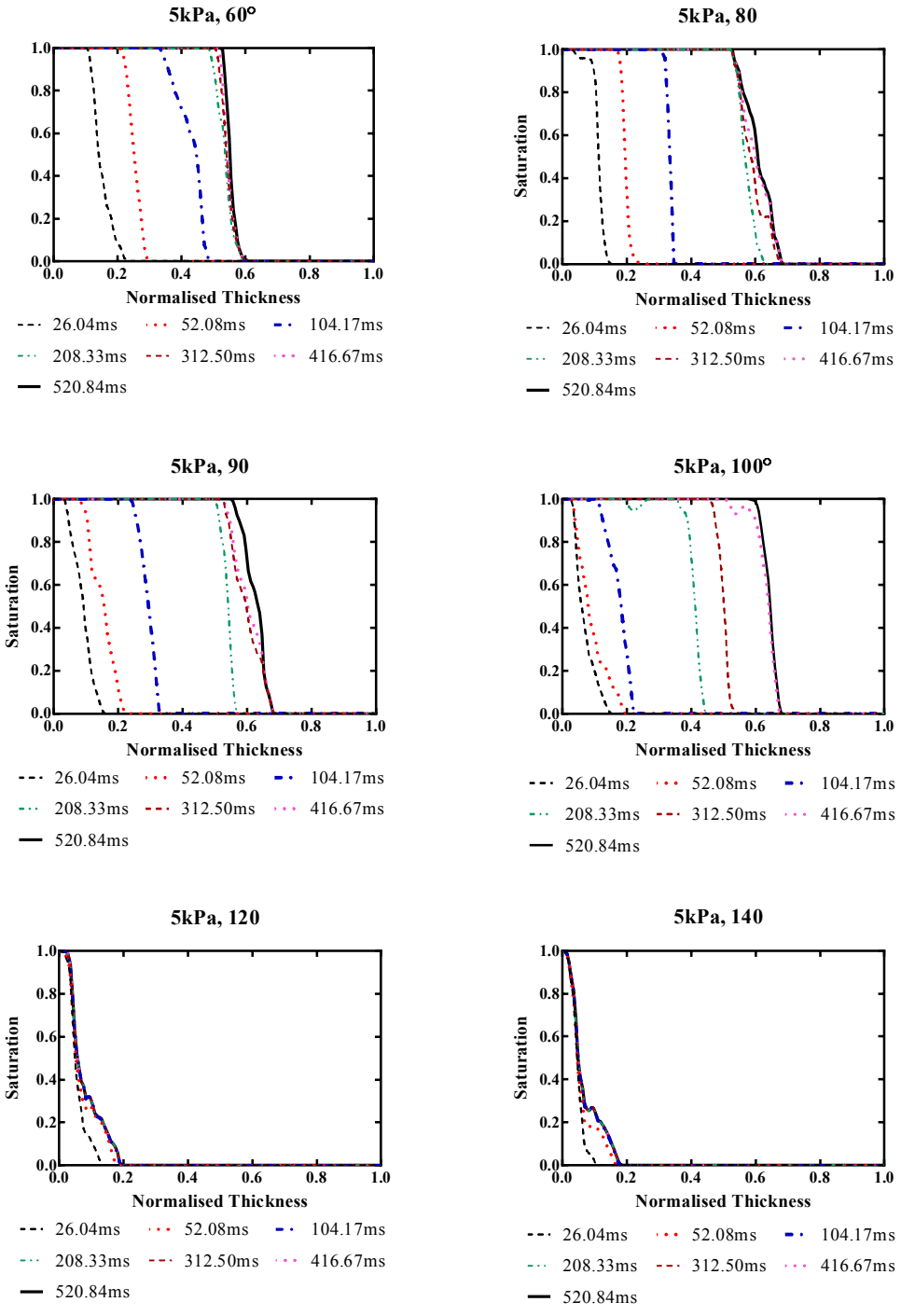

Figure 7.19 Water distributions across the thickness of the Toray paper at the applied pressure difference of 5kPa.

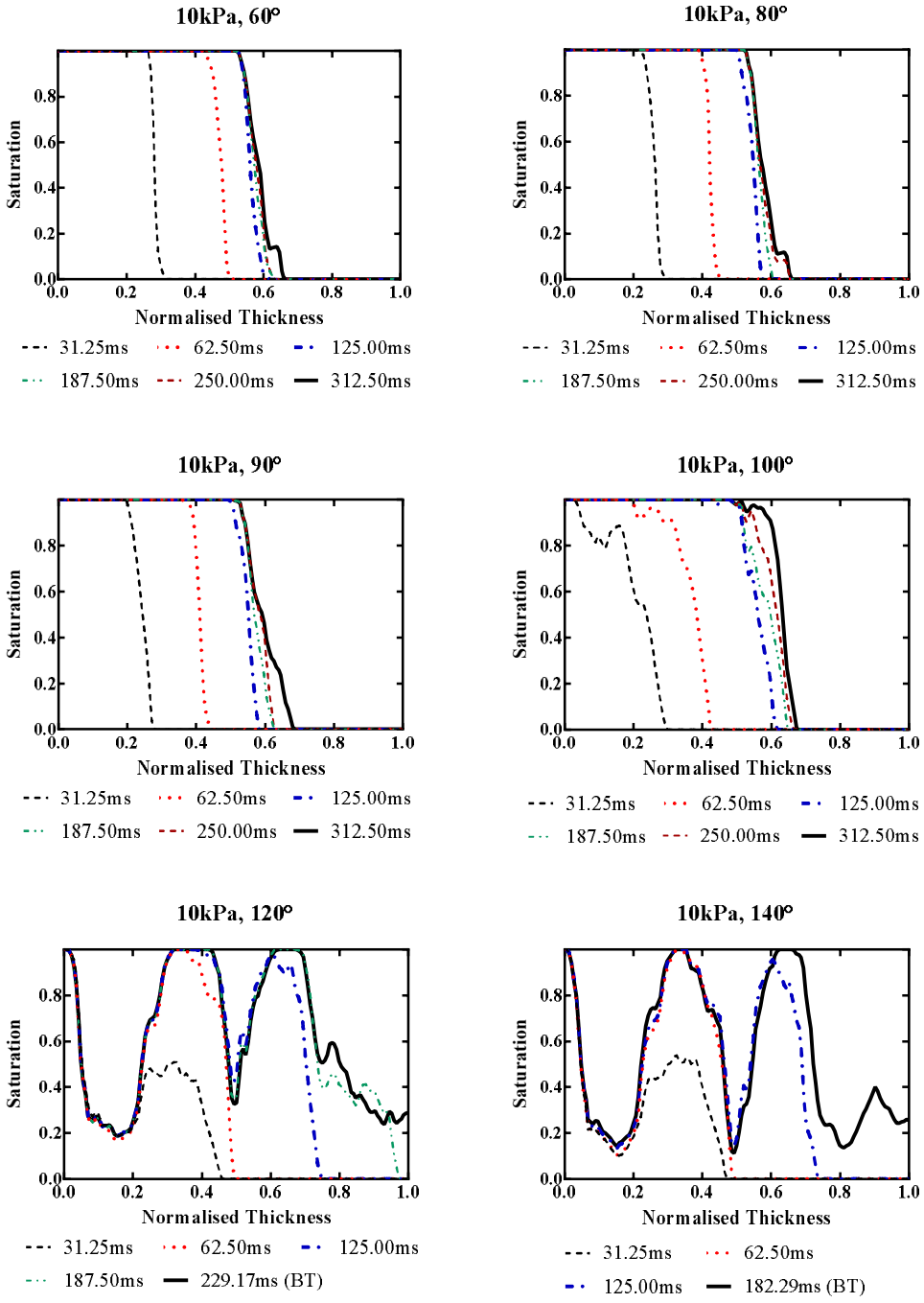

Figure 7.20 Water distributions across the thickness of the Toray paper at the applied pressure difference of 10kPa.

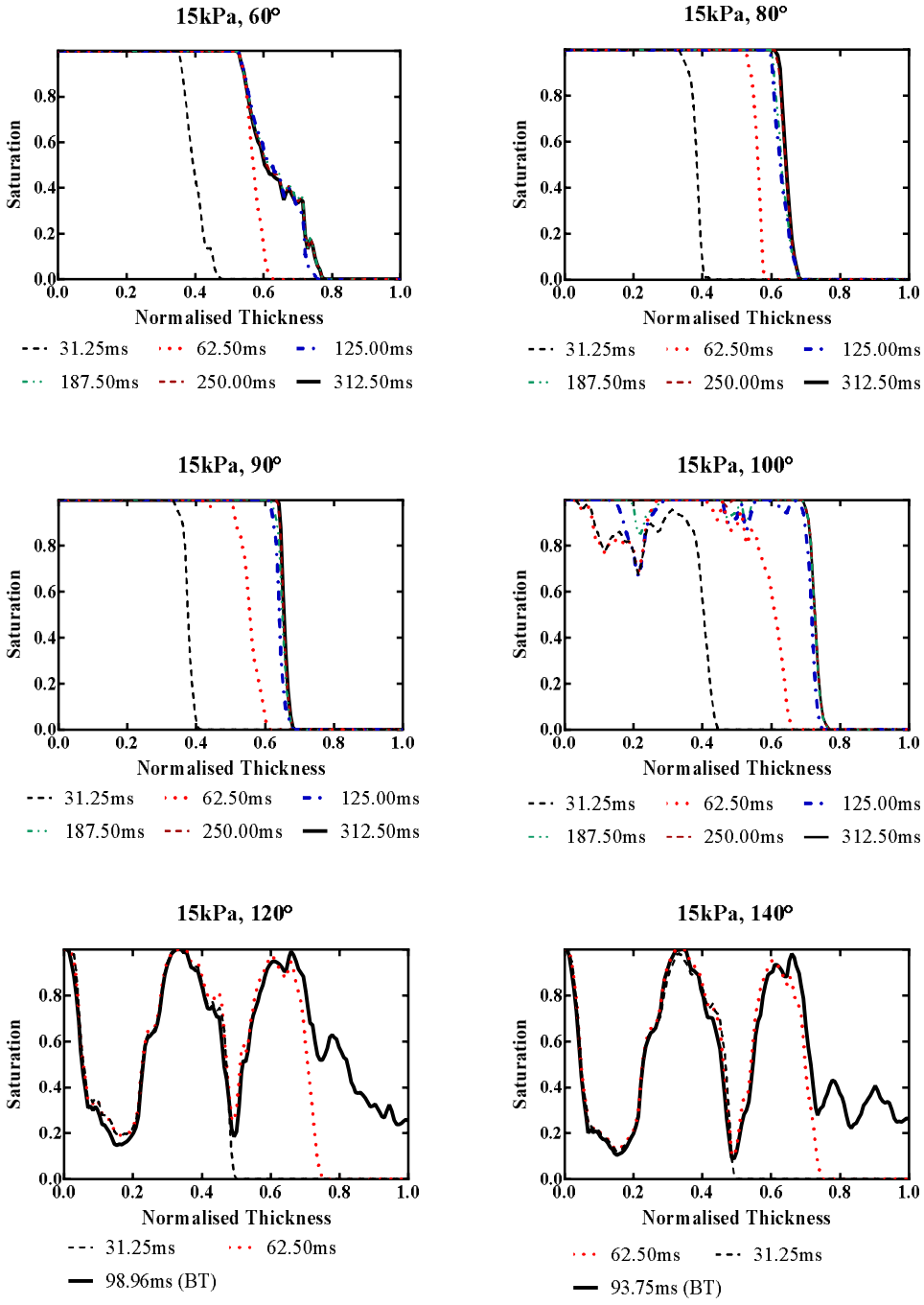

Figure 7.21 Water distributions across the thickness of the Toray paper at the applied pressure difference of 15kPa.

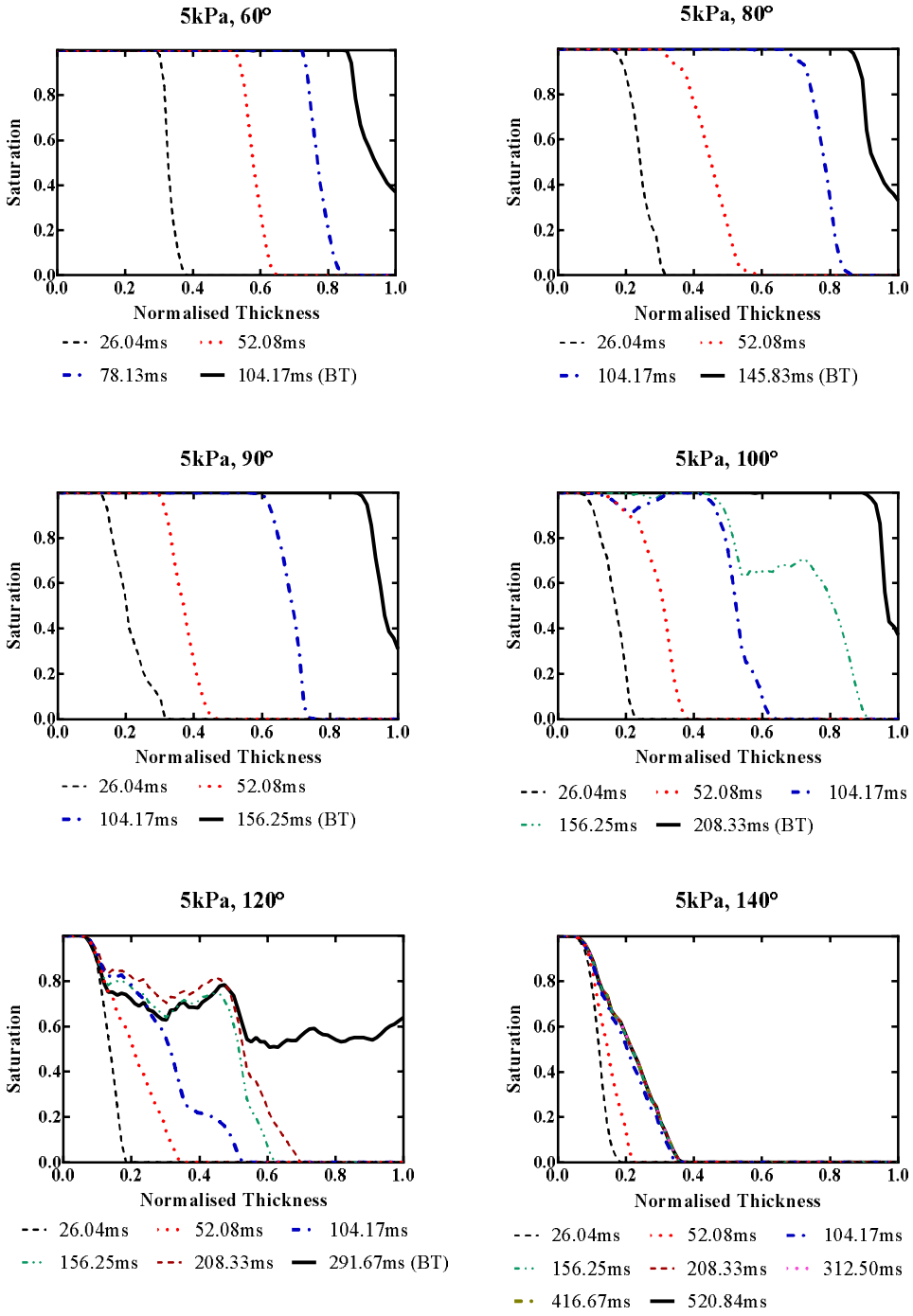

Figure 7.22 Water distributions across the thickness of the SGL paper at the applied pressure difference of 5kPa.

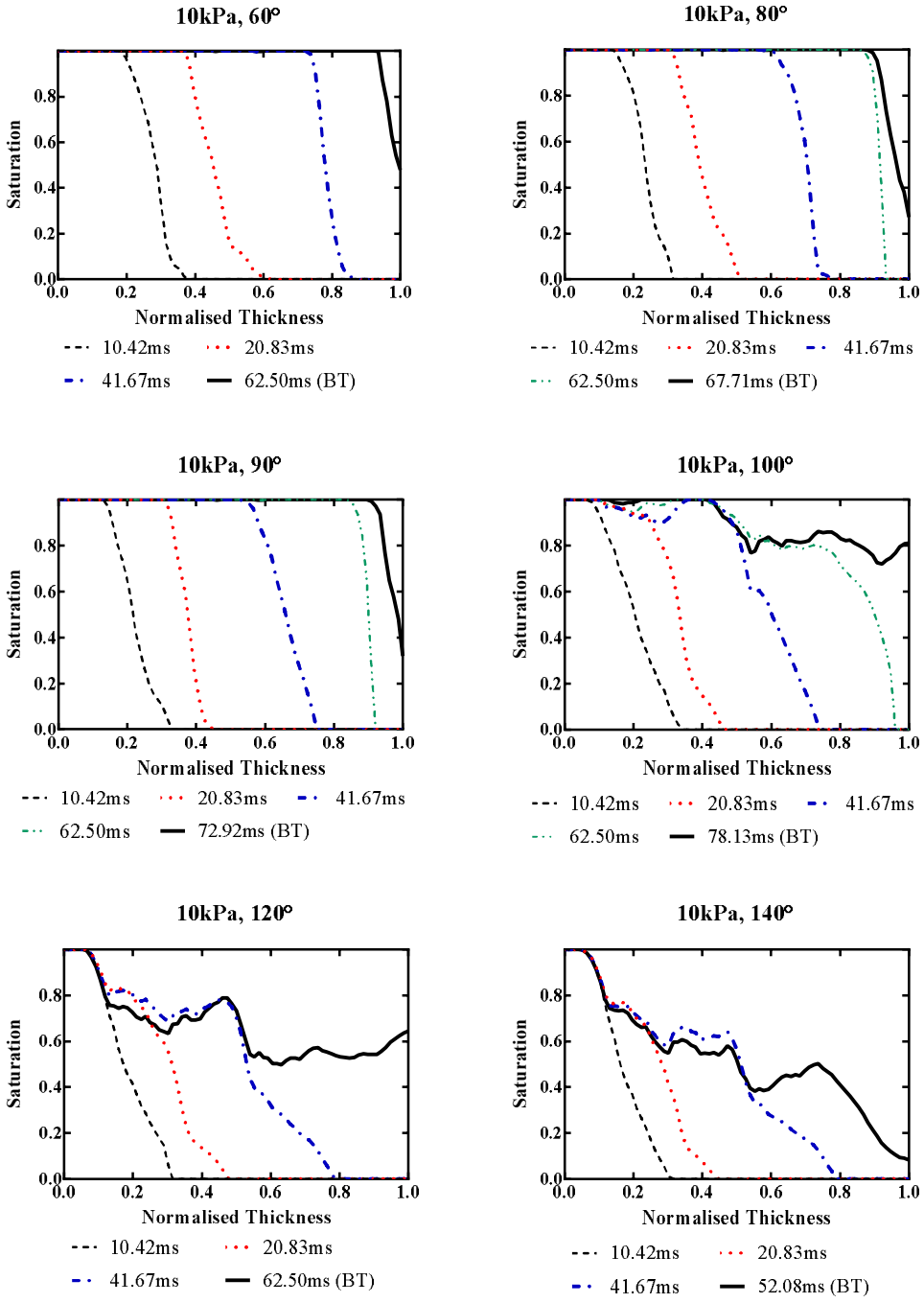

Figure 7.23 Water distributions across the thickness of the SGL paper at the applied pressure difference of 10kPa.

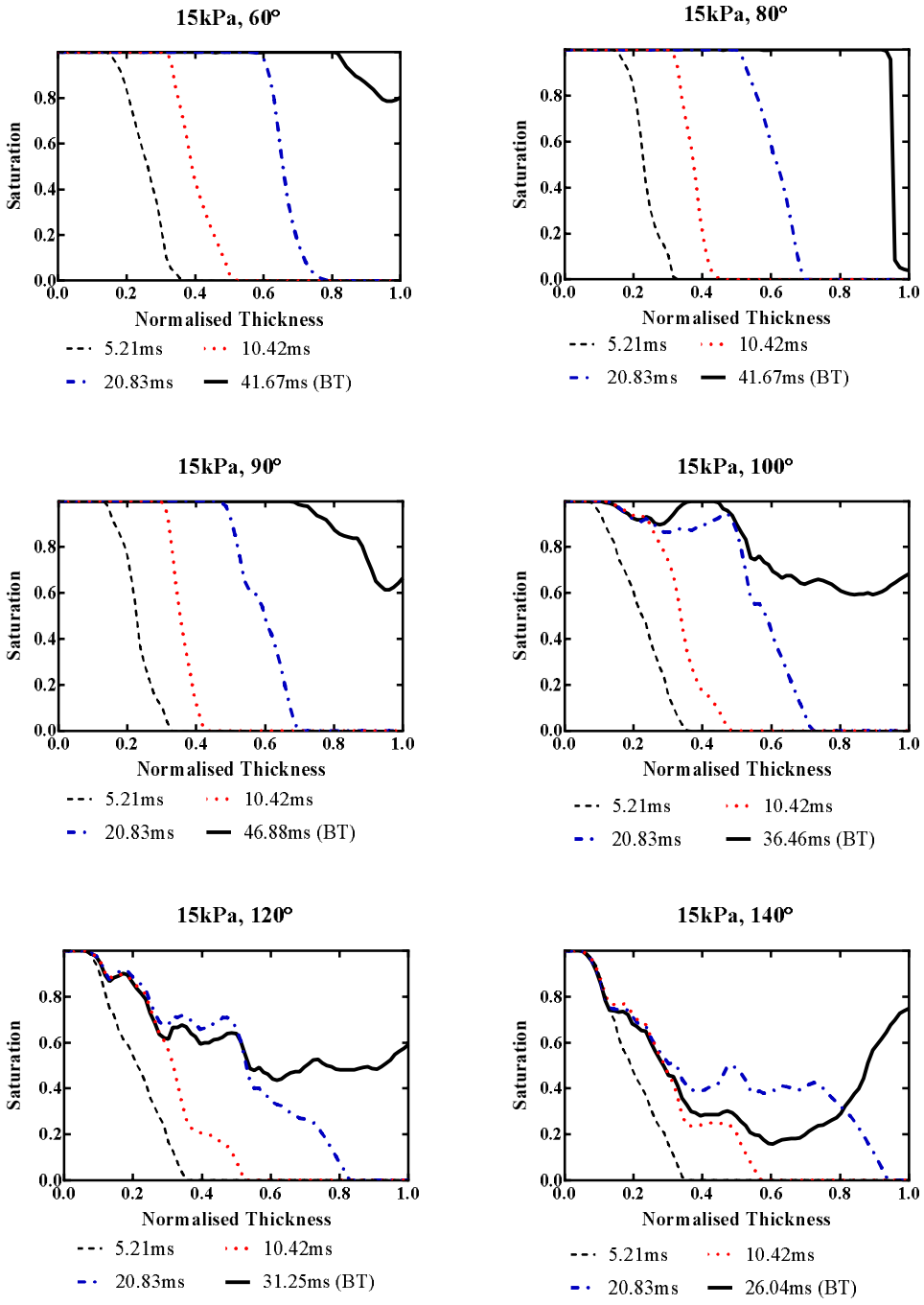

Figure 7.24 Water distributions across the thickness of the SGL paper at the applied pressure difference of 15kPa.

7.6.3 Breakthrough Behaviours

The Freudenberg felt, Toray paper and SGL paper show some similarities and differences in breakthrough behaviours. The Freudenberg felt experiences breakthrough at the hydrophilic, moderate and hydrophobic contact angles, whereas the Toray paper experiences water breakthrough only during the hydrophobic contact angles. The SGL paper, unlike its paper counterpart, experiences breakthrough at all contact angles showing a similar characteristic as the Freudenberg felt.

A possible reason for the similarity in breakthrough behaviour between the Freudenberg felt and the SGL paper, and the distinct difference between the two and the Toray paper would be the structure of the three samples. The Freudenberg felt has a 3D structure in which fibres travel in both in-plane and through-plane directions holding the structure together. No binding agent is required. The majority of its fibres travel in the in-plane direction, as seen in Fig. 5.3, which allows local saturation. The felt, however, also has fibres travelling in the through-plane direction as seen in Fig. 5.12(c). This means that at hydrophilic contact angles, water, with its adhesive nature, would also attach to these through-plane fibres and these would lead saturation through the GDL thickness causing the stable displacement breakthrough phenomenon. On the other hand, the Toray paper has a 2D structure in which fibres travel only in the in-plane direction. It, thus, requires a binding agent to hold the structure together. Besides significantly reducing pore sizes and the porosity of the sample, the carbonized binder substantially increases the contact area between the solid surface and liquid water (as seen in Fig. 5.6). For hydrophilic contact angles, this means that the increased surface area of the binder would attach and hold more water than a bare structure without binder. Hence, water in the Toray paper with hydrophilic contact angles will travel in the in-plane direction saturating the cross section layer by layer, rather than pass through it and breakthrough. Thus, water travelling with a stable displacement and full saturation but not breakthrough is observed in this case for the Toray paper. The SGL paper, unlike the Toray sample, which falls into the same category (i.e. paper-type structure), has a very similar behaviour to the Freudenberg felt sample as regards breakthrough. As with the felt sample, the SGL paper experiences breakthrough at all observed contact angles displaying a stable displacement for hydrophilic angles and capillary fingering for hydrophobic angles. The SGL paper has a

2D fibre structure with fibres only lying in the in-plane direction. This requires a binding agent to link the fibres together. In contrast to the Toray sample where a 2D smooth, sheet-like, binder is observed, the SGL binder is substantially rougher. This rough binder spreads over the fibres of the sample lying in both in-plane and through-plane directions forming a 3D staircase-like binder (as seen in Fig. 5.7). At hydrophilic contact angles, this means that the binder in the through-plane direction could draw water to move into the sample domain in the thickness direction and subsequently breakthrough the sample outlet. This indicates that this 3D binder has a significant role in breakthrough at hydrophilic angles for the SGL paper sample. This also implies that the binder in through-plane direction of the SGL paper plays a similar role as the through-plane fibres of the felt.

On the other hand, it was found that the structure of the GDL did not affect breakthrough in the hydrophobic GDL in which water travelling with capillary fingering is observed in all samples. With the inadhesive nature of the hydrophobic GDL sample, water is not attached by the fibres and binders of the sample. It travels through large pores with least resistance and then breaks through the sample thickness. The pressure difference applied across the thickness is required to be great enough, greater than the capillary pressure, to force water to pass through the pores.

As mentioned above, all three samples experience breakthrough at the hydrophobic contact angles. This, however, requires high pressure difference applied across the sample thickness. Based on the Young-Laplace equation, higher contact angle creates greater capillary resistance, which might prohibit water to pass through the pores of the sample. As a result, the Freudenberg felt and the Toray paper experience breakthrough at the hydrophobic angle only with 10kPa and 15kPa but not with 5kPa pressure difference. As with the Freudenberg felt and Toray paper, the SGL paper presents the same trend at the hydrophobic angles. There is, however, a slight difference in that the SGL paper with 5kPa experiences breakthrough at low and medium hydrophobic contact angles (100° and 120°), while this never happens in the Freudenberg felt and the Toray paper at 5kPa. The SGL paper at 5kPa, however, never experiences breakthrough at 140°, similar to the Freudenberg and Toray samples. The 140° case creates greater capillary resistance than the 100° and 120° cases and seems to be too great

for the water to intrude the pores and break through the outlet. This highlights the combined effect of contact angle, pressure and structure on breakthrough characteristics.

7.6.4 Breakthrough Saturation Levels

Fig. 7.25-Fig. 7.27 show the saturation levels at the point where water breaks through the outlet of the tested samples. The breakthrough saturation levels were observed over the contact angles of 60°, 80°, 90°, 100°, 120° and 140° under the applied pressure differences of 5kPa, 10kPa and 15kPa.

GDL with Felt Structure

Fig. 7.25 shows the change of saturation levels over a range of observed wettability, from hydrophilic to hydrophobic, of the Freudenberg felt under the pressure differences of 5kPa, 10kPa and 15kPa applied across the sample thickness. The three investigated pressure differences show very similar saturation levels at breakthrough. For low and intermediate contact angles, the figure shows that the saturation levels are almost 100% suggesting that liquid water occupies almost all pores of the sample domains. However, the saturation levels decrease substantially from full saturation in the hydrophilic and moderate cases to partial saturation in the medium/high hydrophobic domains. At the high hydrophobic contact angles of 140°, the saturation levels reduce significantly to about 62.5%. The change in saturation levels from full to partial saturation occurs between 100° and 120°. Almost full saturation is observed at 100° but at 120° the saturation has decreased by 18.7% showing the influence of hydrophobicity on saturation in the Freudenberg felt domain.

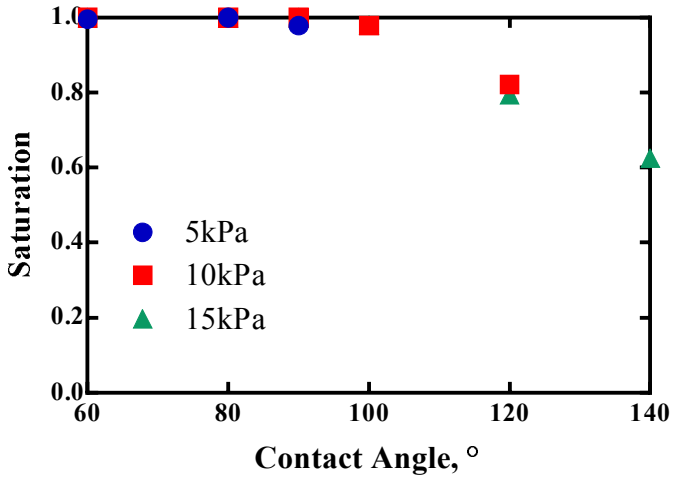

Figure 7.25 Water saturation levels of the Freudenberg felt at breakthrough.

GDLs with Paper Structure

Fig. 7.26 shows saturation levels at breakthrough of the Toray paper at different contact angles. The breakthrough saturation at the contact angles of 110°, 115° and 130° was also examined to confirm a decreasing trend in saturation level and find the most accurate contact angle that could cause water to begin breakthrough at observed pressure differences. It was found that breakthrough only occurs in the 10kPa and 15kPa cases at the hydrophobic contact angles of 115° upwards. The saturation levels at breakthrough show a decreasing trend as the hydrophobic angle increases. At the high hydrophobic contact angle of 140° with 15kPa, the saturation level at breakthrough is just about 54.3%. Again, the three applied pressure differences exhibit comparable saturation levels at breakthrough, similar to what was seen in the Freudenberg felt.

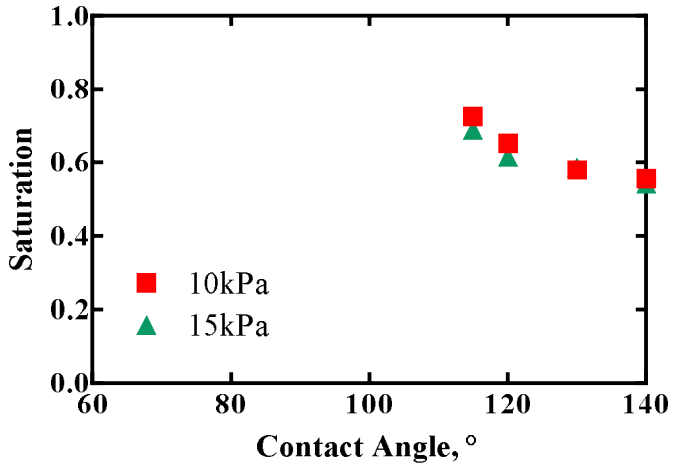

Figure 7.26 Water saturation levels of the Toray paper at breakthrough.

As with the Freudenberg felt, the saturation figure of the SGL paper shows that the GDL wettability affects the saturation levels at breakthrough significantly. For low and intermediate contact angles, the figure shows that the saturation levels are almost 100% indicating that water saturates the whole GDL domain when water breaks through the outlet. The high contact angles, on the other hand, exhibit decreased saturation levels. It is observed that the saturation levels reduce greatly to just about 39.2% at the contact angles of 140°. The transition from full to partial saturation occurs between 90° and 100°. The figure shows full saturation at 90° but at 100° the saturation has decreased by 8.3% suggesting the impact of hydrophobicity on saturation in the SGL paper domain. Similar to what was seen in Freudenberg felt and Toray paper, the three applied pressure differences show comparable saturation levels for the whole range of contact angles observed.

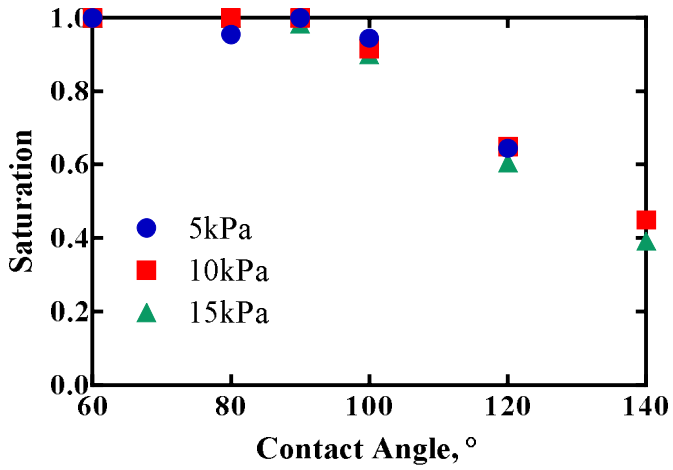

Figure 7.27 Water saturation levels of the SGL paper at breakthrough.

For all samples, the results indicated that contact angle plays a major role on saturation levels at breakthrough. At hydrophilic contact angles, water occupies all pores saturating the whole domain and showing full saturation at breakthrough. On the other hand, at hydrophobic contact angles, water partially saturates the domain displaying a significant decrease in saturation at breakthrough. At 140°, for example, the average saturation level of the three samples is about 52.0%, indicating that approximately half of the GDL volume is available for gas transport. A decrease in saturation level with an increasing hydrophobicity agrees with the results reported in [25, 29-31] which indicated that the enhancement of hydrophobicity of the GDL provides more available spaces for gas transport through the GDL. The Freudenberg felt and the SGL paper show very similar trends in saturation at breakthrough. Water generally passes through the sample outlet for all contact angles displaying full saturation at hydrophilic contact angles and partial saturation at hydrophobic contact angles. On the other hand, the Toray paper presents a different trend in which water only passes through the outlet at the hydrophobic contact angles showing partial saturation at breakthrough. The SGL paper shows significantly lower saturation level at breakthrough with only 39.2% saturation at 140°. Conversely, the Freudenberg felt and Toray paper show significantly higher saturation levels at breakthrough (62.5% and 54.3% respectively).

As regards pressure difference, it is found that the pressure difference applied across the sample thickness does not affect the saturation levels at breakthrough. With 5kPa, 10kPa and 15kPa, all samples show almost the same saturation levels over the range of contact angles observed (with less than 5% difference in breakthrough saturation on average). Pressure difference has a significant impact on breakthrough as it controls whether it actually occurs. With 10kPa and 15kPa, water generally passes through all sample domains. With 5kPa, it seems that the pressure is not great enough to allow water breakthrough; thus, breakthrough is rarely experienced in all samples at this relatively low pressure difference.

7.7 Conclusions

The behaviour of liquid water in GDLs under the effects of GDL structure, surface wettability and applied pressure difference was investigated using the two-phase LB model and the XCT technique. The reconstructed models of three GDL samples, felt, paper with 2D binder and paper with 3D binder, were integrated into the LB solver to model water transport behaviour in the GDLs under a range of GDL wettability properties and applied pressure differences. The behaviour of liquid water in the GDLs, including invasion patterns, water distribution and breakthrough behaviour, was then analysed. Finally, a comparison among the three distinct GDL structures was run. The following conclusions can be drawn from this work.

Effect of GDL wettability

It was found that the invasion pattern and saturation level of liquid water in the GDLs was controlled by the GDL wettability (contact angle). Liquid water travelled with a stable displacement saturating all pores in hydrophilic GDLs, while it travelled with capillary fingering causing decreased saturation in hydrophobic GDLs. It was observed that the saturation levels decreased to about 50% in the highly hydrophobic GDLs leaving about half of the pore spaces available for gas transport. The transition between the two phenomena is sharp and occurs between 90° and 120°. In addition, breakthrough occurrence was found to be partially controlled by GDL wettability. At a given applied

pressure difference, it was found that a rare breakthrough occurrence took place at higher contact angles.

Effect of applied pressure difference

It was found that the applied pressure difference controls breakthrough occurrence in the GDLs. In general, liquid water breaks through the GDL thickness for the 10kPa and 15kPa cases whilst rare breakthrough was observed for the 5kPa case. The latter suggested that the pressure difference of 5kPa was not sufficient to overcome the capillary resistance created by the GDL pores. In terms of invasion patterns, it was found that the applied pressure difference has no effect on them. A stable displacement was observed in hydrophilic GDLs and a capillary fingering was observed in hydrophobic GDLs for all applied pressure differences. In regards saturation, it was found that the applied pressure difference does not affect saturation levels. Based on the breakthrough saturation figures, the three applied pressure differences show the same trend, whereby GDL samples become fully saturated for the hydrophilic angles and partially saturated for the hydrophobic angles. All three applied pressures show very similar saturation levels at breakthrough for the whole range of observed contact angles.

Effect of GDL structure

As far as invasion patterns are concerned, although the three GDL samples studied are influenced similarly by wettability properties, they all show differences in capillary fingering in the hydrophobic cases. Liquid water in the felt mainly invaded in the through-plane direction. On the other hand, invasion of liquid water in the in-plane direction, occupying all pores in certain cross sections, was clearly observed in the paper with 2D binder. Invasion in both directions was observed in the paper with 3D binder but the water did not saturate fully the cross section, as had occurred in the paper with 2D binder. It was also found that the structure of each GDL sample has a great impact on breakthrough in hydrophilic GDLs. The difference in the nature of breakthrough is due to the number of through-plane fibres in the felt structure compared to paper, which has virtually none. Through-plane fibres favour through-plane water transport at hydrophilic contact angles when the water interaction is adhesive. Likewise, the through-plane binder in the paper with 3D binder was found to perform a similar role to the through-plane

fibres in the felt, as both could lead liquid water to travel in this direction and break through. In contrast, the paper with 2D binder mainly consists of in-plane fibres and binder. Thus, liquid water would attach to these fibres and binder and then move along this in-plane direction saturating the cross section rather than travelling in the thickness direction and breaking through. On the other hand, GDL structure was found to have negligible influence on breakthrough in the hydrophobic GDLs. Each GDL structure, however, contributed to a significant difference in capillary fingering in the GDLs with hydrophobic wettability.

This study observes water transport in uncompressed GDL materials with no additional PTFE and MPL. The simulations completed are expected to resemble ex-situ experiments of liquid invasion in a GDL, rather than actual invasion in a GDL within an operating fuel cell.

Chapter 8
Conclusions and Future Work

8.1 Introduction

The aim of this thesis was to develop our understanding of the effects of material structure on liquid water transport behaviours in PEMFC GDLs using a combination of the Lattice Boltzmann (LB) method and X-ray computed tomography (XCT). In this thesis, three GDL materials, felt, paper with 2D binder and paper with 3D binder, were employed to investigate the effects of each structure on liquid water transport behaviours. Each sample was reconstructed via the XCT process into a 3D digital binary volumetric model and the digital model was then integrated into the two-phase LB solver in order to model liquid water transport in the GDL.

8.2 Conclusions

Lattice Boltzmann modelling and X-ray computed tomography

- It has been demonstrated that some key material properties, including thickness and porosity, can be obtained directly from X-ray images. The absolute permeability and tortuosity of an X-ray model have also been obtained either through the LB model or through an analytical approach.
- The influence of image resolution variation on simulated gas permeability of an existing X-ray reconstructed GDL has been determined using the single-phase LB model. The results show significant influence of resolution variation on accuracy and computational time, while the importance of selecting a resolution for image generation for LB simulation has also been highlighted.

Structure and material properties analysis

- It has been shown that the porosity distribution of the GDL sample can also been obtained directly from the X-ray binary image slices of the sample and the

resulting porosity distribution can be used to calculate permeability and tortuosity distribution using an analytical model.

- Based on the porosity distribution analysis, the heterogeneous porosity distribution across the thickness of each sample has been observed. It is of great importance for PEMFC modellers to consider this non-uniform porosity rather than assume the uniform porosity of a GDL.
- As regards porosity distribution, it has been demonstrated that each sample has a distinct through-plane porosity distribution profile. Felt has a more uniform porosity in the core region compared to the paper GDLs. The paper GDLs, on the other hand, exhibit valley pattern distribution, and peaks and troughs distribution for the thin paper and thick paper respectively.
- An analytical model, namely the TS model, which is able to reveal the permeability and tortuosity distributions of the GDL samples, has been employed. It has been shown that the permeability distribution of each sample exhibits a similar trend to the porosity distribution whilst tortuosity is inversely proportional to porosity.
- The average value for each property was determined for the bulk region, effective region and core region. Better agreement was found with the average values of the effective region, which were defined based on the thickness measured directly from the tomographic binary slices, and the values reported in the literature.
- The LB model has also been employed to characterise the permeability and tortuosity of the GDL samples. Comparing to the TS model, we found better agreement between the LB simulated results and data available in the literature. This can be attributed to the capability of the LB approach to incorporate the actual structures of the GDLs into the model. This is in contrast to the TS model, which considers the GDL as an idealised structure of purely cylindrical straight fibres.

Water transport in the GDL

The effects of GDL structure on the invasion pattern, saturation distribution and breakthrough behaviour of liquid water in the GDL have been demonstrated using the two-phase LB model and the following conclusions can be drawn from the research.

- As regards invasion pattern, although the invasion pattern in the GDL is controlled by the wetting property (contact angle) displaying a stable displacement and capillary fingering in hydrophilic and hydrophobic GDLs respectively, it was found that invasion of liquid water in each sample exhibits differently in capillary fingering at hydrophobic contact angles.
    - Liquid water invasion in the felt and paper with 3D binder shows a rather similar pattern in which liquid water exhibits finger-like invasion fronts and invades mainly in the through-plane direction. The only difference is that the paper with 3D binder displays more convex sphere-like shaped invasion fronts than the felt.
    - Liquid water in the paper with 2D binder, on the other hand, mainly invades in the in-plane direction and saturates all pores at certain cross-sections.
    - This significant difference has been attributed to the structure of the paper with 2D binder in which the large area lacking fibres can easily be distinguished from the areas that are much more densely populated. The high porosity area lacking fibres acts as a large pore creating least resistance, thus, allowing liquid water to travel along this direction rather than through the dense area in the thickness direction.
- With regards to saturation distribution, it was found that this has a strong dependence on porosity distribution. The peaks and troughs appearing in the porosity distribution profile across the thickness of the thick paper (i.e. paper with 2D binder) correspond to the low and high saturation regions in the sample.
- As regards breakthrough behaviours of liquid water, it was observed that the paper with 3D binder performs similarly to the felt GDL rather than its paper counterpart at the hydrophilic contact angles. On the other hand, all samples act similarly regarding breakthrough at hydrophobic contact angles.
    - The through-plane fibres of the felt and the through-plane binder of the paper with 3D binder perform the same function in assisting breakthrough during hydrophilic contact angle. Due to the adhesiveness present at hydrophilic contact angles, these through-plane fibres and

through-plane binder can draw liquid water to move in the thickness direction and then break through the sample outlet.

- The paper with 2D or sheet-like binder with hydrophilic contact angles, on the other hand, attaches and leads liquid water to travel in the in-plane direction along the fibres and binder direction saturating the cross-sections rather than passing through and breaking through the sample outlet.
- At hydrophobic contact angles, it was found that the structure of the GDL does not affect breakthrough occurrence. Due to the inadhesive nature of the hydrophobic GDL, liquid water does not attach to fibres and binders; instead, it travels through large pores with least resistance and breaks through the GDL thickness if the pressure is great enough to overcome the capillary resistance of small pores.

8.3 Suggestions for Future Work

This thesis proves the capability of the combined methodology of the LB method and X-ray computed tomography to characterise GDL properties and model liquid water transport in the GDL. With regards to liquid water transport modelling, liquid water invasion patterns, distributions and breakthrough behaviours in three different GDL materials with morphological differences under various wettability conditions have been demonstrated. Further work, however, is needed in order to enrich our understanding of liquid water transport in GDLs.

- In this work, we focused only on modelling liquid water transport in GDLs with uniform wettability representing a fresh GDL. The wettability of the GDL, however, changes over time which results in a mixed wettability condition representing an aged GDL. Hence, the next step could be the investigation of liquid water transport behaviour in a mixed wetted GDL with different hydrophilic fractions and patterns in order to examine the effect of aged GDLs on liquid water transport and flooding phenomena in GDLs.

- Further work also requires the investigation of liquid water transport in a broader range of GDL materials, including carbon cloth GDLs, which were not included in this study.
- Since the GDL is commonly compressed under high compressive loads, which can result in its morphological change, additional work could investigate the effect of compression on liquid water transport behaviour by comparing liquid water transport behaviour in a compressed GDL with that in an uncompressed GDL.
- In terms of computation, the LB simulation demands large computational resources, thus limiting its simulation capability to a very small volume of the GDL, which might not be representative. Parallel computing could be a solution to meet its large computational demands and allow simulation in a larger and more representative volume of the GDL.

References

1. Larminie, J., A. Dicks, and M.S. McDonald, *Fuel cell systems explained*. Vol. 2. 2003: Wiley New York.
2. Li, X., *Principles of Fuel Cells*. 2005: Taylor & Francis.
3. Litster, S. and G. McLean, *PEM fuel cell electrodes.* Journal of Power Sources, 2004. **130**(1-2): p. 61-76.
4. Jiao, K. and X. Li, *Water transport in polymer electrolyte membrane fuel cells.* Progress in Energy and Combustion Science, 2011. **37**(3): p. 221-291.
5. Li, H., et al., *A review of water flooding issues in the proton exchange membrane fuel cell.* Journal of Power Sources, 2008. **178**(1): p. 103-117.
6. Wang, C.Y., *Fundamental models for fuel cell engineering.* Chemical Reviews, 2004. **104**(10): p. 4727-4765.
7. Schmittinger, W. and A. Vahidi, *A review of the main parameters influencing long-term performance and durability of PEM fuel cells.* Journal of Power Sources, 2008. **180**(1): p. 1-14.
8. Wu, J., et al., *A review of PEM fuel cell durability: degradation mechanisms and mitigation strategies.* Journal of Power Sources, 2008. **184**(1): p. 104-119.
9. Dai, W., et al., *A review on water balance in the membrane electrode assembly of proton exchange membrane fuel cells.* International Journal of Hydrogen Energy, 2009. **34**(23): p. 9461-9478.
10. Pasaogullari, U. and C.Y. Wang, *Liquid water transport in gas diffusion layer of polymer electrolyte fuel cells.* Journal of the Electrochemical Society, 2004. **151**(3): p. A399-A406.
11. Zhang, F., X. Yang, and C. Wang, *Liquid water removal from a polymer electrolyte fuel cell.* Journal of the Electrochemical Society, 2006. **153**(2): p. A225-A232.
12. Pasaogullari, U. and C.-Y. Wang, *Two-phase modeling and flooding prediction of polymer electrolyte fuel cells.* Journal of The Electrochemical Society, 2005. **152**(2): p. A380-A390.
13. Bazylak, A., *Liquid water visualization in PEM fuel cells: A review.* International Journal of Hydrogen Energy, 2009. **34**(9): p. 3845-3857.

14. Ge, S. and C.-Y. Wang, *In situ imaging of liquid water and ice formation in an operating PEFC during cold start.* Electrochemical and Solid-State Letters, 2006. **9**(11): p. A499-A503.
15. Mathias, M.F., et al., *Diffusion media materials and characterisation*, in *Handbook of Fuel Cells*. 2010, John Wiley & Sons, Ltd.
16. Barbir, F., *PEM fuel cells: theory and practice*. 2013: Academic Press.
17. El-kharouf, A. and B.G. Pollet, *Gas Diffusion Media and Their Degradation.* Polymer Electrolyte Fuel Cell Degradation, 2011: p. 215.
18. Benziger, J., et al., *Water flow in the gas diffusion layer of PEM fuel cells.* Journal of Membrane Science, 2005. **261**(1–2): p. 98-106.
19. Rama, P., et al., *An X-Ray Tomography Based Lattice Boltzmann Simulation Study on Gas Diffusion Layers of Polymer Electrolyte Fuel Cells.* Journal of Fuel Cell Science and Technology, 2010. **7**(3): p. 031015-031015.
20. Wang, Y., C.-Y. Wang, and K.S. Chen, *Elucidating differences between carbon paper and carbon cloth in polymer electrolyte fuel cells.* Electrochimica Acta, 2007. **52**(12): p. 3965-3975.
21. Wilkinson, D.P., et al., *Proton Exchange Membrane Fuel Cells: Materials Properties and Performance*. 2009: Taylor & Francis.
22. Atiyeh, H.K., et al., *Experimental investigation of the role of a microporous layer on the water transport and performance of a PEM fuel cell.* Journal of Power Sources, 2007. **170**(1): p. 111-121.
23. Gostick, J.T., et al., *Capillary pressure and hydrophilic porosity in gas diffusion layers for polymer electrolyte fuel cells.* Journal of Power Sources, 2006. **156**(2): p. 375-387.
24. Kandlikar, S.G., M.L. Garofalo, and Z. Lu, *Water Management in A PEMFC: Water Transport Mechanism and Material Degradation in Gas Diffusion Layers.* Fuel Cells, 2011. **11**(6): p. 814-823.
25. Chapuis, O., et al., *Two-phase flow and evaporation in model fibrous media - Application to the gas diffusion layer of PEM fuel cells.* Journal of Power Sources, 2008. **178**(1): p. 258-268.

26. Lin, G. and T. Van Nguyen, *Effect of thickness and hydrophobic polymer content of the gas diffusion layer on electrode flooding level in a PEMFC.* Journal of The Electrochemical Society, 2005. **152**(10): p. A1942-A1948.
27. Park, S., J.W. Lee, and B.N. Popov, *A review of gas diffusion layer in PEM fuel cells: Materials and designs.* International Journal of Hydrogen Energy, 2012. **37**(7): p. 5850-5865.
28. Bevers, D., R. Rogers, and M. Von Bradke, *Examination of the influence of PTFE coating on the properties of carbon paper in polymer electrolyte fuel cells.* Journal of power sources, 1996. **63**(2): p. 193-201.
29. Hao, L. and P. Cheng, *Lattice Boltzmann simulations of water transport in gas diffusion layer of a polymer electrolyte membrane fuel cell.* Journal of Power Sources, 2010. **195**(12): p. 3870-3881.
30. Rama, P., et al., *Simulation of liquid water breakthrough in a nanotomography reconstruction of a carbon paper gas-diffusion layer.* AIChE Journal, 2012. **58**(2): p. 646-655.
31. Gao, Y., et al., *Lattice Boltzmann simulation of water and gas flow in porous gas diffusion layers in fuel cells reconstructed from micro-tomography.* Computers & Mathematics with Applications, 2013. **65**(6): p. 891-900.
32. Park, G.G., et al., *Effect of PTFE contents in the gas diffusion media on the performance of PEMFC.* Journal of Power Sources, 2004. **131**(1-2): p. 182-187.
33. Lim, C. and C. Wang, *Effects of hydrophobic polymer content in GDL on power performance of a PEM fuel cell.* Electrochimica Acta, 2004. **49**(24): p. 4149-4156.
34. Prasanna, M., et al., *Influence of cathode gas diffusion media on the performance of the PEMFCs.* Journal of Power Sources, 2004. **131**(1): p. 147-154.
35. Velayutham, G., et al., *Effect of PTFE content in gas diffusion media and microlayer on the performance of PEMFC tested under ambient pressure.* Fuel Cells, 2007. **7**(4): p. 314-318.
36. Tuber, K., D. Pocza, and C. Hebling, *Visualization of water buildup in the cathode of a transparent PEM fuel cell.* Journal of Power Sources, 2003. **124**(2): p. 403-414.

37. Fairweather, J.D., et al., *A microfluidic approach for measuring capillary pressure in PEMFC gas diffusion layers.* Electrochemistry Communications, 2007. **9**(9): p. 2340-2345.
38. Gostick, J.T., et al., *Direct measurement of the capillary pressure characteristics of water-air-gas diffusion layer systems for PEM fuel cells.* Electrochemistry Communications, 2008. **10**(10): p. 1520-1523.
39. Cheung, P., J.D. Fairweather, and D.T. Schwartz, *Characterization of internal wetting in polymer electrolyte membrane gas diffusion layers.* Journal of Power Sources, 2009. **187**(2): p. 487-492.
40. Tamayol, A. and M. Bahrami, *Water permeation through gas diffusion layers of proton exchange membrane fuel cells.* Journal of Power Sources, 2011. **196**(15): p. 6356-6361.
41. Lee, C. and W. Mérida, *Gas diffusion layer durability under steady-state and freezing conditions.* Journal of power sources, 2007. **164**(1): p. 141-153.
42. Mukherjee, P.P., et al., *Numerical Modeling of Two-Phase Behavior in the PEFC Gas Diffusion Layer.* ECS Transactions, 2010. **26**(1): p. 97-106.
43. Sinha, P.K. and C.Y. Wang, *Liquid water transport in a mixed-wet gas diffusion layer of a polymer electrolyte fuel cell.* Chemical Engineering Science, 2008. **63**(4): p. 1081-1091.
44. Kuttanikkad, S.P., M. Prat, and J. Pauchet, *Pore-network simulations of two-phase flow in a thin porous layer of mixed wettability: Application to water transport in gas diffusion layers of proton exchange membrane fuel cells.* Journal of Power Sources, 2011. **196**(3): p. 1145-1155.
45. Wu, R., et al., *Impacts of the mixed wettability on liquid water and reactant gas transport through the gas diffusion layer of proton exchange membrane fuel cells.* International Journal of Heat and Mass Transfer, 2012. **55**(9): p. 2581-2589.
46. Arvay, A., et al., *Characterization techniques for gas diffusion layers for proton exchange membrane fuel cells – A review.* Journal of Power Sources, 2012. **213**(0): p. 317-337.
47. Cindrella, L., et al., *Gas diffusion layer for proton exchange membrane fuel cells—A review.* Journal of Power Sources, 2009. **194**(1): p. 146-160.

48. Nam, J.H. and M. Kaviany, *Effective diffusivity and water-saturation distribution in single- and two-layer PEMFC diffusion medium.* International Journal of Heat and Mass Transfer, 2003. **46**(24): p. 4595-4611.
49. Kong, C.S., et al., *Influence of pore-size distribution of diffusion layer on mass-transport problems of proton exchange membrane fuel cells.* Journal of Power Sources, 2002. **108**(1-2): p. 185-191.
50. Williams, M.V., et al., *Characterization of Gas Diffusion Layers for PEMFC.* Journal of The Electrochemical Society, 2004. **151**(8): p. A1173-A1180.
51. Zhan, Z., et al., *Effects of porosity distribution variation on the liquid water flux through gas diffusion layers of PEM fuel cells.* Journal of Power Sources, 2006. **160**(2): p. 1041-1048.
52. Chen, F.L., M.H. Chang, and P.T. Hsieh, *Two-phase transport in the cathode gas diffusion layer of PEM fuel cell with a gradient in porosity.* International Journal of Hydrogen Energy, 2008. **33**(10): p. 2525-2529.
53. Zhan, Z.G., et al., *Gas diffusion through differently structured gas diffusion layers of PEM fuel cells.* International Journal of Hydrogen Energy, 2007. **32**(17): p. 4443-4451.
54. Han, M., et al., *Characterization of gas diffusion layers for PEMFC.* Electrochimica Acta, 2008. **53**(16): p. 5361-5367.
55. Hiramitsu, Y., H. Sato, and M. Honi, *Prevention of the water flooding by micronizing the pore structure of gas diffusion layer for polymer electrolyte fuel cell.* Journal of Power Sources, 2010. **195**(17): p. 5543-5549.
56. Fishman, Z., J. Hinebaugh, and A. Bazylak, *Microscale Tomography Investigations of Heterogeneous Porosity Distributions of PEMFC GDLs.* Journal of the Electrochemical Society, 2010. **157**(11): p. B1643-B1650.
57. Hinebaugh, J., Z. Fishman, and A. Bazylak, *Unstructured Pore Network Modeling with Heterogeneous PEMFC GDL Porosity Distributions.* Journal of The Electrochemical Society, 2010. **157**(11): p. B1651-B1657.
58. Chang, W.R., et al., *Effect of clamping pressure on the performance of a PEM fuel cell.* Journal of Power Sources, 2007. **166**(1): p. 149-154.

59. Bazylak, A., et al., *Effect of compression on liquid water transport and microstructure of PEMFC gas diffusion layers.* Journal of Power Sources, 2007. **163**(2): p. 784-792.
60. Rama, P., et al., *A Numerical Study of Structural Change and Anisotropic Permeability in Compressed Carbon Cloth Polymer Electrolyte Fuel Cell Gas Diffusion Layers.* Fuel Cells, 2011. **11**(2): p. 274-285.
61. Pharoah, J.G., *On the permeability of gas diffusion media used in PEM fuel cells.* Journal of Power Sources, 2005. **144**(1): p. 77-82.
62. Gostick, J.T., et al., *In-plane and through-plane gas permeability of carbon fiber electrode backing layers.* Journal of Power Sources, 2006. **162**(1): p. 228-238.
63. Ismail, M.S., et al., *Through-Plane Permeability for Untreated and PTFE-Treated Gas Diffusion Layers in Proton Exchange Membrane Fuel Cells.* Journal of Fuel Cell Science and Technology, 2010. **7**(5): p. 051016-051016.
64. Feser, J.P., A.K. Prasad, and S.G. Advani, *Experimental characterization of in-plane permeability of gas diffusion layers.* Journal of Power Sources, 2006. **162**(2): p. 1226-1231.
65. Ahmed, D.H., H.J. Sung, and J. Bae, *Effect of GDL permeability on water and thermal management in PEMFCs - I. Isotropic and anisotropic permeability.* International Journal of Hydrogen Energy, 2008. **33**(14): p. 3767-3785.
66. Tamayol, A. and M. Bahrami, *In-plane gas permeability of proton exchange membrane fuel cell gas diffusion layers.* Journal of Power Sources, 2011. **196**(7): p. 3559-3564.
67. Hao, L. and P. Cheng, *Lattice Boltzmann simulations of anisotropic permeabilities in carbon paper gas diffusion layers.* Journal of Power Sources, 2009. **186**(1): p. 104-114.
68. Nabovati, A., E.W. Llewellin, and A. Sousa, *A general model for the permeability of fibrous porous media based on fluid flow simulations using the lattice Boltzmann method.* Composites Part A: Applied Science and Manufacturing, 2009. **40**(6): p. 860-869.
69. Rama, P., et al., *Determination of the anisotropic permeability of a carbon cloth gas diffusion layer through X-ray computer micro-tomography and single-phase*

lattice Boltzmann simulation. International Journal for Numerical Methods in Fluids, 2011. **67**(4): p. 518-530.

70. Ihonen, J., M. Mikkola, and G. Lindbergh, *Flooding of gas diffusion backing in PEFCs - Physical and electrochemical characterization.* Journal of the Electrochemical Society, 2004. **151**(8): p. A1152-A1161.
71. Nitta, I., et al., *Inhomogeneous compression of PEMFC gas diffusion layer Part I. Experimental.* Journal of Power Sources, 2007. **171**(1): p. 26-36.
72. Ahmed, D.H., H.J. Sung, and J. Bae, *Effect of GDL permeability on water and thermal management in PEMFCs - II. Clamping force.* International Journal of Hydrogen Energy, 2008. **33**(14): p. 3786-3800.
73. He, G.L., et al., *A fractal model for predicting permeability and liquid water relative permeability in the gas diffusion layer (GDL) of PEMFCs.* Journal of Power Sources, 2007. **163**(2): p. 846-852.
74. Hussaini, I.S. and C.Y. Wang, *Measurement of relative permeability of fuel cell diffusion media.* Journal of Power Sources, 2010. **195**(12): p. 3830-3840.
75. Litster, S., D. Sinton, and N. Djilali, *Ex situ visualization of liquid water transport in PEM fuel cell gas diffusion layers.* Journal of Power Sources, 2006. **154**(1): p. 95-105.
76. Bazylak, A., D. Sinton, and N. Djilali, *Dynamic water transport and droplet emergence in PEMFC gas diffusion layers.* Journal of Power Sources, 2008. **176**(1): p. 240-246.
77. Gao, B., et al., *Visualization of unstable water flow in a fuel cell gas diffusion layer.* Journal of Power Sources, 2009. **190**(2): p. 493-498.
78. Lu, Z., et al., *Water management studies in PEM fuel cells, part III: dynamic breakthrough and intermittent drainage characteristics from GDLs with and without MPLs.* International Journal of Hydrogen Energy, 2010. **35**(9): p. 4222-4233.
79. Manke, I., et al., *Investigation of water evolution and transport in fuel cells with high resolution synchrotron X-ray radiography.* Applied Physics Letters, 2007. **90**(17): p. 174105.

80. Zhang, J., et al., *In situ diagnostic of two-phase flow phenomena in polymer electrolyte fuel cells by neutron imaging: Part B. Material variations.* Electrochimica Acta, 2006. **51**(13): p. 2715-2727.
81. Kowal, J., et al., *Liquid water storage, distribution, and removal from diffusion media in PEFCS.* Journal of the Electrochemical Society, 2006. **153**(10): p. A1971-A1978.
82. Ous, T. and C. Arcoumanis, *Visualisation of water droplets during the operation of PEM fuel cells.* Journal of Power Sources, 2007. **173**(1): p. 137-148.
83. Ge, S. and C.-Y. Wang, *Liquid water formation and transport in the PEFC anode.* Journal of the Electrochemical Society, 2007. **154**(10): p. B998-B1005.
84. Yang, X., et al., *Visualization of liquid water transport in a PEFC.* Electrochemical and Solid-State Letters, 2004. **7**(11): p. A408-A411.
85. Mukherjee, P.P., Q.J. Kang, and C.Y. Wang, *Pore-scale modeling of two-phase transport in polymer electrolyte fuel cells-progress and perspective.* Energy & Environmental Science, 2011. **4**(2): p. 346-369.
86. Litster, S. and N. Djilali, *Two-phase transport in porous gas diffusion electrodes.* Developments in Heat Transfer, 2005. **19**: p. 175.
87. Cussler, E.L., *Diffusion: mass transfer in fluid systems*. 2009: Cambridge university press.
88. Bear, J., *Dynamics of Fluids in Porous Media*. 1988: Courier Dover Publications.
89. Sinha, P.K. and C.Y. Wang, *Pore-network modeling of liquid water transport in gas diffusion layer of a polymer electrolyte fuel cell.* Electrochimica Acta, 2007. **52**(28): p. 7936-7945.
90. Gostick, J.T., et al., *Pore network modeling of fibrous gas diffusion layers for polymer electrolyte membrane fuel cells.* Journal of Power Sources, 2007. **173**(1): p. 277-290.
91. Koido, T., T. Furusawa, and K. Moriyama, *An approach to modeling two-phase transport in the gas diffusion layer of a proton exchange membrane fuel cell.* Journal of Power Sources, 2008. **175**(1): p. 127-136.
92. Markicevic, B., A. Bazylak, and N. Djilali, *Determination of transport parameters for multiphase flow in porous gas diffusion electrodes using a capillary network model.* Journal of Power Sources, 2007. **171**(2): p. 706-717.

93. Bazylak, A., et al., *Numerical and microfluidic pore networks: Towards designs for directed water transport in GDLs.* Electrochimica Acta, 2008. **53**(26): p. 7630-7637.

94. Hinebaugh, J. and A. Bazylak. *PEM Fuel Cell Gas Diffusion Layer Modelling of Pore Structure and Predicted Liquid Water Saturation*. in *ASME 2011 9th International Conference on Fuel Cell Science, Engineering and Technology collocated with ASME 2011 5th International Conference on Energy Sustainability*. 2011. American Society of Mechanical Engineers.

95. Lee, K.J., J.H. Nam, and C.J. Kim, *Pore-network analysis of two-phase water transport in gas diffusion layers of polymer electrolyte membrane fuel cells.* Electrochimica Acta, 2009. **54**(4): p. 1166-1176.

96. Lee, K.J., J.H. Nam, and C.J. Kim, *Steady saturation distribution in hydrophobic gas-diffusion layers of polymer electrolyte membrane fuel cells: A pore-network study.* Journal of Power Sources, 2010. **195**(1): p. 130-141.

97. Lee, K.-J., J.H. Kang, and J.H. Nam, *Liquid water distribution in hydrophobic gas-diffusion layers with interconnect rib geometry: An invasion-percolation pore network analysis.* International Journal of Hydrogen Energy, 2014. **39**(12): p. 6646-6656.

98. Chraibi, H., et al., *Influence of wettability on liquid water transport in gas diffusion layer of proton exchange membrane fuel cells (PEMFC).* arXiv preprint arXiv:0909.2947, 2009.

99. Ceballos, L. and M. Prat, *Invasion percolation with inlet multiple injections and the water management problem in proton exchange membrane fuel cells.* Journal of Power Sources, 2010. **195**(3): p. 825-828.

100. Tan, Z.T., L. Jia, and Z.Q. Zhang, *A Study on the Transport Process in Gas Diffusion Layer of Proton Exchange Membrane Fuel Cells.* Journal of Thermal Science, 2011. **20**(5): p. 449-453.

101. Zhang, J.F., *Lattice Boltzmann method for microfluidics: models and applications.* Microfluidics and Nanofluidics, 2011. **10**(1): p. 1-28.

102. Van Doormaal, M.A. and J.G. Pharoah, *Determination of permeability in fibrous porous media using the lattice Boltzmann method with application to PEM fuel cells.* International journal for numerical methods in fluids, 2009. **59**(1): p. 75-89.

103. Gao, Y., et al., *An improved MRT lattice Boltzmann model for calculating anisotropic permeability of compressed and uncompressed carbon cloth gas diffusion layers based on x-ray computed micro-tomography.* Journal of Fuel Cell Science and Technology, 2012. **9**(4): p. 041010.

104. Gao, Y., et al., *Calculating the Anisotropic Permeability of Porous Media Using the Lattice Boltzmann Method and X-ray Computed Tomography.* Transport in Porous Media, 2012. **92**(2): p. 457-472.

105. Gao, Y., et al., *Modeling Fluid Flow in the Gas Diffusion Layers in PEMFC Using the Multiple Relaxation-time Lattice Boltzmann Method.* Fuel Cells, 2012. **12**(3): p. 365-381.

106. Ostadi, H., et al., *Nanotomography based study of gas diffusion layers.* Microelectronic Engineering, 2010. **87**(5–8): p. 1640-1642.

107. Ostadi, H., et al., *Threshold Fine-Tuning and 3D Characterisation of Porous Media Using X-ray Nanotomography.* Current Nanoscience, 2010. **6**(2): p. 226-231.

108. Ostadi, H., et al., *3D reconstruction of a gas diffusion layer and a microporous layer.* Journal of Membrane Science, 2010. **351**(1–2): p. 69-74.

109. Ostadi, H., et al., *Influence of threshold variation on determining the properties of a polymer electrolyte fuel cell gas diffusion layer in X-ray nano-tomography.* Chemical Engineering Science, 2010. **65**(6): p. 2213-2217.

110. Rama, P., et al., *Multiscale Modeling of Single-Phase Multicomponent Transport in the Cathode Gas Diffusion Layer of a Polymer Electrolyte Fuel Cell.* Energy & Fuels, 2010. **24**(5): p. 3130-3143.

111. Gunstensen, A.K., et al., *Lattice Boltzmann model of immiscible fluids.* Physical Review A, 1991. **43**(8): p. 4320.

112. He, X.Y. and G.D. Doolen, *Thermodynamic foundations of kinetic theory and Lattice Boltzmann models for multiphase flows.* Journal of Statistical Physics, 2002. **107**(1-2): p. 309-328.

113. Pan, C., M. Hilpert, and C.T. Miller, *Lattice-Boltzmann simulation of two-phase flow in porous media.* Water Resources Research, 2004. **40**(1): p. W01501.

114. Shan, X.W. and H.D. Chen, *Lattice Boltzmann Model for Simulating Flows with Multiple Phases and Components.* Physical Review E, 1993. **47**(3): p. 1815-1819.

115. Shan, X.W. and H.D. Chen, *Simulation of Nonideal Gases and Liquid-Gas Phase-Transitions by the Lattice Boltzmann-Equation.* Physical Review E, 1994. **49**(4): p. 2941-2948.

116. Swift, M.R., W. Osborn, and J. Yeomans, *Lattice Boltzmann simulation of nonideal fluids.* Physical Review Letters, 1995. **75**(5): p. 830.

117. Swift, M.R., et al., *Lattice Boltzmann simulations of liquid-gas and binary fluid systems.* Physical Review E, 1996. **54**(5): p. 5041.

118. Nourgaliev, R.R., et al., *The lattice Boltzmann equation method: theoretical interpretation, numerics and implications.* International Journal of Multiphase Flow, 2003. **29**(1): p. 117-169.

119. He, X., S. Chen, and R. Zhang, *A lattice Boltzmann scheme for incompressible multiphase flow and its application in simulation of Rayleigh–Taylor instability.* Journal of Computational Physics, 1999. **152**(2): p. 642-663.

120. Zheng, H., C. Shu, and Y.-T. Chew, *A lattice Boltzmann model for multiphase flows with large density ratio.* Journal of Computational Physics, 2006. **218**(1): p. 353-371.

121. Inamuro, T., et al., *A lattice Boltzmann method for incompressible two-phase flows with large density differences.* Journal of Computational Physics, 2004. **198**(2): p. 628-644.

122. Mukherjee, P.P., C.-Y. Wang, and Q. Kang, *Mesoscopic modeling of two-phase behavior and flooding phenomena in polymer electrolyte fuel cells.* Electrochimica Acta, 2009. **54**(27): p. 6861-6875.

123. Mukherjee, P.P., et al., *Two-Phase Behavior and Compression Effect in a PEFC Gas Diffusion Medium.* ECS Transactions, 2009. **25**(1): p. 1485-1494.

124. Niu, X.-D., et al., *An investigation of water-gas transport processes in the gas-diffusion-layer of a PEM fuel cell by a multiphase multiple-relaxation-time lattice Boltzmann model.* Journal of Power Sources, 2007. **172**(2): p. 542-552.

125. Park, J. and X. Li, *Multi-phase micro-scale flow simulation in the electrodes of a PEM fuel cell by lattice Boltzmann method.* Journal of Power Sources, 2008. **178**(1): p. 248-257.

126. Tabe, Y., et al., *Numerical simulation of liquid water and gas flow in a channel and a simplified gas diffusion layer model of polymer electrolyte membrane fuel cells using the lattice Boltzmann method.* Journal of Power Sources, 2009. **193**(1): p. 24-31.

127. Zhou, P. and C.W. Wu, *Liquid water transport mechanism in the gas diffusion layer.* Journal of Power Sources, 2010. **195**(5): p. 1408-1415.

128. Chen, L., H.-B. Luan, and W.-Q. Tao, *LIQUID WATER DYNAMIC BEHAVIORS IN THE GDL AND GC OF PEMFCS USING LATTICE BOLTZMANN METHOD.* Frontiers in Heat and Mass Transfer (FHMT), 2010. **1**(2).

129. Chen, L., et al., *Numerical investigation of liquid water transport and distribution in porous gas diffusion layer of a proton exchange membrane fuel cell using lattice Boltzmann method.* Russian Journal of Electrochemistry, 2012. **48**(7): p. 712-726.

130. Moriyama, K. and T. Inamuro, *Lattice Boltzmann Simulations of Water Transport from the Gas Diffusion Layer to the Gas Channel in PEFC.* Communications in Computational Physics, 2011. **9**(5): p. 1206-1218.

131. Molaeimanesh, G. and M.H. Akbari, *Water droplet dynamic behavior during removal from a proton exchange membrane fuel cell gas diffusion layer by Lattice-Boltzmann method.* Korean Journal of Chemical Engineering, 2014. **31**(4): p. 598-610.

132. Molaeimanesh, G.R. and M.H. Akbari, *Impact of PTFE distribution on the removal of liquid water from a PEMFC electrode by lattice Boltzmann method.* International Journal of Hydrogen Energy, 2014. **39**(16): p. 8401-8409.

133. Chen, S. and G.D. Doolen, *Lattice Boltzmann method for fluid flows.* Annual review of fluid mechanics, 1998. **30**(1): p. 329-364.

134. Mele, I., *Lattice Boltzmann Method.* 2013.

135. Shan, X.W. and G. Doolen, *Multicomponent Lattice-Boltzmann Model with Interparticle Interaction.* Journal of Statistical Physics, 1995. **81**(1-2): p. 379-393.

136. Martys, N.S. and H.D. Chen, *Simulation of multicomponent fluids in complex three-dimensional geometries by the lattice Boltzmann method.* Physical Review E, 1996. **53**(1): p. 743-750.

137. He, X.Y. and L.S. Luo, *Theory of the lattice Boltzmann method: From the Boltzmann equation to the lattice Boltzmann equation.* Physical Review E, 1997. **56**(6): p. 6811-6817.

138. Frisch, U., B. Hasslacher, and Y. Pomeau, *Lattice-Gas Automata for the Navier-Stokes Equation.* Physical Review Letters, 1986. **56**(14): p. 1505-1508.

139. Wolfram, S., *Cellular Automaton Fluids .1. Basic Theory.* Journal of Statistical Physics, 1986. **45**(3-4): p. 471-526.

140. Frisch, U., et al., *Lattice gas hydrodynamics in two and three dimensions.* Complex systems, 1987. **1**(4): p. 649-707.

141. Mcnamara, G.R. and G. Zanetti, *Use of the Boltzmann-Equation to Simulate Lattice-Gas Automata.* Physical Review Letters, 1988. **61**(20): p. 2332-2335.

142. Chen, H.D., S.Y. Chen, and W.H. Matthaeus, *Recovery of the Navier-Stokes Equations Using a Lattice-Gas Boltzmann Method.* Physical Review A, 1992. **45**(8): p. R5339-R5342.

143. Qian, Y.H., D. Dhumieres, and P. Lallemand, *Lattice Bgk Models for Navier-Stokes Equation.* Europhysics Letters, 1992. **17**(6bis): p. 479-484.

144. Buick, J.M., C.A. Greated, and W.J. Easson, *Investigation of a lattice gas model for surface gravity waves.* Physics of Fluids, 1997. **9**(9): p. 2585-2597.

145. Yuan, P. and L. Schaefer, *Equations of state in a lattice Boltzmann model.* Physics of Fluids, 2006. **18**(4).

146. Bhatnagar, P.L., E.P. Gross, and M. Krook, *A Model for Collision Processes in Gases .1. Small Amplitude Processes in Charged and Neutral One-Component Systems.* Physical Review, 1954. **94**(3): p. 511-525.

147. Yin, X.W. and J.F. Zhang, *An improved bounce-back scheme for complex boundary conditions in lattice Boltzmann method.* Journal of Computational Physics, 2012. **231**(11): p. 4295-4303.

148. d'Humieres, D., et al., *Multiple-relaxation-time lattice Boltzmann models in three dimensions.* Philosophical Transactions of the Royal Society of London Series a-Mathematical Physical and Engineering Sciences, 2002. **360**(1792): p. 437-451.

149. Qian, Y.H., *Lattice gas and lattice kinetic theory applied to the Navier-Stokes equations.* Doktorarbeit, Universite Pierre et Marie Curie, Paris, 1990.

150. Pan, C.X., L.S. Luo, and C.T. Miller, *An evaluation of lattice Boltzmann schemes for porous medium flow simulation.* Computers & Fluids, 2006. **35**(8-9): p. 898-909.

151. Succi, S., *The Lattice-Boltzmann Equation*. 2001: Oxford university press, Oxford.

152. Sukop, M.C. and D.T. Thorne, *Lattice Boltzmann modeling: an introduction for geoscientists and engineers*. 2007: Springer.

153. Zou, Q.S. and X.Y. He, *On pressure and velocity boundary conditions for the lattice Boltzmann BGK model.* Physics of Fluids, 1997. **9**(6): p. 1591-1598.

154. Moreno-Atanasio, R., R.A. Williams, and X.D. Jia, *Combining X-ray microtomography with computer simulation for analysis of granular and porous materials.* Particuology, 2010. **8**(2): p. 81-99.

155. Cnudde, V., et al., *Recent progress in X-ray CT as a geosciences tool.* Applied Geochemistry, 2006. **21**(5): p. 826-832.

156. Landis, E.N. and D.T. Keane, *X-ray microtomography.* Materials Characterization, 2010. **61**(12): p. 1305-1316.

157. Van Geet, M., R. Swennen, and M. Wevers, *Quantitative analysis of reservoir rocks by microfocus X-ray computerised tomography.* Sedimentary Geology, 2000. **132**(1-2): p. 25-36.

158. Salvo, L., et al., *3D imaging in material science: Application of X-ray tomography.* Comptes Rendus Physique, 2010. **11**(9-10): p. 641-649.

159. Ostadi, H., K. Jiang, and P.D. Prewett, *Micro/nano X-ray tomography reconstruction fine-tuning using scanning electron microscope images.* Micro & Nano Letters, 2008. **3**(4): p. 106-109.

160. Jia, X., R.A. Williams, and C. Selomulya, *Three-dimensional measurement and simulation of the dewatering behaviour of flocs and sediments using X-ray microtomography.* Journal of the South African Institute of Mining and Metallurgy, 2008. **108**(10): p. 607-612.

161. Brunke, O. *Fully-Automated 3D Metrology and Defect Analysis with High-Resolution 300 kV Microfocus Computed Tomography*. in *18th World Conference on Nondestructive Testing*. 2012. Durban, South Africa.
162. SkyScan, *SkyScan 1172 Desktop X-ray Microtomograph Instruction Manual*. 2005.
163. SkyScan, *SkyScan 1072 Desktop X-ray Microtomograph Instruction Manual*. 2008.
164. SkyScan, *SkyScan 2011 Desktop X-ray Microtomograph Instruction Manual*. 2009.
165. Feldkamp, L., L. Davis, and J. Kress, *Practical cone-beam algorithm.* JOSA A, 1984. **1**(6): p. 612-619.
166. Brunke, O., et al., *Comparison between X-ray tube based and synchrotron radiation based mu CT.* Developments in X-Ray Tomography Vi, 2008. **7078**.
167. Otsu, N., *Threshold Selection Method from Gray-Level Histograms.* Ieee Transactions on Systems Man and Cybernetics, 1979. **9**(1): p. 62-66.
168. Sezgin, M. and B.l. Sankur, *Survey over image thresholding techniques and quantitative performance evaluation.* Journal of Electronic Imaging, 2004. **13**(1): p. 146-168.
169. Huang, Y.X., et al., *Effects of porosity gradient in gas diffusion layers on performance of proton exchange membrane fuel cells.* Energy, 2010. **35**(12): p. 4786-4794.
170. Fishman, Z. and A. Bazylak, *Heterogeneous Through-Plane Porosity Distributions for Treated PEMFC GDLs I. PTFE Effect.* Journal of The Electrochemical Society, 2011. **158**(8): p. B841-B845.
171. Fishman, Z. and A. Bazylak, *Heterogeneous Through-Plane Distributions of Tortuosity, Effective Diffusivity, and Permeability for PEMFC GDLs.* Journal of The Electrochemical Society, 2011. **158**(2): p. B247-B252.
172. Kim, S.G. and S.J. Lee, *Quantitative visualization of a gas diffusion layer in a polymer electrolyte fuel cell using synchrotron X-ray imaging techniques.* J Synchrotron Radiat, 2013. **20**(Pt 2): p. 286-92.
173. Tomadakis, M.M. and S.V. Sotirchos, *Ordinary and transition regime diffusion in random fiber structures.* AIChE Journal, 1993. **39**(3): p. 397-412.

174. Tomadakis, M.M. and T.J. Robertson, *Viscous Permeability of Random Fiber Structures: Comparison of Electrical and Diffusional Estimates with Experimental and Analytical Results.* Journal of Composite Materials, 2005. **39**(2): p. 163-188.

175. Jinuntuya, F., et al., *The Impacts of Image Resolution on Permeability Simulation of Gas Diffusion Layer Using Lattice Boltzmann Method.* ECS Transactions, 2014. **48**(1): p. 93-101.

176. Zamel, N. and X. Li, *Effective transport properties for polymer electrolyte membrane fuel cells – With a focus on the gas diffusion layer.* Progress in Energy and Combustion Science, 2013. **39**(1): p. 111-146.

177. Maheshwari, P.H., R.B. Mathur, and T.L. Dhami, *The influence of the pore size and its distribution in a carbon paper electrode on the performance of a PEM Fuel cell.* Electrochimica Acta, 2008. **54**(2): p. 655-659.

178. Cho, K.T. and M.M. Mench, *Effect of material properties on evaporative water removal from polymer electrolyte fuel cell diffusion media.* Journal of Power Sources, 2010. **195**(19): p. 6748-6757.

179. Sadeghifar, H., M. Bahrami, and N. Djilali, *A statistically-based thermal conductivity model for fuel cell Gas Diffusion Layers.* Journal of Power Sources, 2013. **233**(0): p. 369-379.

180. Fairweather, J.D., P. Cheung, and D.T. Schwartz, *The effects of wetproofing on the capillary properties of proton exchange membrane fuel cell gas diffusion layers.* Journal of Power Sources, 2010. **195**(3): p. 787-793.

181. Parikh, N., J.S. Allen, and R.S. Yassar, *Microstructure of Gas Diffusion Layers for PEM Fuel Cells.* Fuel Cells, 2012. **12**(3): p. 382-390.

182. Tötzke, C., et al., *Three-dimensional study of compressed gas diffusion layers using synchrotron X-ray imaging.* Journal of Power Sources, 2014. **253**(0): p. 123-131.

183. Nabovati, A. and A.C.M. Sousa, *Fluid flow simulation in random porous media at pore level using Lattice Boltzmann Method.* New Trends in Fluid Mechanics Research, 2007: p. 518-521.

184. Lobato, J., et al., *Influence of the Teflon loading in the gas diffusion layer of PBI-based PEM fuel cells.* Journal of Applied Electrochemistry, 2008. **38**(6): p. 793-802.

185. LaManna, J.M. and S.G. Kandlikar, *Determination of effective water vapor diffusion coefficient in pemfc gas diffusion layers.* International Journal of Hydrogen Energy, 2011. **36**(8): p. 5021-5029.

186. El-kharouf, A., et al., *Ex-situ characterisation of gas diffusion layers for proton exchange membrane fuel cells.* Journal of Power Sources, 2012. **218**(0): p. 393-404.

187. Natarajan, D. and T. Van Nguyen, *A Two-Dimensional, Two-Phase, Multicomponent, Transient Model for the Cathode of a Proton Exchange Membrane Fuel Cell Using Conventional Gas Distributors.* Journal of The Electrochemical Society, 2001. **148**(12): p. A1324-A1335.

188. Siegel, N.P., et al., *A two-dimensional computational model of a PEMFC with liquid water transport.* Journal of Power Sources, 2004. **128**(2): p. 173-184.

189. Wang, Z.H., C.Y. Wang, and K.S. Chen, *Two-phase flow and transport in the air cathode of proton exchange membrane fuel cells.* Journal of Power Sources, 2001. **94**(1): p. 40-50.

190. You, L.X. and H.T. Liu, *A two-phase flow and transport model for the cathode of PEM fuel cells.* International Journal of Heat and Mass Transfer, 2002. **45**(11): p. 2277-2287.

191. Wang, Y. and C.Y. Wang, *A nonisothermal, two-phase model for polymer electrolyte fuel cells.* Journal of the Electrochemical Society, 2006. **153**(6): p. A1193-A1200.

192. Wang, Y., et al., *A review of polymer electrolyte membrane fuel cells: Technology, applications, and needs on fundamental research.* Applied Energy, 2011. **88**(4): p. 981-1007.

193. Hinebaugh, J. and A. Bazylak, *Condensation in PEM Fuel Cell Gas Diffusion Layers: A Pore Network Modeling Approach.* Journal of The Electrochemical Society, 2010. **157**(10): p. B1382-B1390.

194. Medici, E.F. and J.S. Allen, *The Effects of Morphological and Wetting Properties of Porous Transport Layers on Water Movement in PEM Fuel Cells.* Journal of the Electrochemical Society, 2010. **157**(10): p. B1505-B1514.

195. Lee, K.J., et al., *Steady liquid water saturation distribution in hydrophobic gas-diffusion layers with engineered pore paths: An invasion-percolation pore-network analysis.* Journal of Power Sources, 2010. **195**(11): p. 3508-3512.

196. Shahraeeni, M. and M. Hoorfar, *Experimental and numerical comparison of water transport in untreated and treated diffusion layers of proton exchange membrane (PEM) fuel cells.* Journal of Power Sources, 2013. **238**: p. 29-47.

197. Shahraeeni, M. and M. Hoorfar, *Pore-network modeling of liquid water flow in gas diffusion layers of proton exchange membrane fuel cells.* International Journal of Hydrogen Energy, 2014. **39**(20): p. 10697-10709.

198. Luo, G., et al., *Modeling liquid water transport in gas diffusion layers by topologically equivalent pore network.* Electrochimica Acta, 2010. **55**(19): p. 5332-5341.

199. Mukherjee, S., et al., *Lattice-Boltzmann Simulations of Multiphase Flows in PEM Fuel Cell GDLs and Micro-channels.* ECS Transactions, 2008. **16**(2): p. 67-77.

200. Hou, S.L., et al., *Evaluation of two lattice Boltzmann models for multiphase flows.* Journal of Computational Physics, 1997. **138**(2): p. 695-713.